Open Access Theses

Theses and Dissertations

12-2017

An Investigation of Alternative Aviation Fuel Spray Characteristics at Lean Blowout Conditions Using Hybrid Air-Blast Pressure-Swirl Atomizer

Dongyun Shin
Purdue University

AN INVESTIGATION OF ALTERNATIVE AVIATION FUEL SPRAY

CHARACTERISTICS AT LEAN BLOWOUT CONDITIONS

USING HYBRID AIR-BLAST PRESSURE SWIRL ATOMIZER

A Thesis

Submitted to the Faculty

of

Purdue University

by

Dongyun Shin

In Partial Fulfillment of the

Requirements for the Degree

of

Master of Science

December 2017

Purdue University

West Lafayette, Indiana

THE PURDUE UNIVERSITY GRADUATE SCHOOL
STATEMENT OF THESIS APPROVAL

Dr. Robert P. Lucht, Chair

   School of Mechanical Engineering

Dr. Jay P. Gore

   School of Mechanical Engineering

Dr. Paul E. Sojka

   School of Mechanical Engineering

Approved by:

   Dr. Tom Shih

   Head of Aeronautics and Astronautics

To my parents.

ACKNOWLEDGMENTS

I would like to thank my co-worker, Andrew Bokhart, who closely work with me for presented work. His help is invaluable.

I would like to thank Prof. Lucht, my advisor, for his guidance and support. I would also like to thank Prof. Sojka and Prof. Gore for sharing his wisdom and knowledge and for serving on my Thesis Committee. I would like to thank Federal Aviation Administration for providing the financial support for this research.

I would like to thank Scott Meyer, Andrew Pratt, and Rohan Gejii for the great technical resource at the Zucrow Laboratories. I would also like to thank all Zucrow Lab members for their support.

TABLE OF CONTENTS

LIST OF TABLES

LIST OF FIGURES

SYMBOLS

$CSPK$ Commercial Synthetic Paraffinic Kerosene

D_{10} arithmetic mean diameter

D_{20} surface mean diameter

D_{30} volume mean diameter

D_{32} Sauter mean diameter

D_0 initial drop diameter

$f_0(D)$ number probability density function

$f_3(D)$ volume probability density function

GTL Gas-to-Liquid

LBO lean blowout

MMD mass median diameter

Oh Ohnesorge number

PIV Particle Image Velocimetry

pdf probability density function

PDA Phase Doppler Anemometer

Re Reynolds number

r radial location

T_{Fuel} fuel temperature

T_{Airbox}	airbox temperature
U_z	axial velocity
U_{rms}	root-mean-square for axial velocity
$VAPS$	Variable Ambient Pressure Spray
We	Weber number
ρ_g	gas density
ρ_L	liquid density
σ_L	liquid surface tension
$\frac{\Delta P}{P}$	pressure drop across the injector swirler assembly
ΔP_{Pilot}	fuel injection pressure
μ	dynamic viscosity

ABSTRACT

Shin, Dongyun MS, Purdue University, December 2017. An investigation of Alternative Aviation Fuel Spray Characteristics at Lean Blowout Conditions using Hybrid Air-Blast Pressure Swirl Atomizer. Major Professor: Robert P. Lucht.

Many efforts on reducing pollutant emissions from the aviation gas turbines have been to mitigate the climate change and air quality. The National Jet Fuel Combustion Program (NJFCP) was initiated to develop new alternative aviation fuels, which are composed solely on hydrocarbons (non-petroleum), and to understand better the impact of chemical/physical properties of the fuels on combustion. One of the major objectives of NJFCP is to study the spray characteristics of the alternative jet fuels compared to conventional jet fuels to ensure that the performance of the alternative jet fuels is comparable to conventional jet fuels.

In this study, spray measurements for alternative jet fuels with Phase Doppler Anemometry are presented. The major objective of this work is to study spray characteristics such as droplet size, drop velocity, and spray cone angle for candidate alternative jet fuels for operating conditions corresponding to lean blowout (LBO). A hybrid air-blast pressure swirl atomizer from Parker-Hannifin Corporation is used in the experiments. The spray cone angles are investigated using shadowgraph imaging with a high speed camera. Six fuels selected by the NJFCP on the basis of chemistry are A-2, C-1, C-5, C-7, C-8, C-9. The droplet sizes and velocities are measured and

compared among six fuels at LBO conditions. For spray cone angles, three fuels (A-2, C-1, and C-5) were investigated at LBO conditions.

The effects of the fuel injection pressure and the pressure drop across the injector swirler assembly on the spray characteristics have been studied. The droplet sizes and velocities were varied for each fuel. However, the differences were minimal among the fuels. The fuel injection pressure was observed to have minimal effect on the mean drop sizes and velocities, while the pressure drop across the swirler assembly had a significant effect on those characteristics. For spray cone angles, it was observed that the effects of the injection pressure, pressure drop, and fuel type were not significant.

1. INTRODUCTION

Spray phenomena in fluid dynamics is a complicated and challenging subject. Yet, the spray can be encountered everywhere in modern life due to its practical importance. In many applications, the interaction between spray and surface is important. In gas turbine applications, the spray characteristics such as drop size, velocity, cone angle, and etc. play an important role in combustion process, and therefore must be considered carefully. According to Lefebvre [19], the combustion of liquid fuel in gas turbines is dependent on effective atomization to increase the specific surface area of the fuel and thereby achieve high rates of mixing and evaporation. In addition, the reduction in the fuel drop size leads to a higher volumetric heat release rate, easier light-up, a wider burning range, and a lower exhaust concentrations of pollutant emissions.

The reduction in pollutant emissions from the aviation gas turbines have become an increasing concerns over the last few decades. Limits on the amount of pollutants that can be released to the atmosphere has been regulated by various governments. One current focus of the aviation industry is on developing alternative jet fuels composed solely of hydrocarbons that can provide identical performance of petroleum-derived jet fuels. Hydrocarbon alternative jet fuel is desired due to its higher energy density. Furthermore, the alternative fuels do not require engine redesign nor new fuel

systems. However, information regarding the performance and characteristics of the alternative jet fuels in combustion is lacking. In addition, it is important to ensure that the alternative jet fuels meet the criteria that are considered for commercial use.

The National Jet Fuel Combustion Program (NJFCP) is jointly funded by several US federal agencies with contributions from international partners. This work is highly coordinated within the NJFCP and funded by Federal Aviation Administration (FAA) under the Aviation Sustainability Center (ASCENT) of Excellence for Alternative Jet Fuels and Environment. The work is coordinated with other universities funded by the Air Force Research Laboratory (AFRL) and NASA. The NJFCP was initiated to develop combustion-related generic test and modeling capabilities that can improve the understanding of the impact of fuel chemical composition and physical properties on combustion, ultimately leading to the acceleration of the approval process of new alternative jet fuels for aircraft use [6]. For the commercial deployment, the approval and issuance of a specification by American Society for Testing and Materials International is required. This specification requires laboratory testings to ensure that the alternative jet fuels can perform identically to the conventional jet fuels in combustion.

Some modern aircraft operate under fuel lean conditions to reduce the amount of pollutant emission. However this leads the gas turbine engines to operate near lean blowout (LBO), which is defined as a scenario in which the engine is operating in fuel lean regime in order to reduce the RPM of the turbines and a perturbation of flow through the engine may cause flame extinction. The need of relight at high altitude

and ability of restart the engine becomes a major safety concern. Thus, NJFCP focuses on engine operability under three critical conditions: lean blowout (LBO), high altitude relight, and cold start.

A knowledge regarding the spray characteristics of new alternative jet fuels at LBO conditions is currently lacking. In order to assess the performance of the alternative jet fuels, it is important to understand spray atomization, which affects the combustion dynamics, heat transfer within the combustor, and emissions [6].

Thus, the major objective of this work is to characterize the spray of the alternative jet fuels at LBO condition and compare to the conventional jet fuels (petroleum-derived). For spray characteristics, the fuel drop size, drop velocity, and full cone angle have been studied. Furthermore, the influences of the operating parameters such as the fuel injection pressure, atomizing flow velocity, and fuel types on the spray characteristics are also investigated.

2. LITERATURE REVIEW

2.1 Introduction

This chapter provides a review of measurement techniques that have been developed for sprays. The break-up mechanism for the hybrid air-blast pressure-swirl atomizer that is used in this study is described. The dimensionless numbers used to characterize the atomization are also discussed in this chapter. Lefebvre [19] stated that the flow and spray characteristics of the atomizers are strongly influenced by the liquid properties such as density, viscosity, and surface tension. In physics, these properties are functions of temperature and pressure, which are the major parameters varied in this experiment. The influences of the operating parameters on the spray characteristics such as droplet size, velocity, and cone angle are reviewed in this chapter.

2.2 Spray Measurement Techniques

Sprays are intellectually difficult and practically important topics in fluid mechanics. Yet, spray phenomena are applicable and being used in various study of fields for many different purposes. Thus, a better understanding of sprays is desired, and thus has led to the development of spray measurement techniques. Many spray measure-

ment techniques are developed based on the laser technology such as Phase Doppler Anemometry(PDA), optical patternation, Malvern spray analyzer, and holography. In this study, PDA is mainly employed to measure the drop sizes and velocities. Shadowgraph imaging with a high speed camera is also used to determine the spray cone angles.

2.2.1   Phase Doppler Anemometry

Phase Doppler Anemometry (PDA) is an extension of Laser Doppler Anemometry(LDA). The basic ideas for LDA measurements in two-phase flows were developed by Durst and Zare in 1975 [12]. LDA is based on the principle of the Doppler shift of the light reflected or refracted from a moving particle. From the detector's point of view, the frequency of light scattered from the moving particle is changed by some amount which depends on velocity and scattering geometry. The first commercial instrument for PDA was developed by Bachalo in the 1980s to measure droplet size and velocity simultaneously. The scattered light from two intersecting beams interferes at detectors placed at designated locations to generate sinusoidal Doppler burst signals. The Doppler-frequency is directly proportional to droplet velocity, and the phase of two bursts is related by the Mie scattering theory to droplet diameter [1]. The feature of PDA is to measure drop size and velocity simultaneously as well as mass flux and concentration. Furthermore, the measurement is very accurate with a high spatial resolution. PDA is a point measurement technique. Thus, it is time-

consuming process to map a spray using a series of point measurements. In addition, it cannot give an instantaneous 2D or 3D representation.

2.2.2 Malvern Spray Analyzer

The Malvern uses the laser diffraction for measurement of the spray droplet size. The technique is based on Fraunhofer diffraction of a parallel beam of monochromatic light by a moving drop. When the drops pass through a parallel beam of light, a diffraction pattern is formed in which some of the light is diffracted by an amount depending on the drop size [19]. The advantage of this technique is the speed at which data can be both accumulated and analyzed, allowing complete characterization of an atomizer. Another attribute is that the diffraction pattern generated by the drops is independent of the position of the drops in the light beam. This means that the measurements of size distribution with the drops moving at any speed is possible. On the other hands, the problem arises with Malvern in application to the high temperature environment. Thermal gradients in the hot air refract the laser beam in a random high frequency pattern. This can results in false reading on the detectors.

2.2.3 Other techniques

Particle Image Velocimetry (PIV) is a standard experimental technique in fluid mechanics, and has been adopted for planar measurements of droplet velocity fields in sprays. The common approach is to record two laser-sheet images in short time

interval. Then, the full image area is divided into a grid of small interrogation windows. Each window contains approximately $10 \sim 20$ droplets. The displacement of the droplets can be measured by cross-correlating the drop image intensity distribution from the interrogation window between two successive images. Hence, the droplet velocity within the interrogation window can be obtained [20]. Figure 2.1 shows various types of techniques for the spray measurement other than PIV. Fansler et al. [13] reviewed needs, milestones, challenges, and a broad array of techniques for spray measurement by organizing over 300 citations. Detailed discussion on each technique can be found in the article.

Needs	Experimental approaches
Droplet size	PDI
	PDS, LSD (LIF/Mie or LIEF/Mie)
	High-resolution imaging
	Forward diffraction
	ILIDS / IPI (Interferometric particle imaging)
	Glare point imaging
	Holography
	Femtosecond polarization ratio
Droplet velocity	PDI
	LDV
	PIV
	DGV
	Laser flow tagging
	High-resolution imaging (PTV)
	ILIDS / IPI (with PTV)
	Glare point imaging
	Holography
Droplet volume flux	PDI
Droplet temperature	LIF
	LIEF
	Thermographic phosphors
	Rainbow refractometry
	Raman

Fig. 2.1.: **Spray measurement techniques for drop size, velocity, and volume flux** [13]

2.2.4 Summary of Spray Measurement Technique Literatures

Various measurement techniques are developed for the spray measurement. PDA and Malvern spray analyzer are introduced as the most common measurement techniques in spray research. PDA is a pointwise measurement technique that can be used to measure the drop size, drop velocity, volume flux, concentration, and etc. simultaneously. PDA has a high accuracy and high spatial resolution but is limited in measuring in a dense spray. Malvern spray analyzer, a laser diffraction measurement technique, can be used to measure the drop size distribution with the drops moving at any speed. However, it is not applicable in high temperature environment due to the beam steering problem. The operating conditions for this study require the high temperature of surrounding gas.

2.3 Atomizer Designs and Break-up Mechanism

This section reviews on the atomizer designs and their break-up mechanisms. In this study, the hybrid air-blast pressure-swirl atomizer was used. This hybrid atomizer is a combination of both air-blast and pressure-swirl atomizers. The designs and features of air-blast and pressure-swirl atomizers are also discussed.

2.3.1 Pressure-Swirl Atomizer

Pressure-swirl atomizers are one of the simplest mechanical pressure atomizers that produce a hollow cone spray and are widely used in rocket and gas turbine

applications. The pressure-swirl atomizer injects the fuel through tangential passages into a swirl chamber as shown in Fig 2.2. The number of fuel ports can be varied depending on the design variation of atomizer. The injected fuel develops a thin and rapid swirling fuel film along the inner surface of the chamber which contracts towards the single orifice. Due to angular momentum conservation, the tangential and axial flow velocity of the fuel film increase as it flows towards the nozzle exit. These velocity components emerge into a thin conical sheet at the nozzle exit and disintegrate the conical sheet into ligaments and then drops due to instability. These atomizers have advantages at start-up and have a large operation stability range [19].
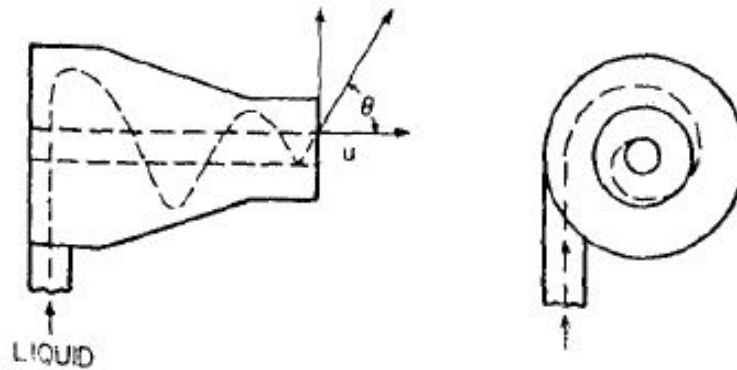
Fig. 2.2.: Flow path in pressure swirler [19]

2.3.2 Air-Blast Atomizer

The air-blast atomizers employ two separate air-flows to shatter the fuel sheet into ligaments then drops. Figure 2.3 shows the design of the prefilming air-blast atomizer. The central circular passage contains a swirler, which causes the air flow to be deflected radially outward to strike the inner surface of the fuel flow. Another

airstream flows through an annular passage containing a swirler. The swirling motion of the airflow interacts with the outer surface of the fuel sheet and leads to atomization. The air velocity in the airblast is usually limited to the value around 120m/s, thus the large amount of air is required for the airblast [19]. Due to a higher air pressure the air-blast atomizers require lower fuel pump pressures and produce finer drops. In addition, low soot formation and a blue flame of low luminosity can be achieved by a thorough fuel and air mixing process from the air-blast atomizers. The primary disadvantages of the air-blast atomizers are narrow stability limits and poor atomization quality at start-up due to the low velocity of air.
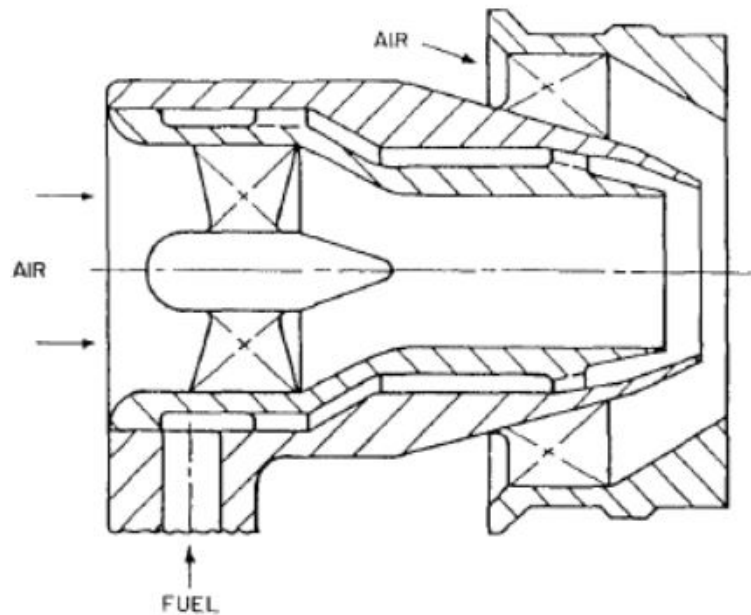
Fig. 2.3.: Prefilming airblast atomizer design [19]

2.3.3 Hybrid Atomizer

The advantages of both air-blast and pressure-swirl atomizers are combined into one to overcome the drawback from each type of atomizer. This is a hybrid atomizer. The hybrid atomizer has two fuel injection circuits: the main and the pilot. The pilot injector uses the pressure-swirl atomizer mechanism, in which fuel is directed out through the central orifice and resulting in a hollow cone spray. The fuel spray then interacts with two air swirl flows provided from the air swirler assembly surrounding the primary nozzle portion. The air co-flow through each swirler which has a number of helical or angled vanes results in co-rotating air flows. These air swirl flows promote breakup of the fuel into ligaments then quickly into droplets. The mechanism that is introduced in the swirler assembly defines the airblast [21]. Although the hybrid atomizers can overcome the drawbacks from the air-blast and pressure-swirl atomizers, the complexity of the design becomes a concern. In addition, the weight of the atomizer increases. Figure 2.4 shows the breakup mechanism for the hybrid air-blast pressure-swirl atomizer that is used in this experiment. The spray from the pilot injector impinges on the inner surface of the swirler assembly. Details on the fuel impingement is discussed in later section. This impingement creates a fuel film on the inner surface. A thin fuel film interacts with the air flows from the air swirler and atomized.
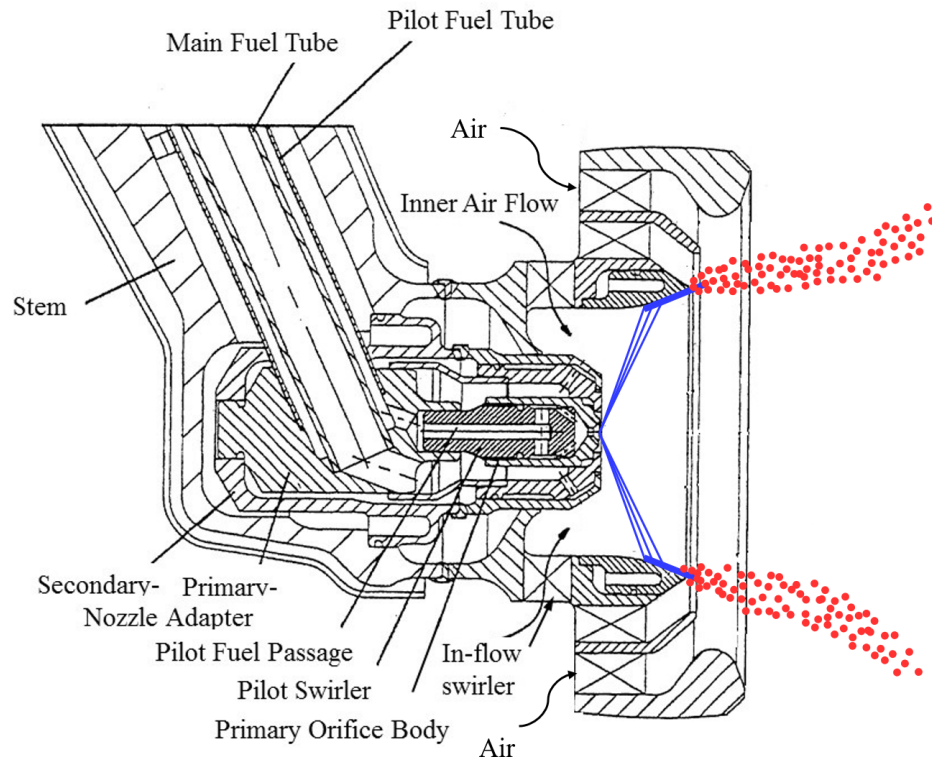
Fig. 2.4.: Breakup mechanism for hybrid atomizer

2.3.4 Summary of Atomizer Design Literatures

Many studies have performed to determine the spray characteristics with different types of pressure-swirl and air-blast atomizers using PDA and Malvern spray analyzer. Different atomization qualities can be expected from each type of atomizer, which has different break-up mechanism. The hybrid air-blast pressure-swirl atomizer is designed to have both features of the air-blast and pressure-swirl atomizers to overcome the drawbacks of each atomizer. The lack of study in the break-up mechanisms and spray characteristics of this particular hybrid atomizer using PDA represents a considerable gap in the literature.

2.4 Characterizing Drop Size Distributions in Sprays

In many mass transfer and spray studies, the mean or average diameters are used instead of the complete drop size distribution. The concept of representative diameters and its notations has been generalized by Mugele and Evans [23].

The generalized representative diameters can be expressed as

$$D_{ab} = \left[\frac{\Sigma N_i D_i{}^a}{\Sigma N_i D_i{}^b} \right]^{\frac{1}{(a-b)}} \tag{2.1}$$

where i denotes the size class considered, N_i is the number of drops in size class i, and D_i is the diameter of the size class i. D_{10} is the arithmetic mean diameter of all the drops in the spray and can be expressed as

$$D_{10} = \frac{\Sigma N_i D_i}{\Sigma N_i} \tag{2.2}$$

D_{20} is the surface mean diameter. It is useful for surface area controlling applications and expressed as

$$D_{20} = \left[\frac{\Sigma N_i D_i{}^2}{\Sigma N_i} \right]^{\frac{1}{2}} \tag{2.3}$$

D_{30} is the volume mean diameter that calculated from the mean of droplet volume. It is used for hydrology and mass flux applications.

$$D_{30} = \left[\frac{\Sigma N_i D_i{}^3}{\Sigma N_i} \right]^{\frac{1}{3}} \tag{2.4}$$

D_{32} is the diameter of the drop whose ratio of drop volume to surface area is equal to that of the complete spray sample.This mean diameter is important characteristic that used in mass transfer and combustion applications. The expression is

$$D_{32} = \frac{\Sigma N_i D_i{}^3}{\Sigma N_i D_i{}^2} \tag{2.5}$$

$D_{0.5}$ is the drop diameter such that 50 % of total liquid volume is in drops of smaller diameter. This is the mass mean diameter (MMD). MMD is used in describing the spray drops in the combustion application which mass transfer and volume are significant.

$$0.5 = \int_0^{MMD} f_3(D)dD \tag{2.6}$$

The representative diameters that are used in this study to characterized the spray measurements are D_{10}, D_{32}, and Mass Mean Diameter. In Eq. 2.6, f_3 symbolizes the volume probability density function(pdf). The volume pdf is the probability density of a drop that has a volume of $\frac{\pi D^3}{6}$. Two other probability density functions to quantify the hybrid atomizer spray are the number pdf, f_0 (probability density that a drop has diameter D), and the area pdf f_2 (probability density that a drop has surface D^2).

2.5 Dimensionless Numbers for Spray Characteristics

The dimensionless parameters that are used to characterize the spray of hybrid air-blast pressure-swirl atomizer are the Weber number and Ohnesorge number. The Weber number presents a ratio of the inertia forces to surface tension forces. The ratio indicates whether the disruptive force or the restorative force on the fluid element is dominant. The Weber number can be expressed as Eq. 2.8:

$$We = \frac{\rho_g U_{rel}^2 D_o}{\sigma_L} \tag{2.7}$$

ρ_g is the gas density, U_{rel} is the relative velocity between gas and liquid, D_o is the initial drop diameter, and σ_L is the surface tension.

A higher Weber number indicates the dominant energy on the drop is the kinetic energy. This means that most of the inserted energy is converted into the kinetic energy, which fonds to break up the fluid or droplets. A lower Weber number indicates the dominant energy is the surface tension energy. Most of inserted energy is converted into surface tension energy in this case. The Weber number is the most important dimensionless number for characterizing the droplet formation. Thus, the Weber number can be used to distinguish the droplet break-up regimes.

The Ohnesorge number is a dimensionless number that represents the ratio of internal viscosity dissipation to the surface tension energy. The Ohnesorge number can also be written as the ratio of the viscous forces to the square root of the inertial

and the surface tension forces or the square root of the Weber number divided by the Reynolds number. The expression for Ohnesorge number is shown in Eq.2.9:

$$Oh = \frac{\sqrt{We}}{Re} = \frac{\mu_L}{\sqrt{\rho_L \sigma_L D_o}} \qquad (2.8)$$

As shown in Eq.2.9, the Ohnesorge number is independent of the velocity but contains the liquid properties. The lower Ohnesorge number indicates lower friction losses due to viscous forces. Most of the inserted energy is converted into surface tension energy. The higher Ohnesorge number indicates the dominant energy for the drop is internal viscous dissipation.

2.6 Influence of Operational Parameters on Spray Characteristics

The operational parameters that influence spray characteristics such as the droplet size, velocity, and cone angle are discussed in this section. The hybrid air-blast pressure-swirl atomizer was used in this study. Thereby, the spray characteristics of pressure-swirl atomizers, air-blast atomizers, and hybrid atomizers were considered. The fuel injection pressure, fuel temperature, and type of fuel were considered for the operational parameters in this study.

2.6.1 Influence of operational parameters on droplet size

The droplet size plays an important role in combustion dynamics. In most combustion systems, reduction in mean fuel drop size leads to a higher volumetric heat

release rate, easier light-up, a wider burning range, and a lower exhaust concentrations of pollutant emission [19].

Wang and Lefebvre [28] investigated the influence of the fuel injection pressure and fuel temperature on the droplet size with two different fuels, JP4 and DF2, for a pressure-swirl atomizer at normal ambient air pressure using a Malvern spray analyzer. The mean drop size of JP4 was observed to decrease when the fuel injection pressure increased. An increase in fuel temperature also decreased the mean drop size. These results demonstrated that the atomization quality was improved by increasing the fuel injection pressure and the fuel temperature. However, the beneficial effect of increase in fuel temperature was sustained to higher levels of fuel injection pressure.

A similar trend of decreasing mean drop size with increasing fuel injection pressure was observed by Kannaiyan et al. [17] using synthetic jet fuels. Kannaiyan et al. [17] investigated the spray characteristics of two Gas-to-Liquid (GTL) synthetic jet fuels for a pilot-scale pressure-swirl nozzle at ambient pressure conditions to validate GTL fuels by comparing them with the characteristics of the conventional Jet A-1 fuel. The droplet size and velocity of the spray in downstream of a pressure-swirl nozzle were measured using Phase Doppler Anemometry at 0.3MPa and 0.9 MPa of fuel injection pressures. The synthetic jet fuels used for the experiment were Commercial Synthetic Paraffinic Kerosene (CSPK) by Shell Inc. and the GTL blend (B-2), a blend of CSPK and Shellsol solvents. Kannaiyan et al. [17] found that an increase in fuel injection pressure resulted in a decrease in mean drop size and an increase in cone angles of all testing fuels.

Custer [5] studied the influence of atomizer designs and liquid properties on the fuel injector performance of an air-blast atomizer using a laser diffraction technique. The author varied the pressure drop and observed that the mean drop size of the spray decreased with an increase in pressure drop. Buschhagen [4] investigated the effect of fuel injection pressure and alternative aviation fuel types on the spray for a hybrid air-blast pressure-swirl atomizer at ambient pressure using Phase Doppler Anemometry (duel-PDA). The study focused on four different operational parameters: fuel temperature, fuel injection pressure, pressure drop across the swirler, and fuel types. Buschhagen showed that the mean drop size decreased with an increase in fuel temperature from 240K to 290K, in fuel injection pressure from 25 psi to 75 psi, and in pressure drop across the swirler from 2% to 6% at ambient surrounding pressure (0.1MPa) for three different aviation fuels (A2, C1, and C5). Rizkalla [25] also studied the effect of the atomizing air velocity (pressure drop) and the fuel flow rate (fuel injection pressure) on the mean drop size of air-blast atomizer spray. The author observed that the mean drop size decreased with an increase in atomizing air velocity and fuel flow rate.

According to Lefebvre [19], the spray characteristics of most atomizers are strongly influenced by the liquid properties of density, viscosity, and surface tension. The liquid property is a function of the temperature. The influence of liquid viscosity and surface tension on mean drop size was studied by Wang and Lefebvre [18] using a pressure-swirl atomizer. The liquids employed in their study were water, diesel oil, and several blends of diesel oil with polybutene. These liquids provided a range of

viscosity from 3×10^{-6} to $18 \times 10^{-6} m^2/s$, and a range of surface tension from 0.027 to 0.0734 kg/s^2. The flow number, nozzle geometry, cone angle, and surrounding air pressure were fixed. Wang et al. [18] plotted the mean drop size versus liquid injection pressure on a logarithmic scale with the liquid viscosity variations and found the mean drop sizes tend to decrease when the liquid viscosity and density increase. However, the effect of viscosity was found to be less significant as the fuel injection pressure increase. The studies of Wang and Lefebvre [18] and Buschhagen [4] clearly show that liquid properties have a significant effect on the mean drop size for the pressure-swirl atomizer.

Liquid properties have a similar effects on the mean drop size for the air-blast atomizer spray. Rizkalla [25] investigated an influence of liquid property on the mean drop size of the air-blast atomizer spray. The tested liquids were blends of Hyvis Polybutene with kerosene, a blend of Butyl Alcohol with water, and a blend of Dibromo-ethane with ethylated spirits. The employed liquids represented a range of values of surface tension from 26 dynes/cm to 73 dynes/cm, while the viscosity and density were varied between 0.8 g/cm^3 and 1.8 g/cm^3 respectively. The study found that the mean drop size increased with an increase in the surface tension and in the viscosity of the liquid. An increase in liquid density increases the mean drop size initially but a decrease is observed with further increase in density. Rizkalla [25] suggested the investigation in liquid film thickness and high speed photography of atomization to provide an explanation for the effect of density. A similar effect of the

surface tension on the mean drop size was observed by Custer, et al [5]. However, the author found that the viscosity had no significant effect on the mean drop size.

2.6.2 Influence of operational parameters on drop velocity

The drop velocity is one of most important spray characteristics for influencing combustor performance. The drop velocity determines how far the drops can travel in the combustor and affects the evaporation rate and growth of instability of the drops, which are directly related to the atomization quality. Vouros et al. [27] investigated alternative aviation fuel blends to assure a compatibility of their spray characteristics for a generic nozzle by comparing those fuels with Jet A-1 using the PDA measurement technique. The selected fuel blends were based on a narrow cut of paraffins, mixed with appropriately selected aromatics and naphthenes. A higher axial velocity was observed for fuels with a higher density and surface tension. Interestingly, the study found the axial velocity was better correlated with the density and surface tension for the blended fuels than with the viscosity. Further investigation of these effects was suggested.

Kannaiyan et al. [17] showed that an increase in fuel injection pressure results in an increase in the droplet velocities. However, the significant difference in droplet mean axial velocities is seen only at an fuel injection pressure of 0.9 MPa due to the dominance of inertial force. Kannaiyan et al. concluded that the effect of surface tension on droplet disintegration and dispersion is prominent at such high flow field.

Therefore, the combined effect of high inertial force and the difference in surface tension between the fuels resulted in different drop velocities.

The experiment by Durdina et al. [8] shows the effect of fuel injection pressure on the droplet velocity with two different pressure-swirl nozzles for turbojet engines (spill return, simplex nozzle) at different distances from the nozzle using PIV and PDA measurements. A higher fuel injection pressures more momentum is transferred to the liquid, resulting in an increase in the drop velocity. This original liquid momentum is well conserved near the nozzle exit. Decreasing droplet size due to higher injection pressure and increasing interfacial area, however, increases the interaction between the droplets and air downstream. This causes a rapid reduction in droplet momentum. Thus, the velocity of droplets decays with distance from the nozzle as the rate of droplet momentum increases.

2.6.3   Influence of operational parameters on spray cone angle

The spray structure of pressure-swirl atomizers is hollow-cone subjects the spray to the influence of the surrounding air. When the spray cone angle increases the extent of this exposure increases, leading to improved atomization, better fuel-air mixing, and better dispersion of the fuel drops throughout the combustion volume [7]. For these reasons, the cone angle is an important characteristic of a pressure-swirl atomizer. Although an increase in cone angles is usually beneficial for gas turbine combustors, a reduction in cone angles can be also beneficial in improving lean blowout limits and

increasing combustion efficiency. Thus, it is important to study the spray cone angle which can be influenced by type of atomizer and liquid properties.

Chen et al. [7] investigated the effects of fuel injection pressure, viscosity, and discharge orifice length/diameter ratio on the spray cone angle of a simplex atomizer using a patternator. The patternator has the total of 29 sampling tubes, spaced 4.5 deg apart along a radius of curvature of 10 cm. The method has been fully described by Ortman and Lefebvre [24]. The study found that the effective spray cone angle increased with the increase in fuel injection pressure and decrease in discharge orifice length/diameter ratio. The higher fuel injection pressure increased the interaction between spray and the surrounding air due to the higher momentum in fuel injection and resulted the increase in spray cone angles. Ortman and Lefebvre. [24] also found that the spray cone angle increased with the increase in fuel injection pressure. However, the spray cone angles did not increase continuously with the increase in fuel injection pressure due to a function of nozzle design. Kannaiyan et al. [17] and Durdina et al. [8] also observed that an increase in fuel injection pressure resulted in an increase in cone angles for all test fuels.

According to Chen et al. [7], an increase in liquid viscosity decreases the effective spray cone angle. The effect becomes more pronounced at the highest level of viscosity. Custer et al. [5] investigated the effect of fuel properties such as surface tension and viscosity on the spray cone angles produced by a air-blast atomizer. The study also observed that an increase in fuel viscosity decreased the spray cone angles. This is due

to the effects of viscous forces that decrease the swirling motion of the liquid sheet. On the other hand, the cone angle increased with an increase in surface tension.

2.6.4 Summary of Influence of Operational Parameters on Spray Characteristics Literatures

The effect of the fuel injection pressure, fuel temperature, pressure drop, and fuel property on spray characteristics have been previously studied. The previous investigations have been done mostly with a pressure-swirl atomizer and an air-blast atomizer under ambient pressure conditions. Although Buschhagen et al. [4] used a hybrid air-blast pressure-swirl atomizer to study its spray characteristics, the operating conditions were at different ambient pressure and temperature. Kannaiyan et al. [17] suggested that it is essential to investigate the spray characteristics of the fuels under gas turbine combustor conditions in order to understand the true benefits of their alternative fuels. From the literature review, the spray characteristics of hybrid air-blast pressure-swirl atomizer under actual aircraft engine operating conditions needs to be studied for a better understanding of the effect on engine performance.

3. EXPERIMENTAL APPRATUS

3.1 Introduction

This chapter introduces the major components of the experiment. The first section describes the atomizers that was used in this study. The second section describes the airbox and pressure vessel, parts of Purdue Variable Ambient Pressure Spray (VAPS) test rig. The third section focuses on the fuel cart, which controls the fuel flow and the fuel chiller. The fourth section describes the nitrogen system and the air heater, which was used to heat up the nitrogen flow. The fifth section focuses on the spray operating parameters. The sixth section describes a Phase Doppler Anemometry (PDA) and discusses the user settings. The last section focuses on the shadowgraph imaging for cone angle measurement.

3.2 Hybrid Airblast Pressure Swirl Atomizer Design

The hybrid air-blast pressure-swirl atomizer used in this experiment was designed by researchers at Parker-Hannifin Corporation [21]. Figure 3.1 shows a cross-sectional side view of hybrid air-blast pressure swirl atomizer. The atomizer has two circuits for the fuel injection: the main and the pilot. The pilot injector uses the pressure swirl atomizer mechanism. As shown in Fig 3.2, the fuel is injected through the central

pilot fuel passage and fed to five discharge passages via intermediate passages. These discharge passages are angled with respect to the central axis "A" as depicted in cross-section B-B. The angled discharge passages causes the fuel to swirl and impinge upon the conical inner end surface. The fuel is then directed out through the central orifice and resulted as a hollow cone spray. As shown in Fig.3.1, the air swirler assembly surrounds the primary nozzle portion of the atomizer. In the course of FAA research, the question arose as to whether or not the fuel injected from the pilot will impinge on the inner surface of the swirler assembly. This issue was investigated by applying machining blue paint on the inner surface of the swirler assembly and flowing methanol though the pilot line. Machining blue paint is soluble in methanol. If the methanol injected from the pilot line impinges on the inner surface, it should remove the machining blue paint applied on the inner surface. Figure 3.3 shows the test result. The methanol that is injected through the pilot injector resulting in removal of all machining blue paint on the inner surface. This confirms that the pilot fuel spray impinges on the inner surface.
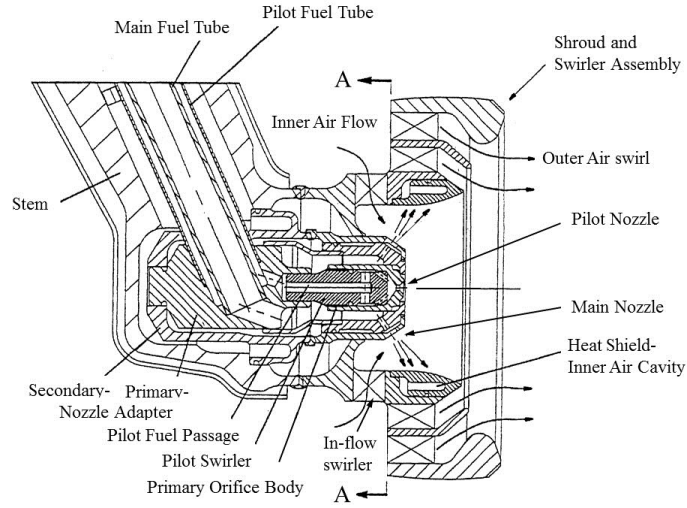
Cross-section A-A
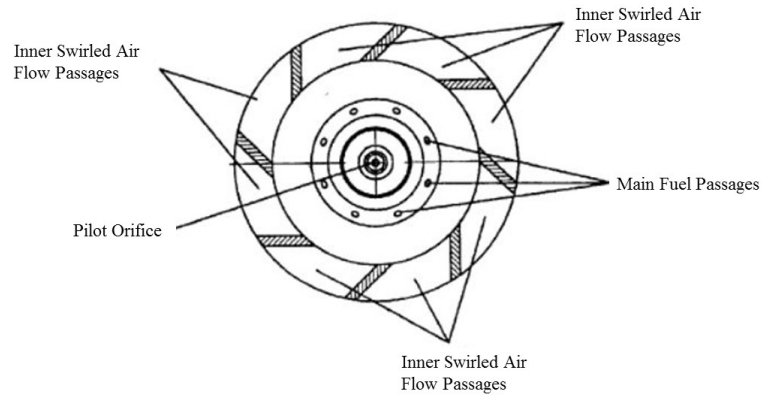
Fig. 3.1.: Hybrid airblast pressure swirl design from Parker-Hannifin Corporation [21]
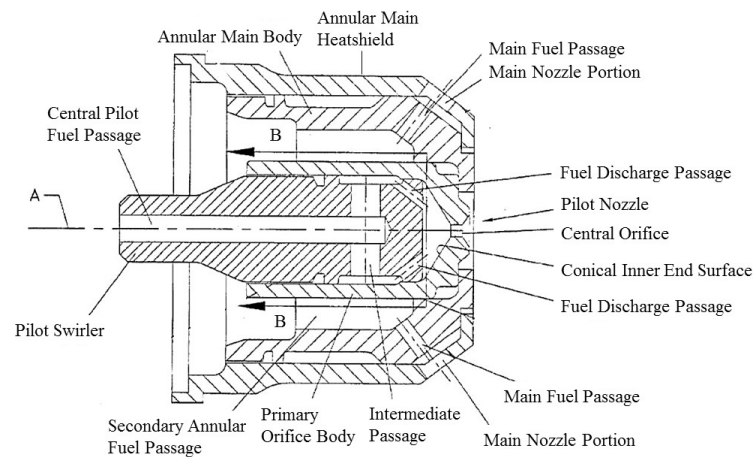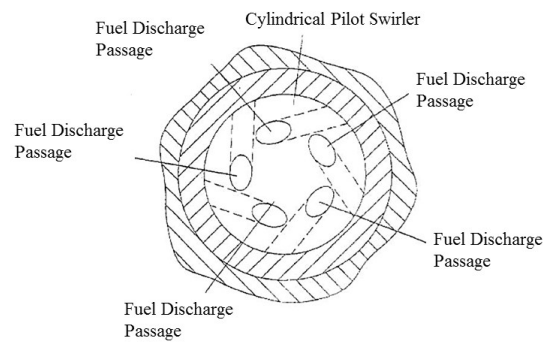
Fig. 3.2.: **Primary nozzle portion of the Hybrid airblast pressure swirl atomizer** [21]

The fuel sprayed through the pilot injector then creates a thin fuel film on the inner surface of the swirler assembly. A thin continuous sheet resulting at the end of the inner surface interacts with swirl flows provided by the air swirler assembly surrounding the primary nozzle portion. The air co-flow through each swirler which has angled vanes resulted in co-rotating air flows. These air swirl flows break up

the fuel film into ligaments and then quickly into droplets. The mechanism that is introduced in swirler assembly defines the airblast [21].

The main circuit is connected to the secondary nozzle portion surrounded by the air swirler assembly and provides the fuel to the main fuel passage. The fuel in the main circuit is directed radially outward in discrete streams from eight of main fuel passages designed around the nozzle tip. The inner air flow, which is provided from the radial in-flow swirler surrounding the main fuel nozzles, guides the fuel stream outward and accelerates the fuel. By spreading the fuel outward, the inner air flow distributes the fuel evenly across the prefilmer surface to a thin fuel film, resulting a thin continuous sheet at the end of the prefilmer surface. The inner and outer air flows from the air swirler assembly, then, break up the thin fuel sheet into the ligaments then quickly to droplets [21].

(a)   (b)
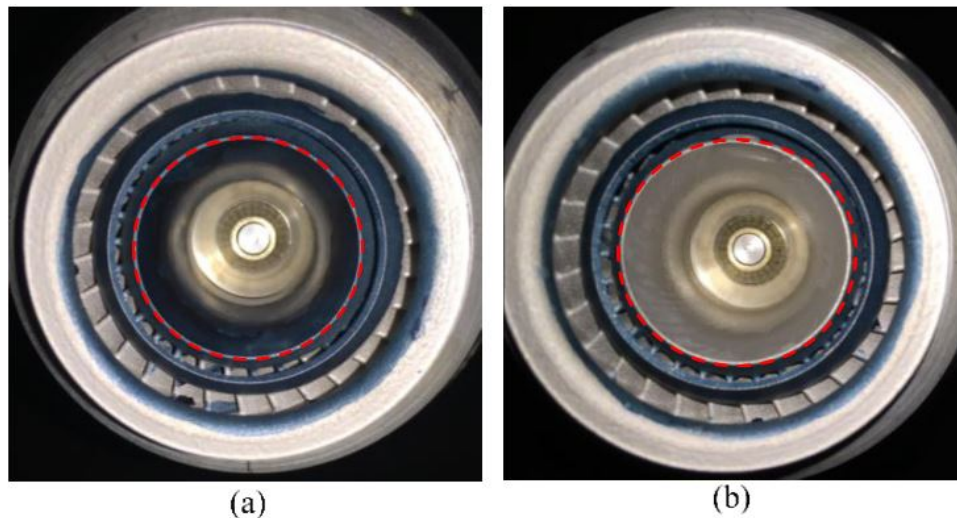
Fig. 3.3.: Inner surface impinging test using methanol. (a) Machining blue paint applied on inner surface of the swirler assembly. (b) Removal of machining blue paint after flowing methanol through the pilot injector.

3.3 Nitrogen and Heating System

A 6000 psi nitrogen system from High Pressure Lab was used to supply the airbox flow and sweeping flow in this experiment. Liquid nitrogen from a 2500 gallon (9463 liters) facility tank is pumped up to 6000 psi (414 bars) and vaporized to pressurize a 250 ft^3 (0.707 m^3) tube trailer. This tube trailer is on loan from NASA White Sands through the Rocket Propulsion Test Management Board [14]. The air co-flow for this experiment was replaced with nitrogen flow in order to prevent the formation of combustible mixture in the vessel. An electric air heater and a natural gas air heater were used to heat up the nitrogen flows in the VAPS system. The electric air heater can operate at maximum power of 80 kW. This electric air heater can supply the heated air to the test cells at temperature up to 1200 $°F$ (922 K) and pressure up to 600 psi (41.3 bars) and was used to heat the airbox flow. The natural gas air heater can supply the heated nitrogen to the test cells at flow rates up to 15 lbm/sec (6.80 kg/s) This air heater can heat the nitrogen up to 1000 $°F$ (811 K) and with 700 psi (48.3 bars) as the maximum pressure. Figure 3.4 shows the schematic diagram of heated nitrogen flow lines and fuel lines in VAPS system.
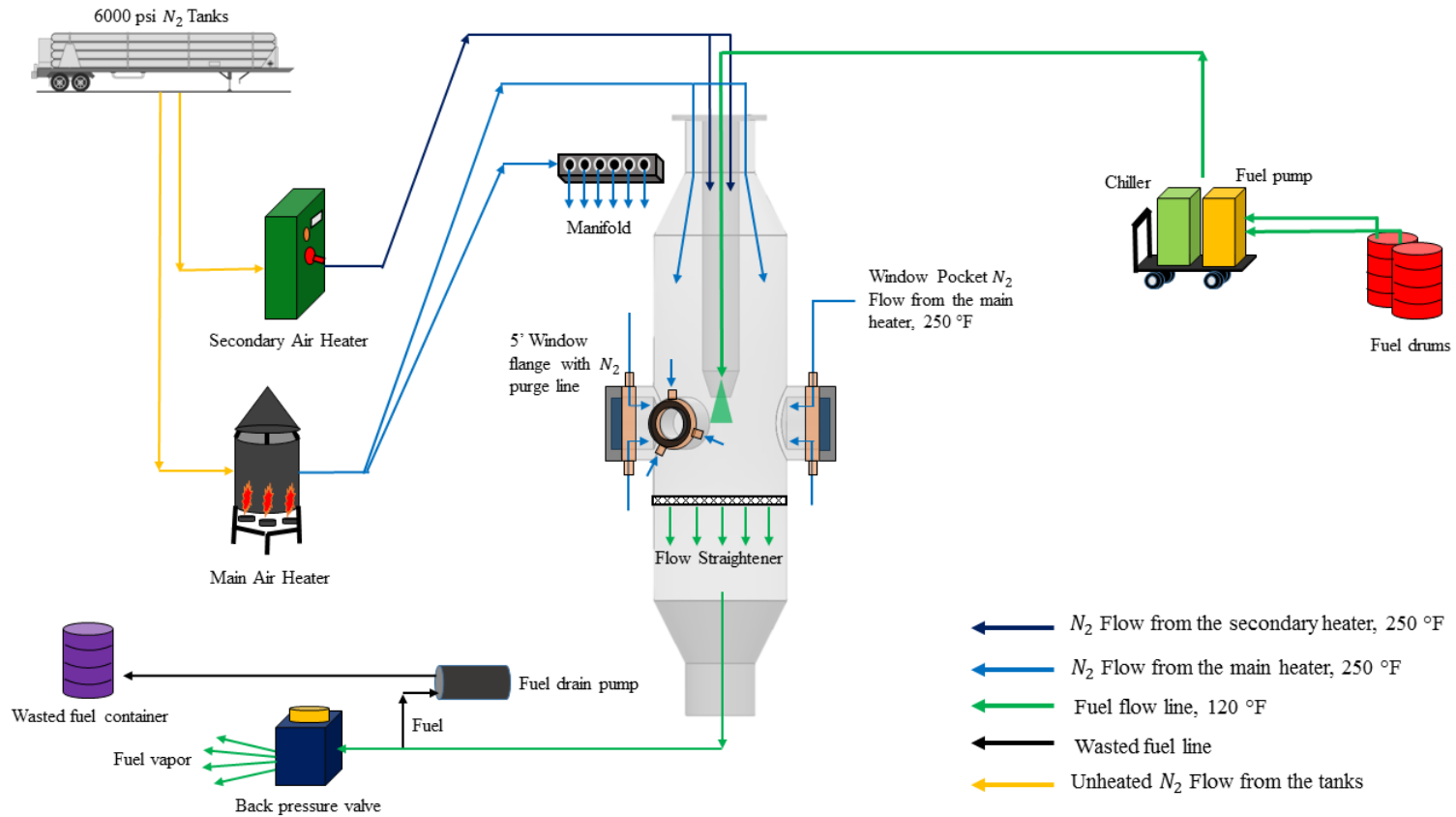
Fig. 3.4.: Schematic diagram of nitrogen flow lines and fuel lines in VAPS system

3.4   Airbox and Pressure Vessel

3.4.1   Airbox

The heated nitrogen co-flow was supplied to the injector by encasing it within an end section of a pipe. This pipe is called airbox in this experiment. Figure 3.5 shows the design of the airbox with the swirler mounted on the bottom of the pipe. The airbox has 3.5 inches (89 mm) in diameter. A 0.5 inch (12.7mm) thick metal plate encloses the top of the airbox and has the ports for the fuel lines, pressure transducer, and thermal couple. The pilot and main fuel lines are running through the airbox and supply the fuel to the injector. Due to the heat convection between the heated nitrogen co-flow and fuel, the fuel temperature increases in the airbox.

ITEM NO.	DESCRIPTION	QTY.
1	AIR BOX PIPE	1
2	AIR BOX INLET CAP	1
3	0.25IN FUEL LINES	2
4	MODIFIED 6IN DIAMETER PIPE	1
5	UPPER FLANGE WITH ORING SEAL	1
6	TOP FLANGE	1
7	MODIFIED TIGHT TOLERANCE ROD 8934K213	2
8	MODIFIED CLASS 600 6IN BLIND TEXAS FLANGE	1
9	BALL SCREW COLLAR	1
10	BALL SCREW 98804A040	1
11	TOP BRACKET	1
12	FLEXIBLE FUEL LINES	2
13	BALL SCREW HOLDER	1
14	BRONZE BUSHING SAE 841 (6338K437)	2
15	AS568A-2-340 SILICONE O-RING	2
16	SOCKET HEAD CAP SCREW 9012BA846	12
17	SKF 81102 TN	2
18	WASHER 93852A104	3
19	SOCKET HEAD CAP SCREW 9012BA842	2
20	91259A731 SHOULDER SCREW	1
21	CUSTOM WASHER	1
22	94945A225 NUT	1
23	90099A031 NUT	3
24	91259A720 SHOULDER SCREW	2

SECTION Q-Q
SCALE 1 : 10

Fig. 3.5.: Airbox and assembly drawing with labels [14].

3.4.2 Pressure Vessel

In order to achieve the pressure difference between the airbox and surroundings, the airbox was encased by a pressure vessel. By supplying heated sweeping flow in the pressure vessel, a desired pressure and temperature in the vessel was obtained.

The pressure vessel was designed originally by Loren Crook [Rachedi, et al. [26]]. The pressure vessel is capable of withstanding 600 psi (41.4 bars) at 1200F (922 K). The material for the vessel is 12 NPS schedule 80, 316 stainless steel. The ends of the pressure vessel are reduced to 6 NPS and flanged with class 600, 316 stainless steel

flanges. When the pressure vessel is assembled on the stand, it is 98.1 inches (2490 mm) tall, has an inside diameter 11.750 inches(298.5 mm), and has a wall thickness of 0.5 inch(12.7 mm).

There are four optical ports welded to the middle of the pressure vessel as shown in Fig 3.6. Two ports are 4.5 inches (114.3 mm) in diameter and facing each other. The other two ports are 2.5 inches (65.5 mm) in diameter and located 60 degrees off center from the optical axis. The optical windows and the flanges for the pressure vessel were redesigned for the current project. Two 5-inch (127 mm) diameter optical windows are Schlieren polished and designed to be 1.2 inches (30.48 mm) thick. Two 3-inch (76.2 mm) diameter optical windows are also Schlieren polished and designed to be 0.7 inches (17.78 mm) thick. A Grafoil gasket was used to seal between the optical windows and the flanges. These windows allow PDA to access the spray for the measurements.

The optical accessibility is critical for the PDA measurement. The windows on the pressure vessel are required to be clean during the measurements. The fuel spray, however, got onto the windows and affected the measurements by blocking and distorting the refraction from the spray. To resolve the issue, additional window flanges were fabricated and mounted as shown in Fig 3.7. In order to prevent fuel condensation on the windows, hot nitrogen was injected through four 1/8 inch (3.175 mm) ports on the inner ring surface of the flanges. This created a shield near the inner window surface to prevent the fuel from condensing on to the windows and promoted the fuel evaporation. At higher fuel injection pressure and higher pressure drop, the

spray mist was getting on the windows. However, the temperature of the windows and window flows were high enough to evaporate the fuel mist quickly.

The flanges and optical windows have 8 bolts. The bolts on the 5-inch (127 mm) optical windows were torqued to 20 ft/lb (27.1 Nm). The bolts on the 3-inch (76.2 mm) diameter optical windows was torqued to 10 ft/lb (13.6 Nm).

The pressure vessel has the instrumentation ports in several locations. Two ports are used for 1/8 Omega type-K thermocouples and one port for a Druck PMP-1260 pressure transducer in order to measure and record the pressure and temperature in the vessel. The uncertainties that provided by the manufacturer for these thermal couple and pressure transducer are 0.75 % and 0.433 % respectively.
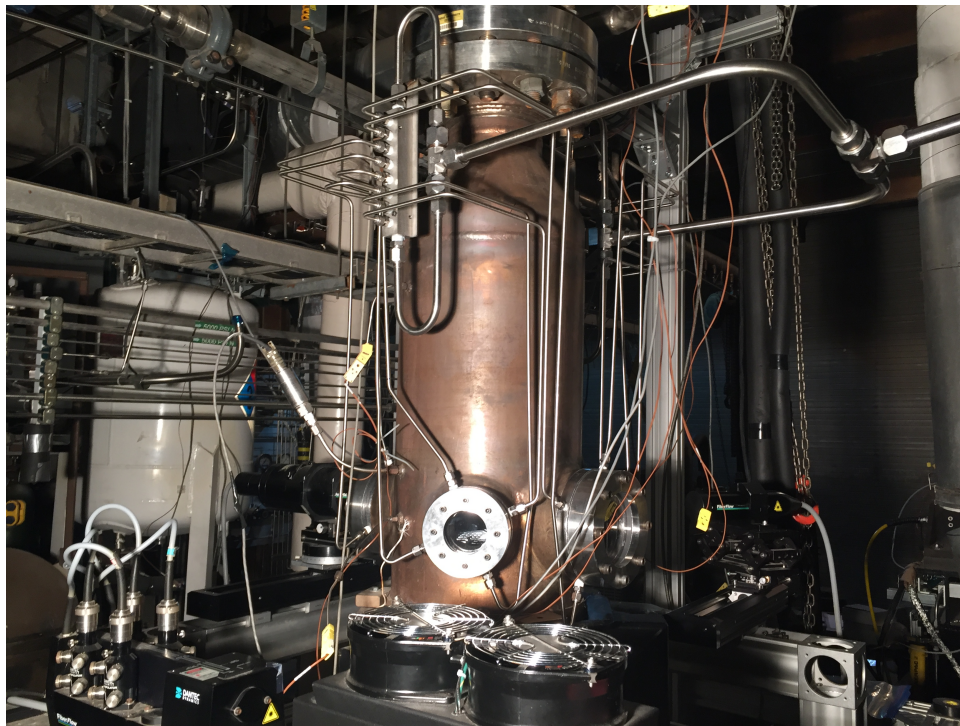
Fig. 3.6.: Image of pressure vessel in test cell
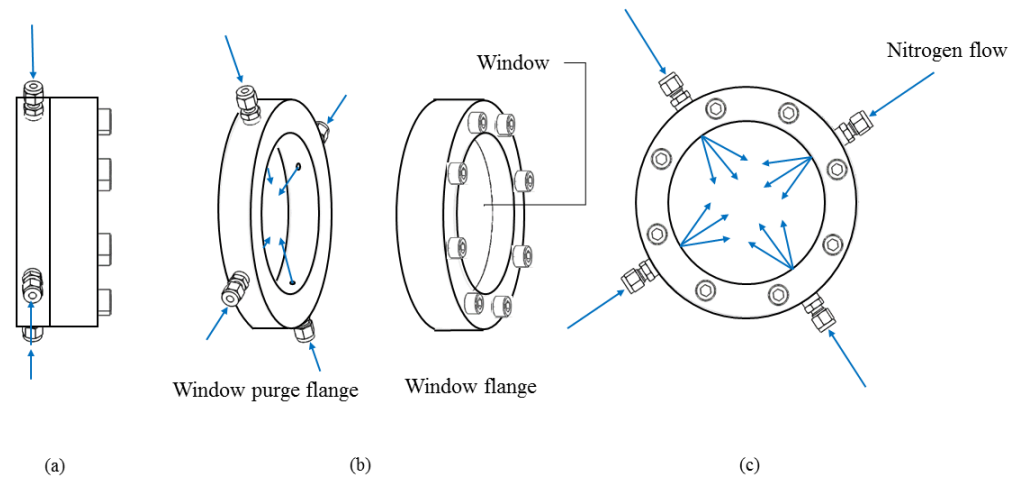
Fig. 3.7.: **Window flange design with window flow**

3.5 Exhaust System

The exhaust system consists of an Eaton 31L gas/liquid separator, a Robo Drain RD750, and a back pressure control valve. The Eaton 31L gas liquid separator is connected to the outlet of the pressure vessel by a 600 lb 316 SS flange connected to a 6 inch (152.4 mm) schedule 80 elbow and reduced to a 4 inch (102 mm) schedule 80 pipe with a 4 inch (102 mm) 150 lb (68 kg) flange. The vessel is rated for 350 psia (24.1 bars) pressure and the allowable flow rate inside the gas-liquid separator is a function of the pressure inside the vessel.

The mixture of fuel droplet and nitrogen flows into the gas-liquid separator and swirl around. The fuel drops, then, move to the outside of the gas-liquid separator

due to the centrifugal force. The liquid fuel droplets fall out of the gas stream as the velocity of the flow is decreased. The nitrogen and vaporized fuel drops leave the separator to be exhausted to the ambient. The liquid fuel droplets leave the separator through an external drain and are collected in the Robo Drain.

The Robo Drain RD750 is connected to the outlet of the external drain on the gas-liquid separator. The mechanism of Robo Drain is that a reservoir fills up until a float mechanism reaches the capacity of the drain. Then the control air is activated and purges the collected residual fuel from the tank to a waste fuel drum until the float reaches the minimum drain level. This cycle repeats and purge out fuel but never lets nitrogen escape through outlet of the drain.

The back pressure control valve is connected to the end of the gas-liquid separator via 4 inch (102mm) schedule 40 pipe. The back pressure control valve is an ABZ 028 valve with electronic actuator that is controlled remotely during test operation. The valve controls the amount of nitrogen that flows out of the pressure vessel to the surroundings.

3.6 Fuel Cart and Fuel Supply System

3.6.1 Fuel Cart and Chiller

The fuel cart is a mobile fuel supply system that was designed for the Combustion Rules and Tools program. The fuel cart is connected to 55 gallons (208.2 liters) of fuel drums by flexible stainless steel hoses with quick disconnects and a PTFE interior

lining. The fuel drum has a fuel manifold assembly that consists of three tubes with quick disconnects, a fuel filter from Norman Filter Company, and a customized drum cap as shown in Fig. 3.8.

The IMO CIG Lip Seal and Weep Hole Design gear pump is used to pump and supply two fuel circuits in the system with a maximum fuel pressure of 2000 psi (14 MPa). Both fuel circuits were isolated from the fuel exiting the pump using pneumatically actuated ball valves. This pneumatic valve is controlled by a 24 VDC signal and 60 to 120 psi (0.413 MPa to 0.827 MPa) pilot pressure line that allows for rapid on and off control of the pilot line. The fuel flow rates through two circuits were controlled by the motorized needle valves and measured by using a Micro Motion Coriolis flow meter with an accuracy of $\pm$ 0.030 % full scale deflection.

The needle valve coupled with ETI Systems electronic valve actuator provides flow adjustment to $\pm$ 0.1 lb/hr (0.045 kg/hr) [14]. The fuel can be flown through the chiller which can control the fuel temperature before it enters to the system.

Two fuel circuits were connected to a chiller, RC210 from FTS SYSTEMS SP SCIENTIFIC. The chiller uses a heat transfer fluid called, Duratherm XLT 120. The fluid has a capability of precise temperature control ranging from -120 $°F$ (-84 $°C$) up to 150 $°F$ (65 $°C$). The chiller has the capability to control the temperature range of -112 $°F$ (-80 $°C$) to 14 $°F$ (-10 $°C$). The control stability for this model is $\pm$ 0.1 $°C$

Fig. 3.8.: Fuel manifold assembly connected to fuel drum

3.6.2 Fuel Types and Physical Properties

The test fuels in this study are A-2, C-1, C-5, C-7, C-8, and C-9. The A-2 fuel (POSF 10325) is a Jet A procured from the Shell Mobile refinery in June 2013. The POSF numbering is a reference system established by Air Force Research Laboratory (AFRL) to uniquely define a fuel, its source, and batch number.

Figure3.9 shows the property range of the category A fuels with allowed limits. Eight different fuel properties are compared among three different category A fuels.

These properties are the density, flash point, freeze point, viscosity, aromatics, cetane number, and hydrogen content. The combustion-related properties that would be expected to have the greatest impact on combustor behavior are the flash point, viscosity, and aromatics content. As shown in Fig.3.9, the A-2 fuel is an average/normal property fuel among other category A fuels [6].

Colket et al. [6] described the category C test fuels as unusual and outside of experience, such as narrowly distributed aromatics at the front-end of the boiling range. The category C fuels include fuels with hydrocarbons confined to a narrow range of carbon numbers. The C-5 test fuel was created by blending 1,3,5 trimethyl benzene with a C_{10} iso-paraffinic solvent and designed to evaluate the impact of a very limited vaporization range of the fuel on combustor. This fuel also has a very low boiling point.

The C-1 test fuel is representative of a fuel composed of heavily branched iso-alkanes. This specific fuel has only two carbons numbers: C_{12} and C_{16}. C-1 has an extremely low derived cetane number relative to other fuels. By testing the C-1 fuel, the goal is to determine the effect of low cetane number on combustion [6].

Colket et al. [6] described the C-7, C-8, and C-9 as a high cycloparaffin, high aromatic, and high derived cetane respectively. These fuels were provided to this study as blind fuels, which the given information about the fuels was minimal. The purpose of testing these fuels was to compare the experimental data to the modelers' predictions of the spray characteristics based on the chemical compounds and physical

properties of the fuels. The fuel properties of testing fuels at Lean Blowout condition are shown in Table 3.1.
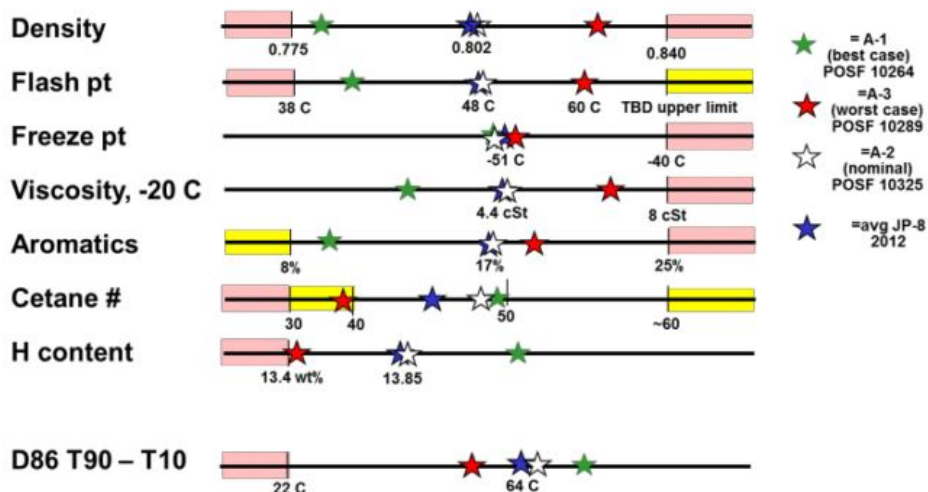
Fig. 3.9.: Property range of the category A conventional fuels with respect to allowed limits [6]

Table 3.1.: Test fuel types and physical properties at 120 °F (49 °C)

Fuel Property	A-2	C-1	C-5	C-7	C-8	C-9
ν $[m^2/s]$	$1.472{\times}10^{-6}$	$1.363{\times}10^{-6}$	$0.664{\times}10^{-6}$	$0.336{\times}10^{-6}$	$0.310{\times}10^{-6}$	$0.431{\times}10^{-6}$
σ $[N/m]$	0.024	0.021	0.022	0.025	0.025	–
ρ $[kg/m^3]$	780	736	741	795	801	736

* A-2 : average, C-1: C_{12} and C_{16} highly branched paraffins, C-5: 73 vol% C_{10} iso-paraffins

+ 27vol% trimethylbenzene, C-7: high cycloparaffin, C-8: high aromatic, C-9: high cetane

3.7 Spray Operating Parameters

The spray characteristics at lean blowout (LBO) conditions were measured as defined for the FAA NJFCP program in this study. For the LBO condition, the vessel pressure, fuel temperature, and vessel temperature were required to be 30 psia (2.07 bar), 120 °F (322 K), and 250 °F (394 K), respectively. Table 3.2 shows variable parameters and conditions for the spray measurements. $\Delta P/P$ represents the pressure drop across the swirler divided by the vessel pressure. ΔP_{pilot} is the differential pressure between the pressure in the fuel line and the vessel pressure. Thus, *psid* is used as an unit for the ΔP_{pilot} and indicates the differential pressure.

The uncertainties of the instrumentations that used in this experiment are provided by the manufacturers. For the instrumentation for the temperature and pressure measurement, the uncertainties are 0.75% and 0.045 % respectively. The uncertainties for the fuel injection pressure, fuel temperature, vessel temperature and airbox temperature are obtained using the standard deviation. They are 0.8 %, 3.6%, 1.6%, and 0.9% respectively. It is observed that the uncertainties from the measurements are bigger than the uncertainties from the instrumentations.

Table 3.2.: Spray Operating Conditions

Injector	OP	$\frac{\Delta P}{P}$ [%]	Fuel Flow Rate [lbm/hr]	ΔP_{pilot} [psid]
	1	2.00	20	25
	2	3.00	20	25
	3	4.00	20	25
	4	3.00	28.28	50
100 % Pilot	5	3.00	34.64	75
	6	2.00	28.28	50
	7	2.00	34.64	75
	8	6.00	20	25

* 20 lbm/hr = 9.07 kg/hr, 28.28 lbm/hr = 12.83 kg/hr, 34.64 lbm/hr = 15.71 kg/hr

* 25 psid = 1.72 bar, 50 psid = 3.45 bar, 75 psid = 5.17 bar

3.8   Phase Doppler Anemometry

Phase Doppler Anemometry is the primary diagnostic technique that was employed in this study. In this section, the basic principles of PDA are described. The mask selection for the receiving probe is also described. The dual-PDA system was available, but the 1-D Fiber PDA configuration was employed in this experiment due to a limitation of dual-PDA. The limitations of dual-PDA for this particular experiment set-up and the advantages of 1-D Fiber PDA are discussed. The alignment of

PDA system is critical for the measurement. Types of alignment that must be done before measurements are introduced. Lastly, the physical and software settings for the 1-D PDA system is described in this section.

3.8.1   Components of PDA

Phase Doppler Anemometry is the one of the most commonly used laser diagnostic techniques for measuring spray characteristics. The dual-PDA system from Dantec Dynamics was available for this study. The dual-PDA system consists of a 57x90 dual-PDA receiving probe, a Fiber Flow 60x24 transmitter with 60mm probe, and an argon-ion laser head from Spectra-Physics (Model 177-G0232).

The receiving probe carries the main optical components: front lens, aperture plate, spatial filter, composite lens, and alignment eyepiece. The probe is mounted on a 60X45 probe support with the 60x48 probe mount. The 60x45 probe support allows users to change orientation (pitch, yaw, back and forth) of the probe. The receiving optic probe has a 310-mm focal length front lens, and a 400-mm focal length lens is used in the transmitter probe.

Three standard aperture plates are available for the receiving probe: Masks A, B, and C as shown in Fig.3.11. The Mask A (large apertures) is used for the small particles, mask B (medium apertures) is for the medium particles, and mask C (small apertures) is for the large particles. The particle size sensitivity and range depend on which plate is used. Later in this chapter, the choice of mask is discussed.

The spatial filter has four different sizes of width (25, 50, 100, and 200 µm) and can be selected by a slit selector. An argon-ion laser from Spectra-Physics (Model 177-G0232) is used for the light source operating in multi-mode. The laser is powered by a 277-G0102 power supply and controlled by a 377G remote controller. This laser has an output power of 320 mW, a beam diameter of 0.74 mm, and a beam divergence of 0.89 $mrad$.

For signal processing, Dantec uses a 58N81 detector unit and a BSA P80 signal processor, which communicate with each other. Both the detector unit and the processor are configured for the dual-PDA system. The detector unit has four input photo-multipliers for the measurement of two velocity components and includes two interference filters for 514.5 nm (green) for the U1 and U2 channels and two 488 nm filters (blue) for the V1 and V2 channels [9]. The signal processor measures the phase differences between the Doppler signals from different detectors based on the light information that the detector unit received from the receiving probe. For this experiment, the dual-PDA configuration was converted to a 1-D Fiber PDA configuration by changing the interference filters. For the Fiber PDA system, the interference filters for 514.5 nm were connected to U1, U2, and V2/U3 channels, and 488 nm interference filter was connected to V1 channel. Details on the limitation of Dual PDA system for this particular experiment are discussed in section 3.8.3.
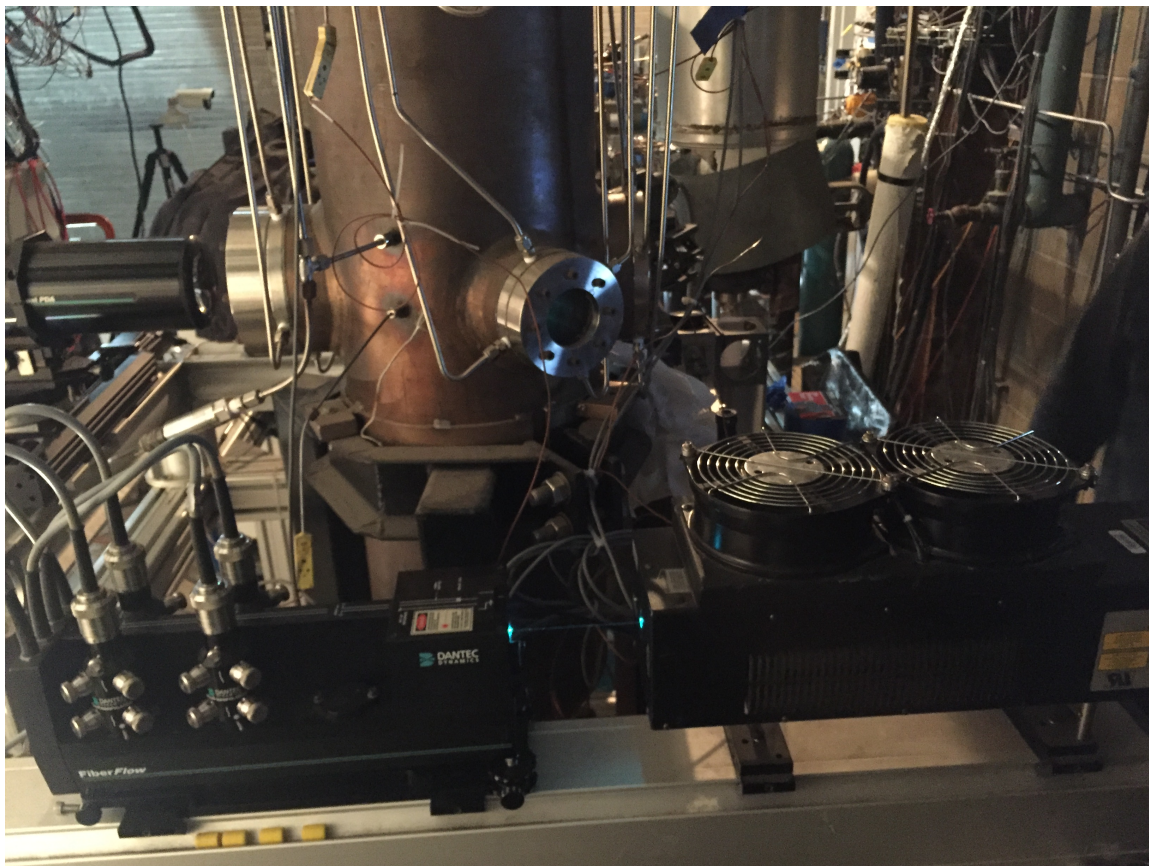
Fig. 3.10.: Laser head and splitter with manipulators

Fig. 3.11.: Three standard aperture plates for the optical receiving probe

3.8.2   Basic Principles of PDA

Figure 3.12 shows the layout of a 112-mm Dual PDA Probe. This receiving probe consists of a front lens, an aperture plate, an eye-piece, a spatial filter selector, a spatial filter, a segmented lens, and multi-mode fibers. When a fuel drop travels through the probe volume, the drop scatters the two incident beams as shown in Fig 3.13. The probe volume is the intersection between the two incident laser beams and defined as the volume within which the modulation depth is higher than e^{-2} times the peak core value. The shape of probe volume is an ellipsoid due to the Gaussian intensity distribution in the beams [9].

The scattered light from the drop surface may have different optical path length. This optical path length changes with the position of the photo-detectors. Both photo-detectors receive a Doppler burst of the same frequency, but the phases of two bursts change with the angular position of the detectors as shown in Fig 3.13 [9]. The amount of phase difference between two Doppler bursts depends on the size of the particles. The time lag between two bursts increasing as the particle size increases. However, this phase difference can increase beyond 2π when the size of particle is large enough. This generates an ambiguity in measuring the particle size. To resolve this problem, Dantec used three detectors: U1, U2, and U3. U1 and U2 form a greater slope of diameter-phase relationship, and U1 and U3 form a smaller slope of diameter-phase relationship. By comparing the phase differences from the two detector pairs, the true diameter can be determined. Details on the 2π Ambiguity can be found

in LDA and PDA Reference Manual [9]. The drop velocity can be measured from the Doppler-frequency. The magnitude of Doppler-frequency is proportional to the drop velocity. The velocity can have a negative value, and this produces a negative frequency. The receiving probe, however, can not distinguish whether the frequency is negative or positive. To resolve this directional ambiguity, a Bragg Cell is used to shift the frequency of one of the laser beams [9].

The scattered light from the drop surface then passes through the front lens, which works as a collimator creating a parallel light beam. The aperture plate followed by the front lens divides the parallel light beam into three segments corresponding to the photo-multipliers U1,U2,U3 for the Fiber PDA as shown in Fig. 3.14. The segments corresponding to U1,U2,V1,and V2 for the dual-PDA probe. The segmented light, then, is focused through a unique spatial filter. Through an alignment eyepiece, the image of the beam crossing on the spatial filter can be inspected. The part of the image which falls on the slit itself corresponds to the probe volume as shown in Fig. 3.15. Only the light from the probe volume is collimated to a segmented lens. Each part of the segmented lens guides the light into the multi-mode optical fibers then to the photo-multipliers [9]. The detector unit receives this light information through the photo-multipliers, and the signal processor measures the phase differences and the magnitude of Doppler-frequency based on given light information.
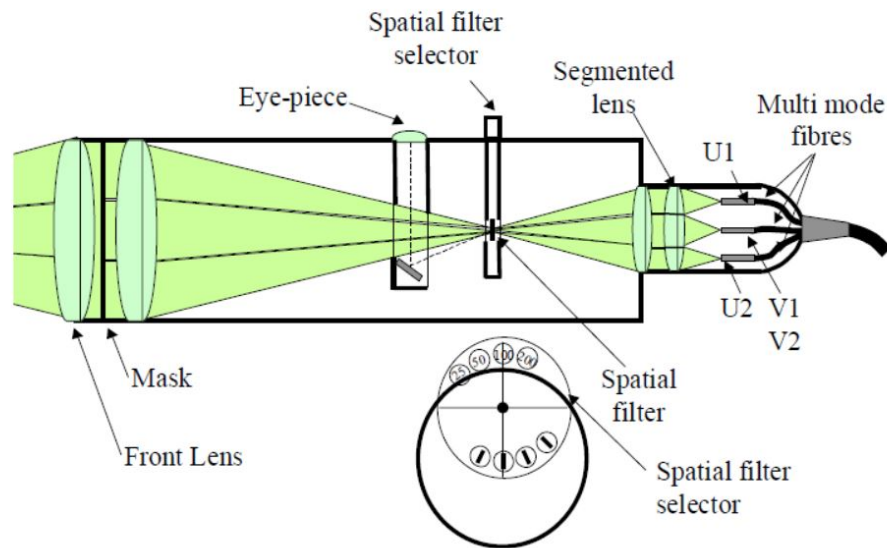
Fig. 3.12.: 112mm Dual PDA Probe (57x90). U1 and U2 are in the drawing plane and V1 and V2 are in the plane perpendicular to the drawing plane [9]

(a)

(b)
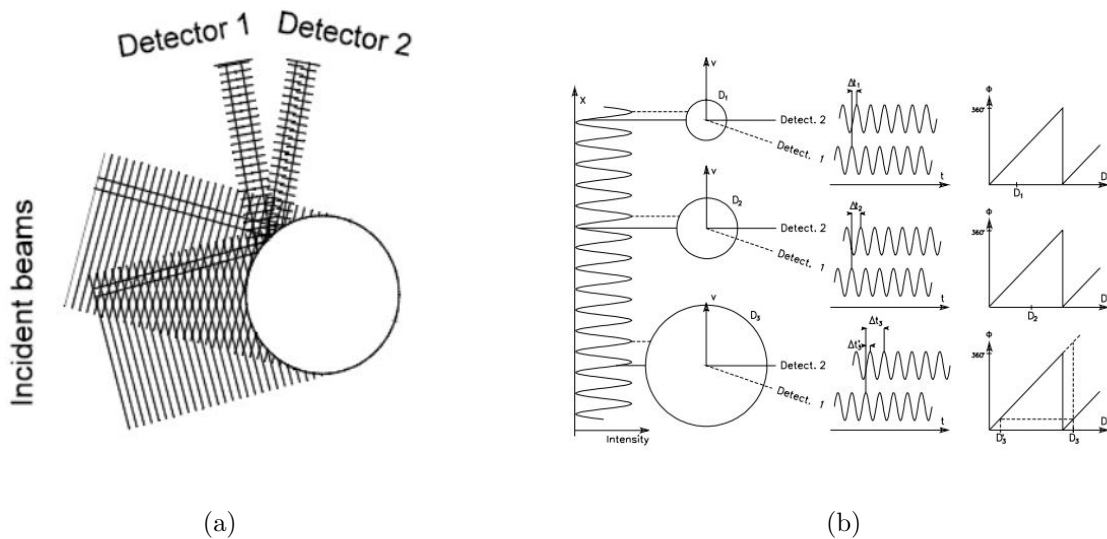
Fig. 3.13.: (a) The interference patterns differ at the two photo-detector surfaces [9], (b) Illustration of the intensity fluctuation in each of the photodetectors and the time lag, Δ t, separating the wave fronts reaching the two photodetectors [9]

Fig. 3.14.: Polarization definition for 1D PDA [9]

Fig. 3.15.: Image of the beam crossing on the spatial filter [9]

3.8.3 Limitation of Dual PDA system

The configuration of the dual-PDA system and the BSA software can be changed into four different measurements settings: Classic PDA, 2D PDA, 112-mm Fiber PDA, and 112-mm dual-PDA. The 112-mm dual-PDA configuration was not used for

this experiment due to a limitation of the scattering angle imposed by the spray test rig.

The feature of dual-PDA is that both conventional PDA and planar PDA are used in the measurement system. Figure 3.16 shows the phase/diameter conversion factor depending on the particle refractive index for various scattering angles for conventional PDA and planar PDA. The phase factor for the planar PDA is much lower than the conventional PDA as the scattering angle increases. This means that the phase difference that the receiver probe sees is much smaller with for planar PDA. Therefore, the measurement noise has a much larger effect on planar PDA. This can cause degraded measurement resolution, and the resolution gets worse as the scattering angle increases for planer PDA. Figure 3.18 also shows that the V12 phase factor decreases as the scattering angle increases. Therefore it is recommended the scattering angle be between 20 degrees to 40 degrees for the dual-PDA configuration. The orientation of windows on the pressure vessel, however, were such that the scattering angles were restricted to approximately 60 degrees and 120 degrees.

On the other hand, the phase factor for conventional PDA is much higher than for planer PDA for scattering angles in the range of $20° \sim 75°$. In other words, the measurement resolution for conventional PDA is better at these scattering angles than the resolution from planar PDA.

The 2-D PDA configuration was another option instead of Dual PDA. However, the polarizations of the laser were changed to factory reset (parallel) while the transmitter was being refurbished. The 2-D PDA requires both parallel and perpendicular

polarizations. With incorrect polarizations, the data rate and validation of the mea-

surements with 2D PDA were observed to be very poor. A lack of hands-on experience

in changing the polarizations for the sensitive laser system led to a decision to keep

the polarizations at their factory settings. Thus, it was concluded that the 1-D PDA,

which uses the conventional PDA, is the best configuration with the scattering angle

of 60 degrees for this experiment.
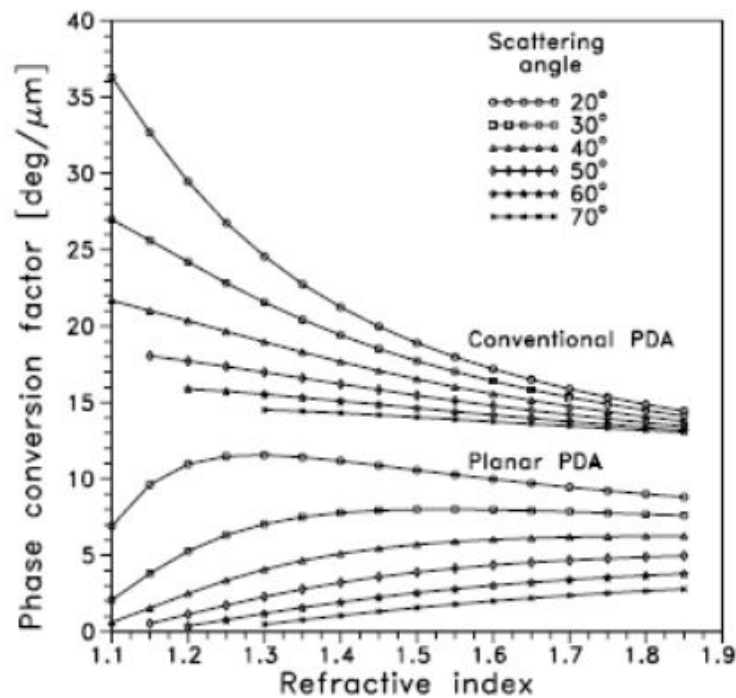
Fig. 3.16.: Phase/diameter conversion factor versus particle refractive index for various scattering angles [9]
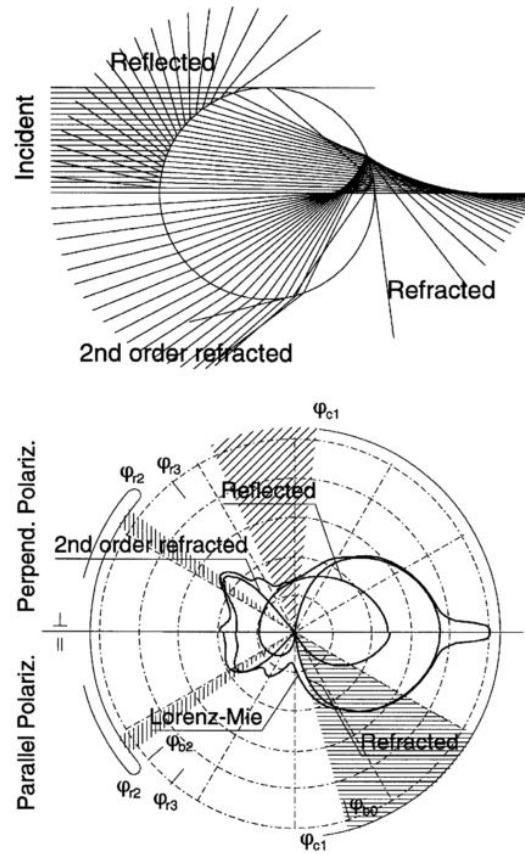
Fig. 3.17.: Top:ray traces indicating the three modes of scattering, refraction, 2nd order refraction, and reflection, for a water drop. Bottom: the scattering chart. The light intensity for each of these modes is shown in a polar plot for scattering angles from 10° to 180° and for two polarizations-the upper half is for perpendicular polarization, adn the lower half is for parallel polarization [9]
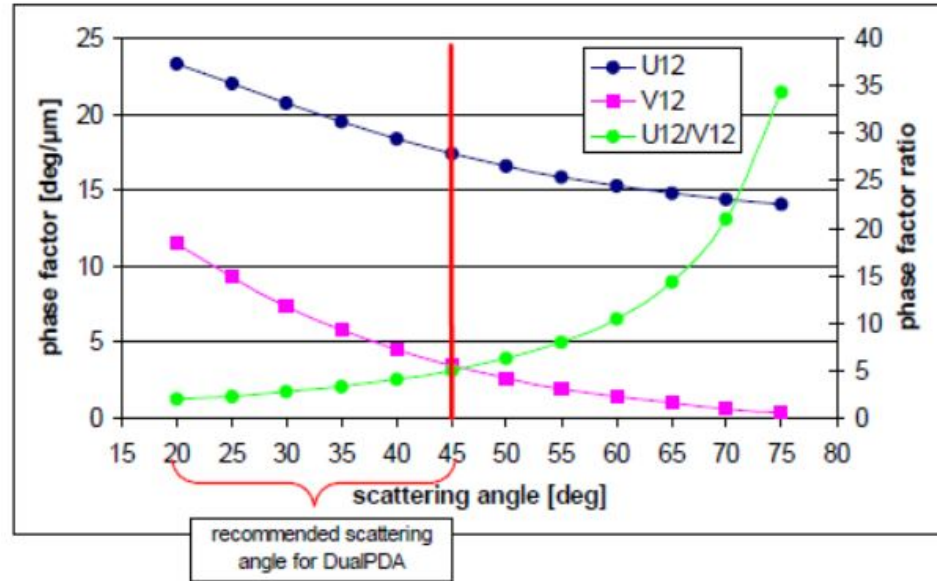
Fig. 3.18.: Phase/diameter conversion factor versus scattering angle for water droplets [9]

3.8.4 Mask selection

The selection of three Masks (aperture plates) is available for 1-D Fiber PDA. It is important to use the proper Mask depending on the produced drop sizes. For instance, if Mask C, which is for the large droplets, is used for small drop size spray application, a significant number of the small droplets will not be detected but detect most of the large drops instead. This can shift the drop size distribution to the larger values and gives a skewed drop size measurement.

The maximum drop diameter that can be measured with Mask A at the scattering angle of 60 degree is approximately 95 μm. With the Mask B, it is 153 μm and 364 μm for the Mask C. The measurement dynamic range for each Mask is approximately 1:50. The investigation was done with C-3 fuel at $\Delta P/P = 3\%$, $\Delta P_{pilot} = 25$ psi, fuel

temperature of -34 °C. The largest drop size produced by the current atomizer is around 100 µm. Thus, the Mask C was excluded in this investigation since its drop diameter range is too wide for this atomizer spray drop sizes.

Table 3.3 shows the mean drop diameters for Mask A and B. Figure 3.19 shows the comparison of number probability density function of diameter for Mask A and B. 20,000 samples are collected for each test. A bin size is 120 for this PDF and bin width is 1 µm to obtain detailed resolution.

As shown in Table 3.3, the mean drop diameters vary considerably for the different aperture plates. This indicates that selecting an appropriate aperture plate is an important task. Figure 3.19 shows that the drop distribution for Mask B has lower peak than that for Mask A. In addition, the drop distribution for the Mask B is shifted to right due to the large drop diameters. From the comparison, it can be seen that the Mask A can pick up more small drops than the Mask B can do. In other words, the Mask B misses many of the small drops and this leads to a skewed drop distribution and incorrect D_{32}. Therefore, Mask A is selected for this experiment.
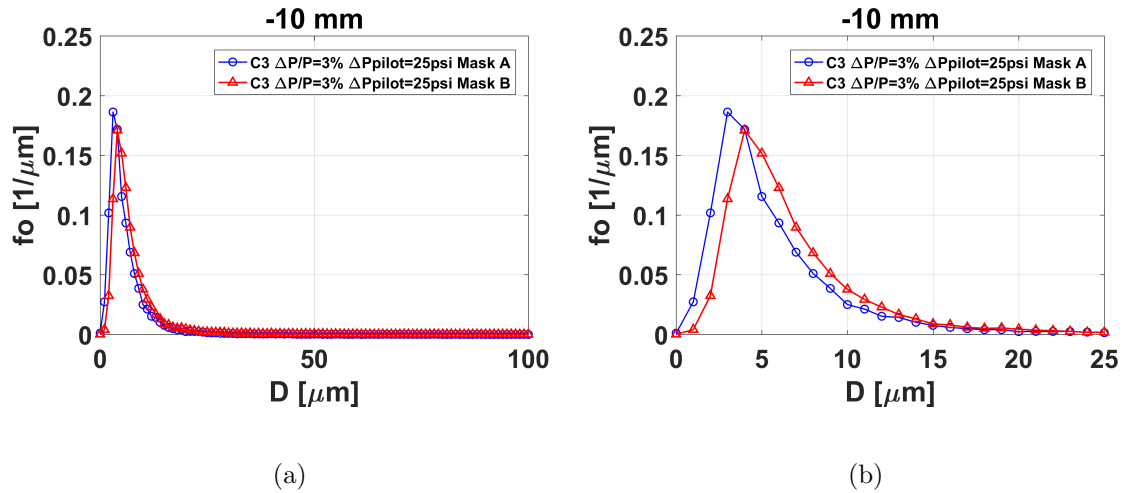
Fig. 3.19.: (a) Comparison of number PDF of diameter for Mask A and B at r=-10 mm, (b) Number of PDF versus truncated drop diameter for Mask A and B

Table 3.3.: Mean drop diameters with Mask variation.

Aperture plate	Radial Location	D_{10} [µm]	D_{32} [µm]	MMD [µm]
	-30 mm	11	42	54
	-20 mm	11	50	65
Mask A	-10 mm	7	32	55
	0 mm	6	16	21
	-30 mm	13	53	65
	-20 mm	14	67	75
Mask B	-10 mm	8	35	54
	0 mm	7	24	39

3.8.5   PDA Alignment

Alignment is a critical issue in PDA measurements. There are three major alignments must be performed for this experiment: laser alignment, transmitter alignment, and probe alignment. The purpose of the laser alignment is to align the laser to the transmitter in order to ensure a well-specified beam path through the transmitter. It is recommended to lower the laser power to 50 mW before proceeding with the laser alignment to prevent uncontrolled laser amplification. The transmitter is mounted on the mounting rail 15 cm apart from the laser head. There is a sliding switch on top of the transmitter to select the main path or the alignment path. By switching from the main path to the alignment path, a matt glass plane with a central hole can be seen. The position of transmitter needs to be adjusted to align the transmitter correctly to the incoming laser beam so that any reflected beam can be centered on the incoming laser beam. By adjusting two front feet and one back foot on the transmitter, it can be adjusted vertically and horizontally at the front and rear of its mounting support. After the alignment, the laser powers from the manipulators were approximately 40 mW for the green beams and 30 mW for the blue beams. A detailed alignment procedure can be found in the FiberFlow Installation and User's guide manual [11].

The transmitter alignment optimizes the coupling of the laser beams from the transmitter to the optical fibres, which are connected to the transmitter. The manipulators mounted on the transmitter position the laser beams on the exact center of the optical fiber core and corrects the incoupling angle [11]. This gives the maximum

laser output power at the probes. For this alignment, it is also recommended to lower the laser power to 50 mW or lower. By pressing a tiny circular slot on each surface of manipulator port on the transmitter, the shape of the laser and the power of laser distributed to each manipulator can be checked. The coupling of the laser beam to the optical fiber can be optimized by adjusting a thumb screw and four knob screws on the manipulators. Prior to the alignment, the thumb screw and four knob screws were set at the neural marks that are on each screws. Then, the thumb screw was turned counterclockwise until it reached the limit. The screw was turned to clockwise slowly until the laser beam from the probe was barely visible. By adjusting the four knob screws individually (in order of top left and right then bottom left and right), the laser power from the probe that corresponds to the manipulator increased slowly until it reaches maximum power. According to the technician from Dantec Dynamics, it is recommended to drop it down to its half of the power using just thumb screw. Then, it is recommended to increase the laser power again using just four knob screws.

The optimization was done by repeating this procedure until the laser power reaches its true maximum power. If the laser power reaches to its maximum, any more adjusting the thumb screws and knob screws will decrease the laser power. After the optimization, the laser powers from the transmitter probe were approximately 26 mW for the green beams and 9 mW for the blue beams. Since 1D PDA uses only conventional PDA (green beams), it was focused to obtain the highest power output for the green beams. Figure 3.21 shows the comparison of probability density functions for two measurements with two different laser powers. More small droplets

were detected with higher laser power than the lower laser power. Therefore, it is an important task to get a high laser power from the transmitter probe. Once this alignment is finished, the transmitter and probe are ready for the measurement.

Lastly, the probe alignment was done. The probe alignment is to position the probe volume at the center of the spray. For this alignment, a customized alignment tool was fabricated as shown in Fig. 3.20. This alignment tool is consist of two parts: atomizer housing cup and alignment pin. This housing cup is designed to slide-fit to the air swirler housing of the hybrid atomizer that used in this experiment. There are two threaded holes for the holding screws. The alignment pin is a steel shoulder style precision ejector pin and has 1/32 inch (0.79 mm) pin diameter with 6 inch (152.4 mm) overall length. This pin sits on the bottom of the surface of the housing cup. The center of the atomizer is aligned with the center of hosing cup where the alignment pin sits on. When the probe volume is located at the center of the atomizer, it is blocked by the alignment pin since the size of the probe volume is much smaller than the pin diameter. Thus, it can ensure that the probe volume is located at near the center of the atomizer.

(a)

(b)
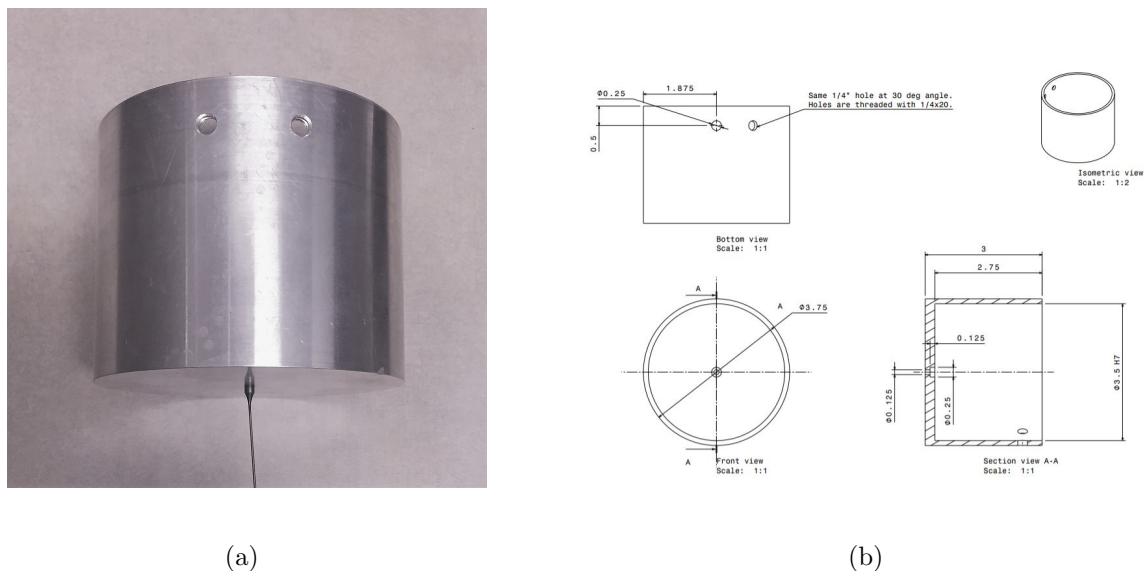
Fig. 3.20.: (a) Alignment tool that helps the PDA to find the center of spray, (b) Dimension of the alignment tool cup
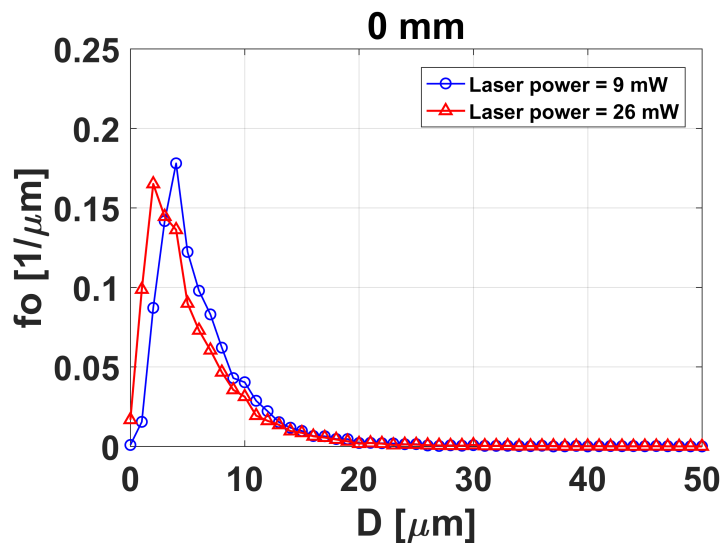
Fig. 3.21.: Comparison of probability density function for two measurements with different laswer power. The measurements were obtained under LBO condition with A-2 at $\Delta P/P = 3\%$, $\Delta P_{pilot} = 25$ psi at the center of spray

3.8.6   1D Fiber PDA Physical Setting

Figure 3.22 and 3.23 show a diagrams of the PDA system around the pressure vessel. The optical receiving probe and the transmitter probe are mounted on Zaber stages. The Zaber stage is a motorized linear transverse stage that allows the receiving probe and the transmitter probe to move to their alignment positions and to different radial locations in spray. Two identical Zaber stages, A-LST0250A-E01 models, were used for the receiving probe and the transmitter probe. This Zaber stage model has a microstep size of 0.12402 µm and can travel up to 254 mm with maximum speed of 22 mm/s and minimum speed of 0.0000757 mm/s.

The receiving probe and transmitter probe sit in front of the 5 inch and 3 inch windows respectively. The front lens of each probe and the windows are parallel each other. Two probes need to be in the same plane so that the probe volume can be centered in the receiving probe front lens. The range of movement for the transmitter probe is limited by the size of window. This allows the probe to move no more than -30 mm and +30 mm in radial location of spray.
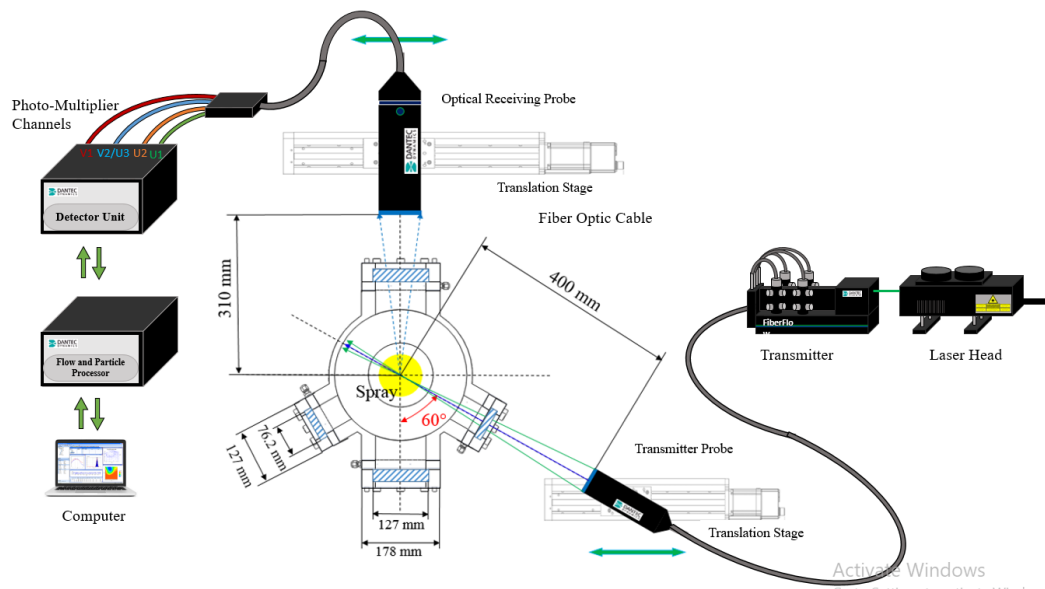
Fig. 3.22.: Schematic diagram for PDA set-up
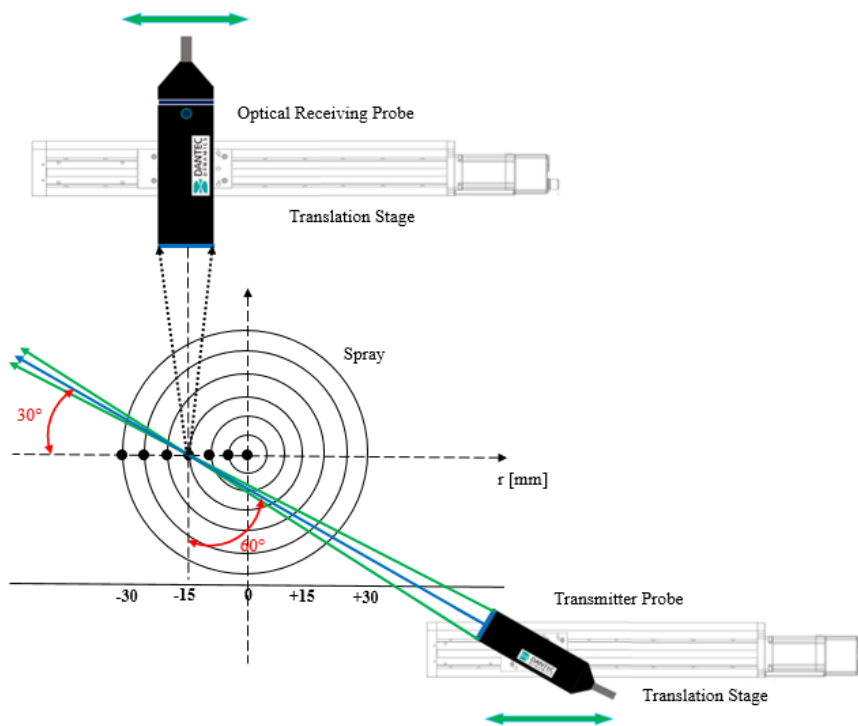
Fig. 3.23.: Schematic diagram for spray measurement points with PDA.

3.8.7   1D Fiber PDA Software Setting

A trial and error method was used to determine the optimum parameters based on the validation, spherical validation, quality of bursts and phase plot, and data rate. These parameters can be optimized by changing the Sensitivity, Signal Gain, and Record length.

The Sensitivity sets the high voltage level to the photo-multiplier. Test was conducted with varing the Sensitivity from 700 V to 1200 V on PDA1, LDA2, and LDA3 while keeping other parameters constant. The Signal Gain is the gain of the photo-multiplier signal amplifier. The Signal Gain of PDA1 was varied from 18 dB to 22 dB while keeping all other parameters constant. The Record Length of PDA1 was varied while keeping other parameters constant. The Record Length is closely related to the Bursts length. If the burst is longer than the record length, only the part within the record interval is used for the frequency estimation. Record Length was tested with values of 64, 128, and 256. Many different sets of combinations can be made with varing these parameters. The optimized setting can be determined by checking the quality of phase plot and bursts, validation, spherical validation, and data rate. Table 3.22 shows the optimized software setting for this particular experiment.

Table. 3.22.: Optimized BSA software settings for 1D PDA

Start\Stop	
Start Actions	Start Independently
Stop Actions	Stop Independently
Stop events	(No stop events defined)
Stop event actions	Stop on every stop event
Traverse	
Disable traverse	Yes
Prompt before region	No
Prompt before position	No
Bypass errors	No
Wait before error	60 sec
Delay between positions	0 sec
Lasers	
Disable lasers	No
Activate method	Automatic activation
Delay for lock	10 sec
Miscellaneous	
Save method	After each position
Send email	No
Automatic apply lock	No
Allow skipping positions	Yes
Acquisition timeout	300 sec
Acquisition and monitor	
Max. Samples	20000
Max. acquisition time	10000 sec
Coincidence method	Overlapped
Coincidence window	10 µs
Scope display	Burst signal
Scope zoom	800%
Scope trigger channel	Individual
Range and gain (LDA1)	
Center Velocity	Varies
Velocity span	Varies
Record length mode	Fixed
Record length	128
Maximum record length	256
Sensitivity	700 V
Signal gain	18 dB
Burst detector SNR level	1 dB
Anode current limit	1500 µA
Level validation ratio	4

Range and gain (PDA2)	
Sensitivity	700 V
Balance high voltage	Yes
Range and gain (PDA3)	
Sensitivity	700 V
Balance high voltage	Yes
Optical PDA System	
Beam system U1	
Wavelength	514.5 nm
Focal length	400 mm
Beam diameter	1.350 mm
Expander ratio	1
Beam spacing	38 mm
Frequency shift	40 MHz
Laser mode	Uncontrolled
PDA Receiver	
Reciever type	112 mm Fiber PDA
Scattering angle (deg)	60 deg
Reciever focal length	310 mm
Reciever expander ratio	1
Fringe direction	Positive
Scattering mode	Refraction
Aperture mask	Mask A
Phase ratio validation	20%
Spatial filter	Slit: 0.200 mm
Particle properties	
Particle name	Jet A
Particle refractive index	1.444
Particle specific gravity	1
Particle kinematic viscosity	0.001 m^2/s
Medium properties	
Medium name	Nitrogen
Medium refractive index	1
Medium specific gravity	1
Medium kinematic viscosity	0.001 m^2/s
Window correction	
Window type	None
Eff. Scattering angle	60 deg

3.9   Shadowgraphy and High Speed Imaging

For the cone angle measurement, shadowgraph imaging with high speed camera was employed. Figure 3.24 shows the schematic diagram of the shadowgraphy system for the cone angle measurement.

A Photron FASTCAM SA4 high speed camera was used to obtain shadowgraph images. High speed videos was recorded at 8000 fps with a resolution of 512×512. A Nickon 50 mm focal length lens was used to focus on the spray within the vessel. A fiber optic dual gooseneck microscope illuminator(AmScope HL250-AY) was used to supply the back light for the shadowgraph images. The high speed camera was mounted on sliders and a lab jack to align the camera with one of the 127 mm windows. The light source was directed at and diffused by a opaque glass and entered the vessel through the opposite 127 mm window.

The measurements on the full cone angle have been done for A-2, C-1, and C-5 fuels. The pressure drop across the swirler and the fuel injection pressure were varied to investigate the effect of those parameters on the full cone angles. A simple imaging processing technique was employed to process the images to determine the full cone angles. A detailed analysis procedure can be found in Bokhart et al. [3].
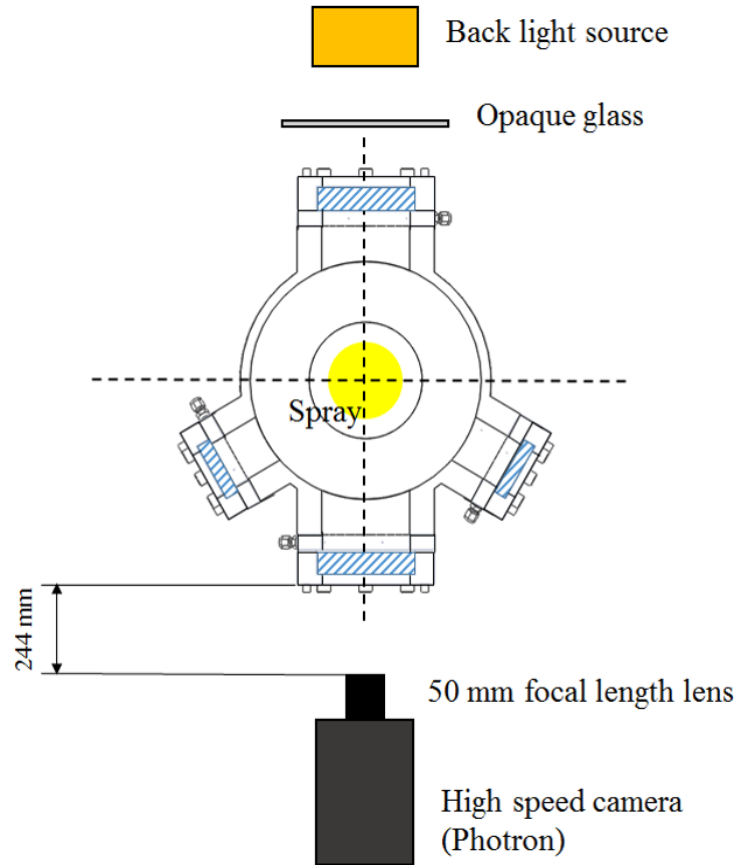
Fig. 3.24.: Schematic diagram for the shadowgraphy set up for the cone angle measurement.

4. RESULTS AND DISCUSSION

4.1   Introduction

The results and discussion are presented in this section. The arithmetic mean diameter (D_{10}), Sauter Mean Diameter (D_{32}), and Mass Mean Diameter (MMD) are used to characterize the drop size of the spray in this study. The mean axial velocity (U_z) and Root-Mean-Square (U_{rms}) of mean axial velocity are used to characterize the drop velocity in the spray. The Weber number (We) and Ohnesorge number (Oh) are used to determine the break-up regimes of the droplets.

In this study, the pressure drop across the swirler is defined as $\frac{\Delta P}{P}$. This is the differential pressure between the airbox and the vessel divided by the vessel pressure. Changes in the $\frac{\Delta P}{P}$ result in changes in atomizing gaseous flow velocity. This parameter can be obtained by

$$\frac{\Delta P}{P} = \frac{AirboxPressure - VesselPressure}{VesselPressure} \times 100 \qquad (4.1)$$

The fuel injection pressure is expressed as ΔP_{Pilot}. Due to the vessel pressure (30 psia), the fuel is injected at a 30 psi higher pressure to obtain the desired injection pressure. This parameter dictates the fuel flow rate.

All measurements presented in this study were taken at 1 inch (25.4 mm) downstream from the swirler exit with a vessel pressure of 30 psia (2.07 bar), vessel temperature of 250 $°F$ (394 K), and fuel temperature of 120 $°F$ (322 K).

4.2   Spray Profile and Repeatability

For this study, the measurements on the negative radial locations of the spray are presented. Spray symmetry was observed by taking additional data on the positive radial locations. Figure 4.1 shows the profiles of the mean drop size and axial velocity for A-2. Both the mean drop size profile and axial velocity profile show that the spray produced by the hybrid atomizer is symmetric. The uncertainty bars on the mean drop size at each radial location are the standard deviations of 10 repeated measurements. The uncertainty bars on the axial velocity are the root mean square (RMS).

From the mean drop size profile, it is observed that the smaller droplets dominate at the center of the spray and the larger droplets dominate near the radial location of -20 mm. In addition, the larger droplets are observed to travel at higher velocities. This is due to a higher inertia dictated by the initial tangential force from the atomizer. The larger droplets have enough momentum to travel radially outward away from the center of the spray. The smaller droplets, however, do not and are trapped within the hollow cone. As shown in the axial velocity plot, these smaller droplets are traveling with positive axial velocity. In other words, these droplets are moving towards the injector nozzle. This zone is defined as the recirculation zone and

is discussed in a later section. Beyond the radial location of -20 mm, the drop size and the axial velocity tend to decrease due to entrainment and turbulent mixing with the surrounding ambient nitrogen. The smaller droplets tend to follow the gaseous flow streamlines closely. However, the flow creates turbulence by mixing with the surrounding nitrogen at the edge of the spray. This results a decrease in the velocity of the smaller droplets at the spray edge.
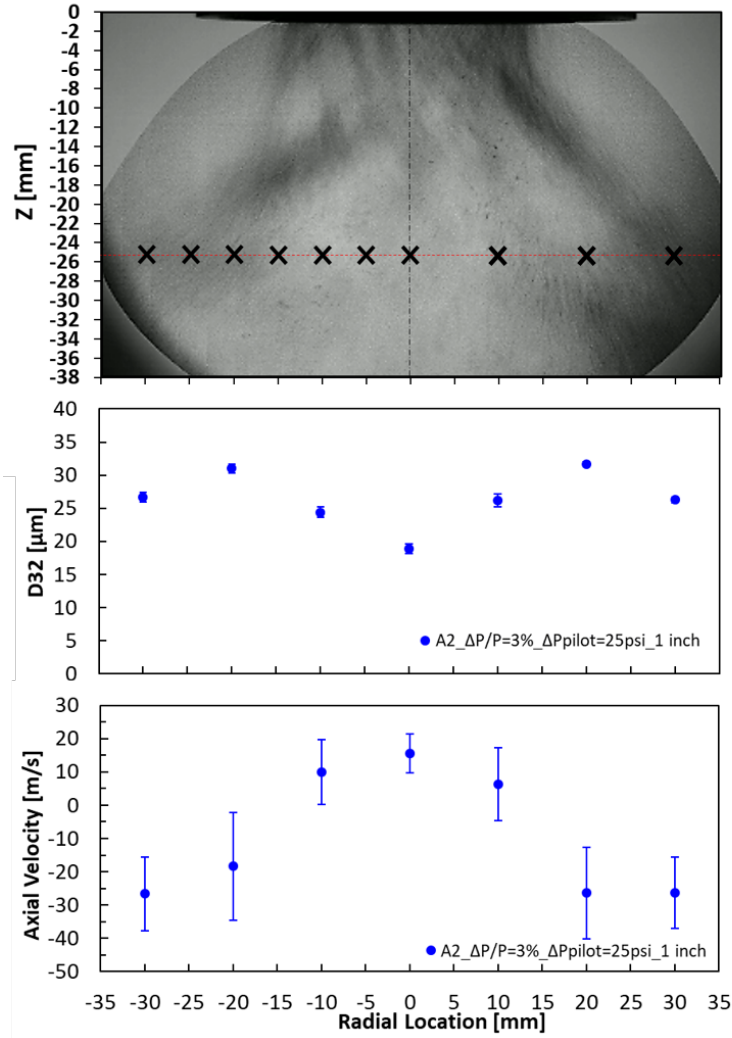
Fig. 4.1.: Top: shadowgraphy image of the spray with the measurement locations. The red dashed line indicates the measurement plane at 1 inch (25.4 mm) and the black dashed line is the center line of the spray. The x markers are indicating the measurement locations at 1 inch plane. Middle: mean drop size for A-2 with uncertainty bars. Bottom: axial velocity for A-2 with uncertainty bars. The symmetry of the spray structure is shown. The operating conditions are $\frac{\Delta P}{P} = 3$ %, $\Delta P_{Pilot} = 25$ psi, $T_{Fuel} = 120$ °F, $T_{Airbox} = 250$ °F

Figure 4.2 shows the half radial spray measurement for A-2. The uncertainties for the D_{32} are the standard deviations of 21 repeated measurements taken on three different measurement days. The average uncertainty for D_{32} across the radial locations

is approximately ±0.9 µm. The average uncertainty, not RMS, for the axial velocity

across the radial locations is approximately ±0.6 m/s. It can be argued that the

repeatability of the measurements is well established. The plots with the uncertainty

bars for C-1 and C-5 can be found in the Appendix A. The average uncertainties for

D_{32} and axial velocity for the three fuels are ±0.7 µm and ±0.6 m/s respectively.

These average uncertainties are considered as the overall PDA uncertainties in this

experiment. The numerical data for A-2 is shown in Table 4.1.
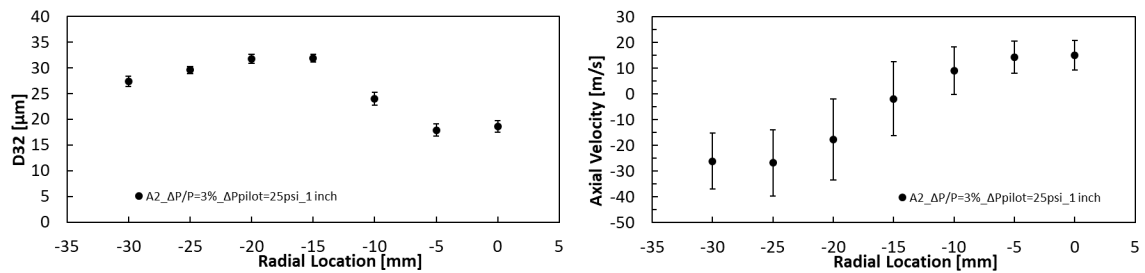
(a) Mean drop size for A-2 with uncertainty bars. (b) Axial velocity for A-2 with uncertainty bars.

Fig. 4.2.: D_{32} **and Axial velocity for A-2 at** $\frac{\Delta P}{P} = 3$ **%,** $\Delta P_{Pilot} = 25$ **psi,** $T_{Fuel} = 120$ °F**,** $T_{Airbox} = 250$ °F

Table 4.1.: Numerical Data for D_{32} (±uncertainty), Axial velocity, RMS, Spherical Validation, Validation for A-2 at $\frac{\Delta P}{P} = 3$ %, $\Delta P_{Pilot} = 25$ psi, $T_{Fuel} = 120$ °F, $T_{Airbox} = 250$ °F

r	D_{32}	Axial Velocity	RMS	Spherical Validation	Validation
[mm]	[µm]	[m/s]	[m/s]	[%]	[%]
-30	27 ±1.21	-26.06	±10.88	94	94
-25	29 ±1.08	-26.79	±12.94	95	94
-20	31 ±1.17	-17.75	±15.76	93	93
-15	32 ±0.75	-1.85	±14.36	94	95
-10	24 ±2.03	9 .17	±9.21	94	97
-5	18 ±1.56	14.34	±6.35	96	97
0	19 ±1.35	15.09	±5.78	96	97

4.2.1 Weber number and Ohnesorge number

The Weber number and Ohnesorge number are calculated for each radial location using the drop diameters measured on 1 inch (25.4 mm) plane. Figure 4.3 shows plots of the Weber number versus Ohnesorge number for each fuel at different operating conditions. The numerical values are tabulated and can be found in Appendix C. The Weber numbers did not vary significantly with the fuel injection pressure nor the pressure drop across the swirler. Furthermore, it is observed that the Weber numbers are less than 1 for all cases.

Ohnesorge numbers, on the other hand, are less than 0.1 for C-5, C-7, and C-8, but for A-2 and C-1 the Ohnesorge numbers are slightly higher than 0.1. This is due to the higher viscosity of A-2 and C-1 compared to the other fuels. Guilldenbecher, et al. [15] reviewed the transition We for Newtonian drops with $Oh < 0.1$ for each

break-up mode. In addition, the author provided the We at transition plot from the work of Hsiang, et al. [16]. Based on the work from Guilldenbecher and Hsiang, it is concluded that the spray drops at the 1 inch (25.4 mm) plane are not experiencing any break-up modes since the authors' defined drop Weber numbers less than 11 as a vibrational mode or deformation regime.

From this analysis, it can be argued that the secondary break-up has already occurred before the drops reach the 1 inch (25.4 mm) downstream location. For this reason, additional measurements near the swirler nozzle exit may be necessary in future work to find the secondary break-up location in the spray. The PDA technique, however, has limitations with dense sprays. Alternative measurement techniques may be necessary for this investigation.
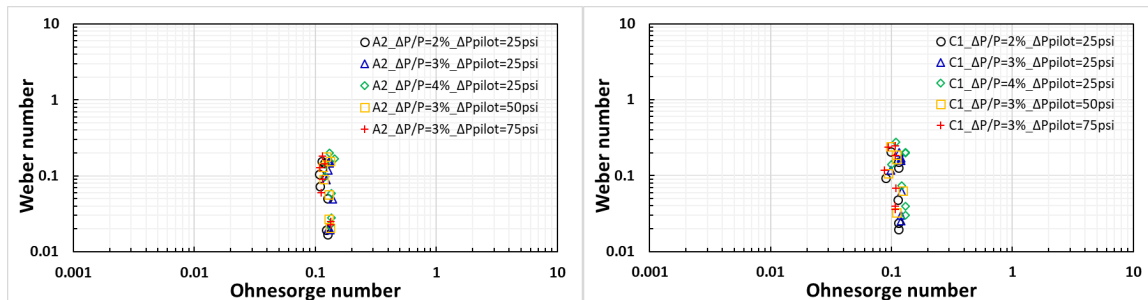
(a) We versus Oh plot for A-2

(b) We versus Oh plot for C-1
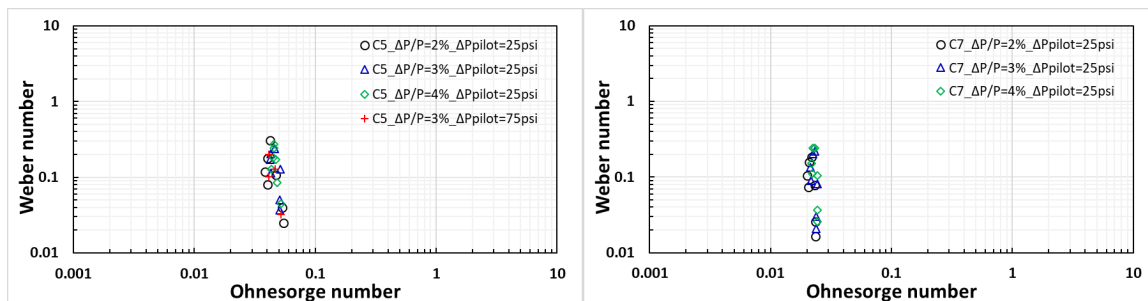
(c) We versus Oh plot for C-5

(d) We versus Oh plot for C-7
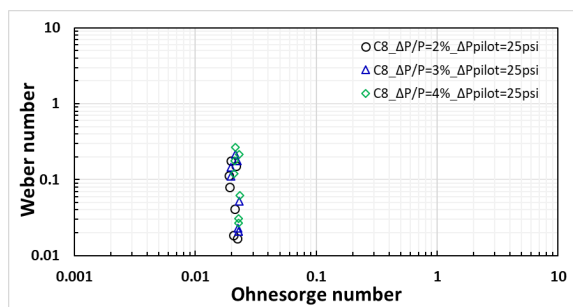
(e) We versus Oh plot for C-8

Fig. 4.3.: Weber number vs Ohnesorge number.

4.3   Influence of Fuel Injection Pressure on Spray Characteristics

4.3.1   Drop Size and Velocity

The pilot injection pressure differential was investigated at 25 psid, 50 psid, and 75 psid. This parameter dictates the mass flow rate of fuel through the injector. Thus, a higher injection pressure leads to a higher liquid velocity due to mass conservation and a thinner liquid film develops. The fuel flow rates that were obtained with each fuel injection pressure were 20 lbm/hr, 28.28 lbm/hr, and 36.46 lbm/hr (9.07 kg/h, 12.83 kg/h, 15.71 kg/hr) respectively. As shown in Fig.4.4, the effect of fuel injection pressure on the mean drop size and axial velocity is minimal for A-2, C-1, and C-5. This is an interesting finding because the previous work done by Buschhagen et al. [4] shows that the increase in the fuel injection pressure decreased the mean drop size by approximately 5 to 8 % beyond the radial location of -10 mm and 30 % at the center of the spray using the same hybrid atomizer as this investigation. Buschhagen et al., however, performed their study at different operating conditions such as lower fuel temperature, lower ambient pressure, etc. It can be argued that the combination of different operating parameters may exert influence on the mean drop size and axial velocity. Further investigation is necessary to explain this phenomena. D_{10}, D_{32}, and MMD are tabulated and shown in Table 4.2 $\sim$ 4.4. Minimal changes occurred in D_{10} and MMD as a result of the fuel injection pressure differential variation.
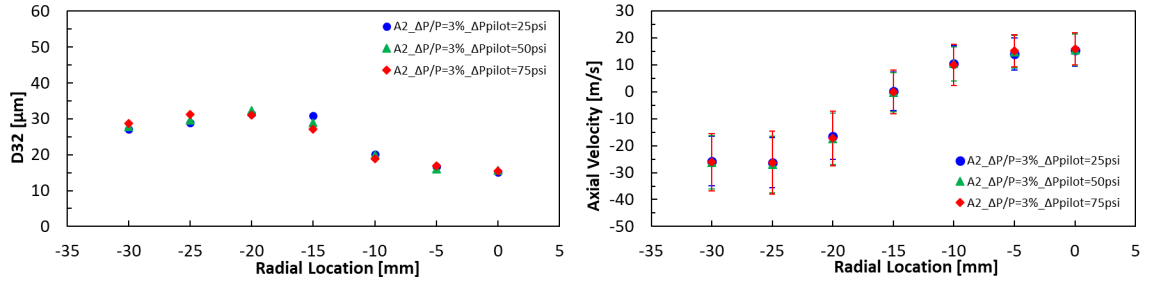
(a) Mean drop size with ΔP_{Pilot} variation for A-2.

(b) Axial velocity with ΔP_{Pilot} variation for A-2.
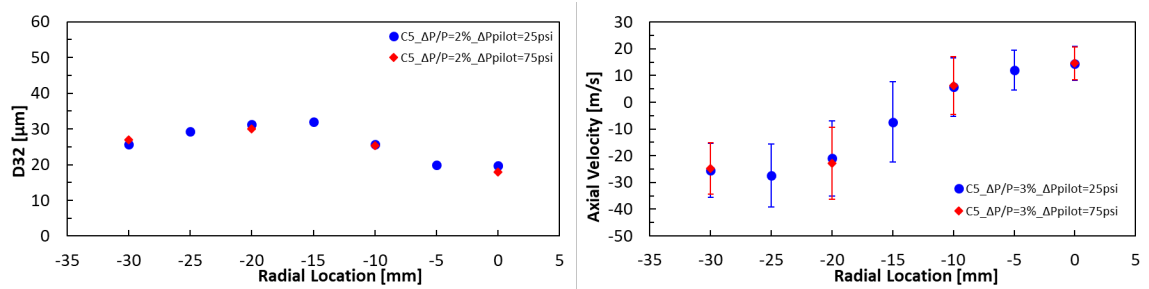
(c) Mean drop size with ΔP_{Pilot} variation for C-5.

(d) Axial velocity with ΔP_{Pilot} variation for C-5.
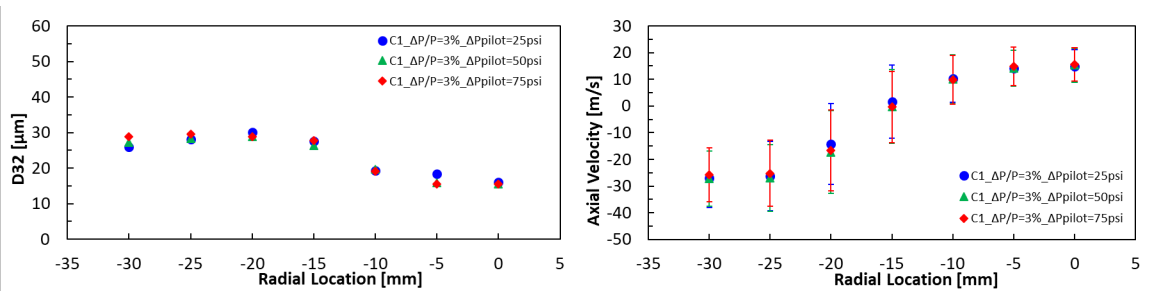
(e) Mean drop size with ΔP_{Pilot} variation for C-1.

(f) Axial velocity with ΔP_{Pilot} variation for C-1.

Fig. 4.4.: D_{32} and Axial velocity with ΔP_{Pilot} variation for A-2, C-5, and C-1 at $\frac{\Delta P}{P} = 3$ %, $T_{Fuel} = 120\ ^\circ F$, $T_{Airbox} = 250\ ^\circ F$

Table 4.2.: Mean drop diameters with ΔP_{Pilot} variation for A-2 at $\frac{\Delta P}{P} = 3$ %, $T_{Fuel} = 120$ °F, $T_{Airbox} = 250$ °F

ΔP_{Pilot}	r [mm]	D_{10} [µm]	D_{32} [µm]	MMD[µm]
	-30	13	27	32
	-25	13	29	34
	-20	13	32	39
25 psi	-15	11	31	44
	-10	9	21	31
	-5	8	17	21
	0	8	17	21
	-30	10	28	33
	-25	10	30	35
	-20	10	33	41
50 psi	-15	7	29	40
	-10	6	20	28
	-5	6	16	19
	0	6	16	19
	-30	11	29	33
	-25	12	32	36
	-20	10	32	39
75 psi	-15	8	28	38
	-10	8	19	23
	-5	6	17	20
	0	6	15	18

Table 4.3.: Mean drop diameters with ΔP_{Pilot} variation for C-1 at $\frac{\Delta P}{P} = 3$ %, $T_{Fuel} = 120\ ^\circ F$, $T_{Airbox} = 250\ ^\circ F$

ΔP_{Pilot}	r [mm]	D_{10} [µm]	D_{32} [µm]	MMD[µm]
	-30	12	26	29
	-25	13	27	31
	-20	13	29	35
25 psi	-15	11	30	38
	-10	9	21	28
	-5	9	17	20
	0	9	17	19
	-30	12	27	32
	-25	12	29	32
	-20	11	30	35
50 psi	-15	8	27	36
	-10	6	20	26
	-5	7	16	19
	0	7	16	18
	-30	13	29	33
	-25	14	30	34
	-20	11	30	35
75 psi	-15	8	29	38
	-10	8	19	24
	-5	7	15	18
	0	7	17	19

Table 4.4.: Mean drop diameters with ΔP_{Pilot} variation for C-5 at $\frac{\Delta P}{P} = 3$ %, $T_{Fuel} = 120\ ^\circ F$, $T_{Airbox} = 250\ ^\circ F$

| ΔP_{Pilot}	r [mm]	D_{10} [µm]	D_{32} [µm]	MMD[µm]
	-30	12	26	30
	-25	13	29	33
	-20	12	32	38
25 psi	-15	10	32	40
	-10	8	25	34
	-5	8	20	24
	0	8	19	22
	-30	13	27	31
	-20	13	30	35
75 psi	-10	9	25	35
	0	8	18	21

4.3.2 Probability Density Function

The number probability density functions for the mean drop size and axial velocity are compared for each fuel with the fuel injection pressure variations as shown in Fig.4.5. The probability density is on the y-axis, and the drop diameter range is on the x-axis. The binsize of the probability density function is 120 with 1 µm bin width. The drop diameter range is truncated to 50µm for a closer look.

The fuel injection pressure has a minimal effect on the mean drop size and axial velocity, and this trend is shown in the number probability density functions. The velocity distributions for each fuel are overlapped with each other for different fuel injection pressures. The drop distributions for each fuel have relatively the same

profiles. However, the distribution for A-2 at $\Delta P_{Pilot} = 75$ psid is shifted to the larger drop diameter range. The differences in mean drop sizes at r= -10 mm for each injection pressure can be found in Table 4.2. The differences, however, are within the uncertainties. Figure 4.6 shows the volume probability. The volume probability density functions show that the distributions for three injection pressures are similar to each other.
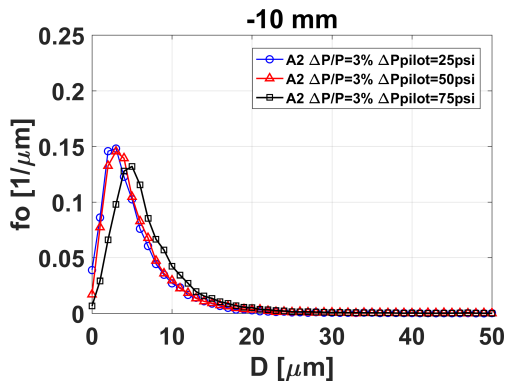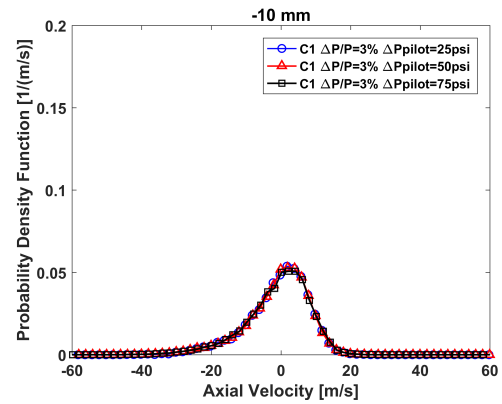
(a) Comparison of D_{32} number probaility density functions for A-2 with ΔP_{Pilot} variation at r= -10 mm.
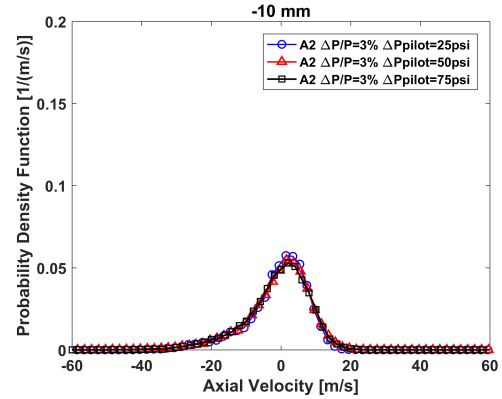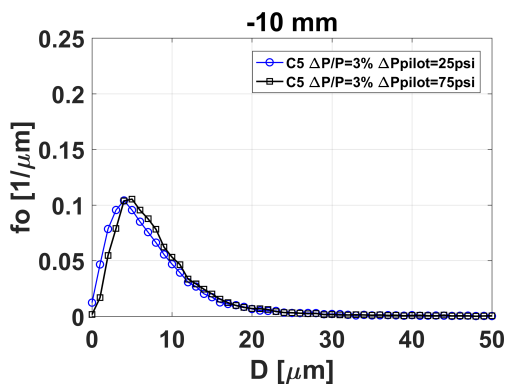
(b) Comparison of axial velocity number probaility density functions for A-2 with ΔP_{Pilot} variation at r= -10 mm.
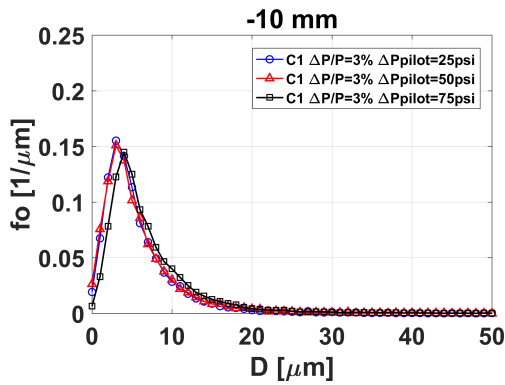
(c) Comparison of D_{32} number probaility density functions for C-1 with ΔP_{Pilot} variation at r= -10 mm.

(d) Comparison of axial velocity number probaility density functions for C-1 with ΔP_{Pilot} variation at r= -10 mm.

(e) Comparison of D_{32} number probaility density functions for C-5 with ΔP_{Pilot} variation at r= -10 mm.

(f) Comparison of axial velocity number probaility density functions for C-5 with ΔP_{Pilot} variation at r= -10 mm.
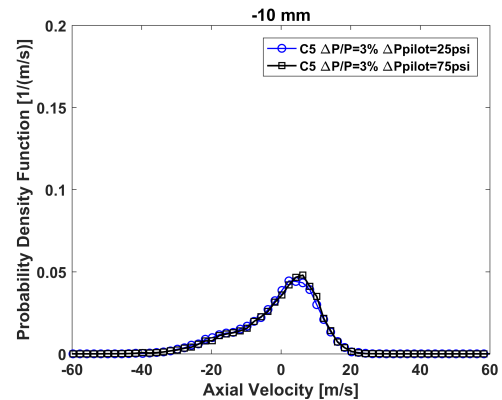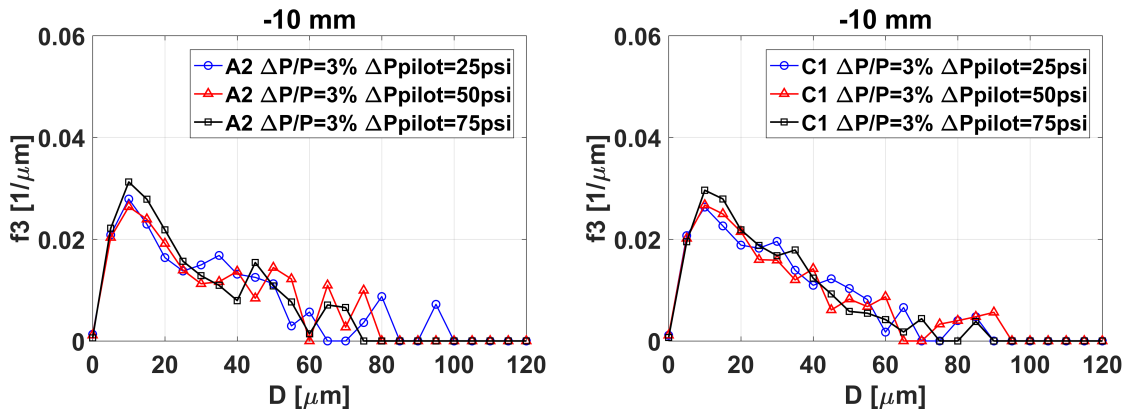
Fig. 4.5.: Comparisons of D_{32} and Axial velocity number PDFs for A-2, C-1, and C-5 with ΔP_{Pilot} variation at $\frac{\Delta P}{P} = 3$ %, $T_{Fuel} = 120$ °F, $T_{Airbox} = 250$ °F

(a) Comparison of D_{32} volume probaility density functions for A-2 with ΔP_{Pilot} variation at r= -10 mm.

(b) Comparison of D_{32} volume probaility density functions for C-1 with ΔP_{Pilot} variation at r= -10 mm.

Fig. 4.6.: Comparisons of D_{32} volume PDFs for A-2 and C-1 with ΔP_{Pilot} variation at $\frac{\Delta P}{P} = 3$ %, $T_{Fuel} = 120$ °F, $T_{Airbox} = 250$ °F

The measurements at r= -20mm show that there are droplets which are traveling downwards and droplets which are traveling upwards. This can be found in the number probability density function for the axial velocities, but it does not contain the drop size information. The joint probability density function can show the inner-dependence between the drop sizes and axial velocities of each drop. Figure 4.7 shows the 2D contour plots for the joint probability density functions of drop size and axial velocity for C-1. The x-axis and y-axis are the drop size and axial velocity respectively. Each color indicates the different values of probability density.

The shape of the profile is maintained with the change in injection pressure. The peak of the contour is lying on the same axial velocity and drop size range for each injection pressure. All the contours at r= 0 mm, for example, are lying on the axial

velocity range of 30 m/s to 0 m/s and on the drop size range of 0 µm to 15 µm for each different injection pressure.
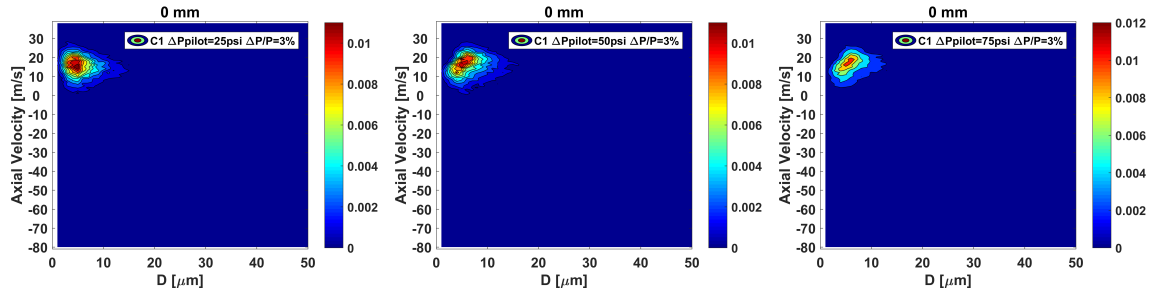
(a) D_{32} and axial velocity joint PDF for C-1 with $\Delta P_{Pilot} = 25$ psi at r= 0 mm.
(b) D_{32} and axial velocity joint PDF for C-1 with $\Delta P_{Pilot} = 50$ psi at r= 0 mm.
(c) D_{32} and axial velocity joint PDF for C-1 with $\Delta P_{Pilot} = 75$ psi at r= 0 mm.
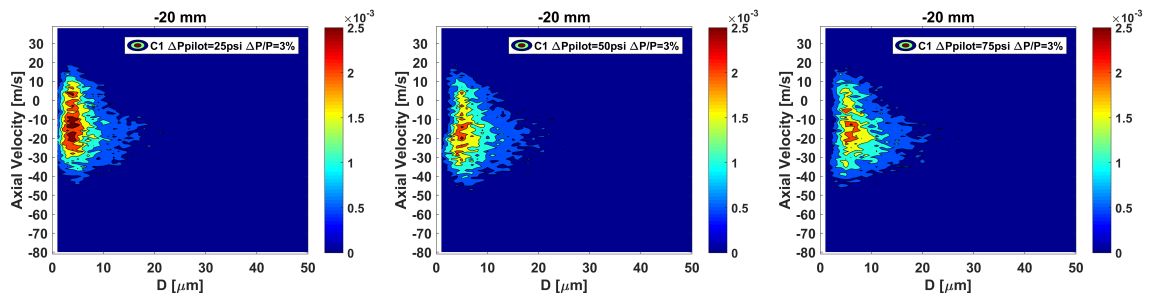
(d) D_{32} and axial velocity joint PDF for C-1 with $\Delta P_{Pilot} = 25$ psi at r= -20 mm.
(e) D_{32} and axial velocity joint PDF for C-1 with $\Delta P_{Pilot} = 50$ psi at r= -20 mm.
(f) D_{32} and axial velocity joint PDF for C-1 with $\Delta P_{Pilot} = 75$ psi at r= -20 mm.

(g) D_{32} and axial velocity joint PDF for C-1 with $\Delta P_{Pilot} = 25$ psi at r= -30 mm.
(h) D_{32} and axial velocity joint PDF for C-1 with $\Delta P_{Pilot} = 50$ psi at r= -30 mm.
(i) D_{32} and axial velocity joint PDF for C-1 with $\Delta P_{Pilot} = 75$ psi at r= -30 mm.

Fig. 4.7.: **Comparisons of joint PDF for C-1 with ΔP_{Pilot} variation at $\frac{\Delta P}{P}$ = 3 %, T_{Fuel} = 120 $^\circ F$, T_{Airbox} = 250 $^\circ F$**
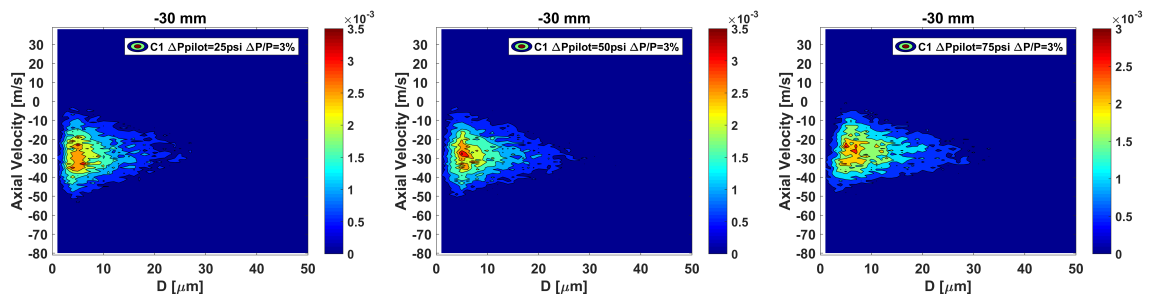
4.3.3 Spray Cone Angle

The effect of the fuel injection pressure on the full spray cone angles are investigated using a shadowgraph imaging with high speed camera. The full cone angles at 0.5 inch downstream from the swirler exit are measured for this study. The fuel injection pressure was varied with 25 psi, 50 psi, and 75 psi at $\frac{\Delta P}{P} = 2$ %. Figure 4.8 shows the comparison of the full cone angles for A-2, C-1, and C-5. The change in the fuel injection pressure is observed to have a minimal effect on the spray cone angles for each fuel. The cone angles are varied within $\pm 1°$ for different fuel injection pressures. These variations are within the margin of experimental uncertainties.

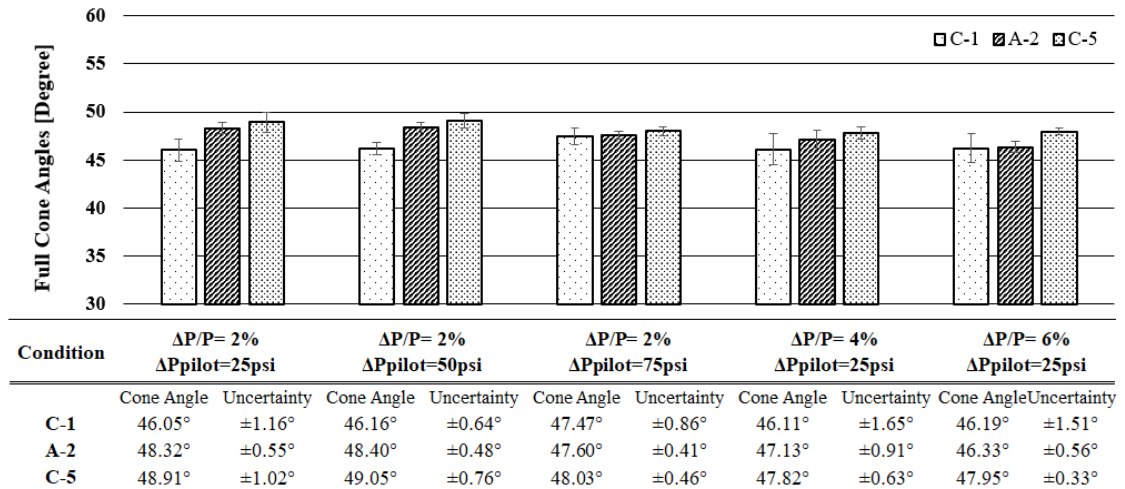| Condition	ΔP/P= 2% ΔPpilot=25psi		ΔP/P= 2% ΔPpilot=50psi		ΔP/P= 2% ΔPpilot=75psi		ΔP/P= 4% ΔPpilot=25psi		ΔP/P= 6% ΔPpilot=25psi	
	Cone Angle	Uncertainty	Cone Angle	Uncertainty	Cone Angle	Uncertainty	Cone Angle	Uncertainty	Cone Angle	Uncertainty
C-1	46.05°	±1.16°	46.16°	±0.64°	47.47°	±0.86°	46.11°	±1.65°	46.19°	±1.51°
A-2	48.32°	±0.55°	48.40°	±0.48°	47.60°	±0.41°	47.13°	±0.91°	46.33°	±0.56°
C-5	48.91°	±1.02°	49.05°	±0.76°	48.03°	±0.46°	47.82°	±0.63°	47.95°	±0.33°

Fig. 4.8.: Comparison of the full cone angles for A-2, C-1, and C-5 with ΔP_{Pilot} **variation and** $\frac{\Delta P}{P}$ **variations at** $T_{Fuel} = 120\ °F$, $T_{Airbox} = 250\ °F$

4.4 Influence of Pressure Drop across the swirler on Spray Characteristics

4.4.1 Drop Size and Velocity

Varing the pressure drop across the swirler is essentially changing the atomizing N_2 flow velocity and mass flow rate within the airbox. The pressure drop was investigated at 2 %, 3 %, and 4 %. Figure 4.9 and 4.10 show the effect of the pressure drop on the mean drop size and axial velocity. The higher pressure drops produce higher axial drop velocities. The momentum of the gas flow applied to the fuel drops increases with increases in pressure drop across the swirler. This causes the drops to travel at higher velocities. However, the axial velocity at the radial location of -15 mm shows no change for three different pressure drops. In addition, the axial velocities are positive within the radial location of -10 mm. This indicates that drops with positive velocities are traveling towards the injector nozzle face instead of away from it. It was also confirmed with the high speed camera investigation. From this, it can be argued that the recirculation is occurring at radial location less than -15 mm. Furthermore, the counterbalance of the momentum of the gas flow from the recirculation zone and beyond the recirculation zone creates a shear layer near the -15 mm radial location.

An increased gas flow velocity in the airbox due to a higher pressure drop decreases the mean drop size. The gas flow with higher velocity carries a higher kinetic energy that can be applied to the drops. The higher kinetic energy on the drops causes the growth of instability in the drop formation. This promotes the ligaments or drops to break up if instability dominate over the restorative energy in the drops.

D_{10}, D_{32}, and MMD are tabulated for all six fuels and shown in Table 4.5 $\sim$ 4.9. The amount changes in D_{32} when the pressure drop increases from 2% to 3% are approximately 7 µm and 11 µm for 2% to 4%. These changes are consistent with all six fuels. The changes in D_{10} and MMD with the pressure drop variation are also significant and follow the same trend as the changes in D_{32}.
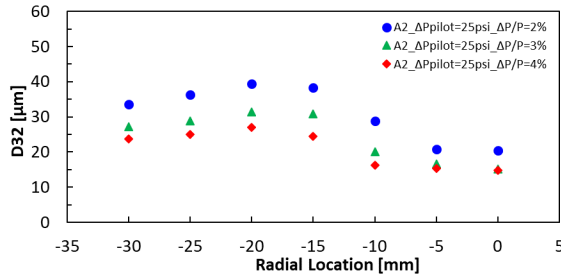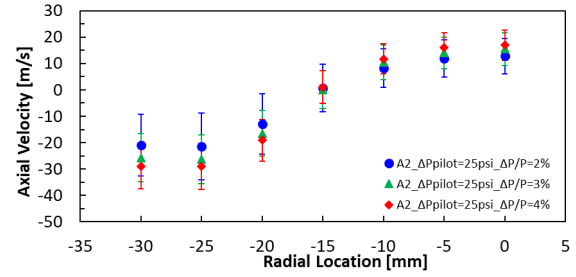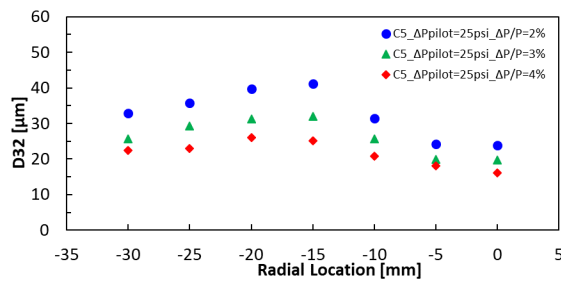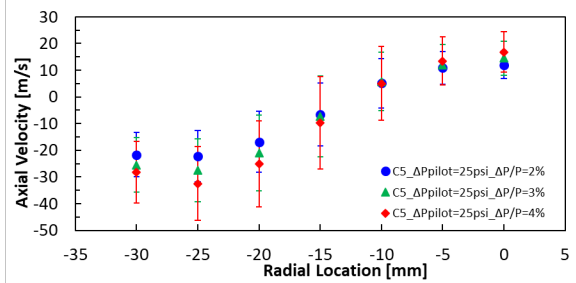
(a) Mean drop size with $\frac{\Delta P}{P}$ variation for A-2.

(b) Axial velocity with $\frac{\Delta P}{P}$ variation for A-2.

(c) Mean drop size with $\frac{\Delta P}{P}$ variation for C-5.

(d) Axial velocity with $\frac{\Delta P}{P}$ variation for C-5.

(e) Mean drop size with $\frac{\Delta P}{P}$ variation for C-1.

(f) Axial velocity with $\frac{\Delta P}{P}$ variation for C-1.

Fig. 4.9.: D_{32} and Axial velocity with $\frac{\Delta P}{P}$ variation for A-2, C-1, and C-5 at $\Delta P_{Pilot} = 25$ psi, $T_{Fuel} = 120\,^{\circ}F$, $T_{Airbox} = 250\,^{\circ}F$
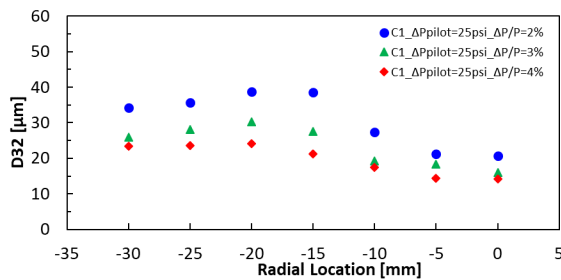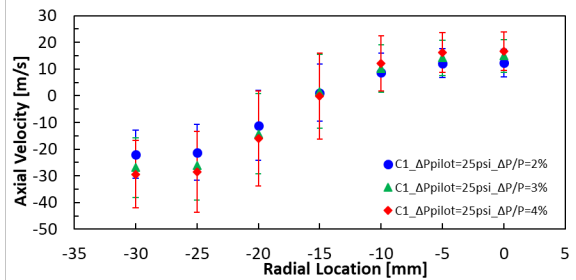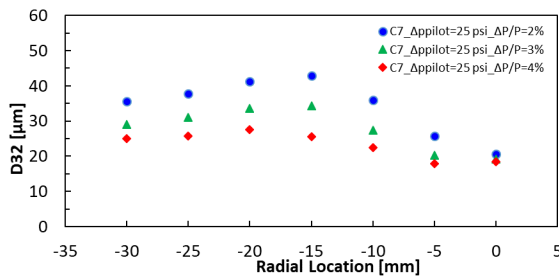
(a) Mean drop size with $\frac{\Delta P}{P}$ variation for C-7.
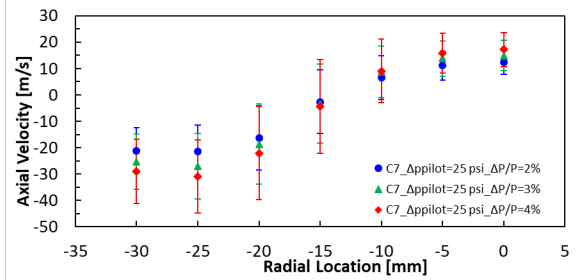
(b) Axial velocity with $\frac{\Delta P}{P}$ variation for C-7.

(c) Mean drop size with $\frac{\Delta P}{P}$ variation for C-8.
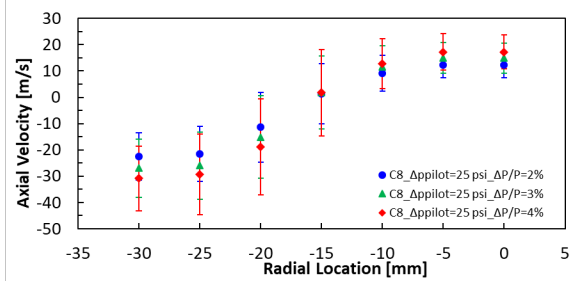
(d) Axial velocity with $\frac{\Delta P}{P}$ variation for C-8.
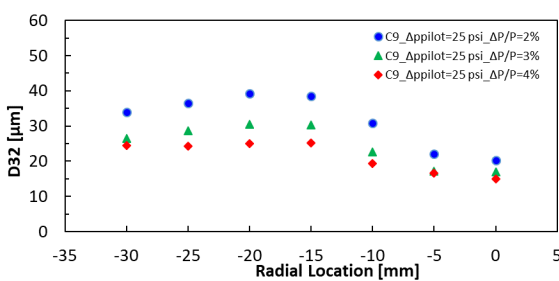
(e) Mean drop size with $\frac{\Delta P}{P}$ variation for C-9.
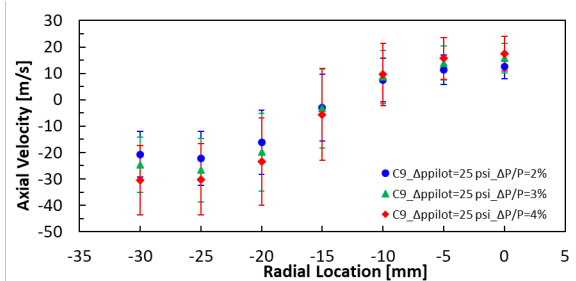
(f) Axial velocity with $\frac{\Delta P}{P}$ variation for C-9.

Fig. 4.10.: D_{32} **and Axial velocity with** $\frac{\Delta P}{P}$ **variation for C-7, C-8, and C-9 at** $\Delta P_{Pilot} = 25$ **psi,** $T_{Fuel} = 120$ $^{\circ}F$, $T_{Airbox} = 250$ $^{\circ}F$

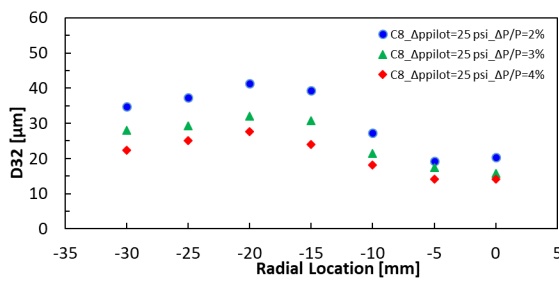Table 4.5.: Mean drop diameters with $\frac{\Delta P}{P}$ variation for A-2 at $\Delta P_{Pilot} =$ 25 psi, $T_{Fuel} = $ 120 °F, $T_{Airbox} = $ 250 °F

$\frac{\Delta P}{P}$	r [mm]	D_{10} [µm]	D_{32} [µm]	MMD[µm]
2 %	-30	12	34	41
	-25	13	36	43
	-20	12	40	49
	-15	9	39	53
	-10	7	30	47
	-5	7	21	28
	0	7	20	27
3 %	-30	11	27	33
	-25	12	30	34
	-20	12	30	36
	-15	10	32	42
	-10	8	24	36
	-5	8	20	24
	0	8	20	24
4 %	-30	8	24	28
	-25	9	25	30
	-20	8	28	33
	-15	6	26	37
	-10	6	16	20
	-5	6	15	18
	0	6	15	17

Table 4.6.: Mean drop diameters with $\frac{\Delta P}{P}$ variation for C-5 at $\Delta P_{Pilot} = 25$ psi, $T_{Fuel} = 120\ °F$, $T_{Airbox} = 250\ °F$

$\frac{\Delta P}{P}$	r [mm]	D_{10} [µm]	D_{32} [µm]	MMD[µm]
	-30	14	33	39
	-25	16	37	42
	-20	16	40	48
2 %	-15	14	42	53
	-10	10	32	45
	-5	8	24	31
	0	8	24	30
	-30	12	26	30
	-25	13	29	33
	-20	12	32	38
3 %	-15	10	32	40
	-10	8	25	34
	-5	8	20	24
	0	8	19	22
	-30	11	23	26
	-25	11	24	27
	-20	11	27	31
4 %	-15	10	26	32
	-10	9	21	26
	-5	8	18	21
	0	7	16	18

Table 4.7.: Mean drop diameters with $\frac{\Delta P}{P}$ variation for C-7 at $\Delta P_{Pilot} = $ 25 psi, $T_{Fuel} = 120\ °F$, $T_{Airbox} = 250\ °F$

$\frac{\Delta P}{P}$	r [mm]	D_{10} [µm]	D_{32} [µm]	MMD[µm]
2 %	-30	13	36	44
	-25	15	38	46
	-20	14	42	51
	-15	12	44	57
	-10	10	37	53
	-5	9	26	39
	0	8	21	26
3 %	-30	11	29	35
	-25	12	31	37
	-20	12	34	41
	-15	10	34	46
	-10	8	28	46
	-5	8	20	27
	0	8	19	24
4 %	-30	10	25	30
	-25	11	26	30
	-20	10	28	33
	-15	9	26	35
	-10	8	22	35
	-5	7	18	21
	0	7	18	23

Table 4.8.: Mean drop diameters with $\frac{\Delta P}{P}$ variation for C-8 at $\Delta P_{Pilot} =$ 25 psi, $T_{Fuel} = 120\ °F$, $T_{Airbox} = 250\ °F$

$\frac{\Delta P}{P}$	r [mm]	D_{10} [µm]	D_{32} [µm]	MMD[µm]
2 %	-30	13	35	42
	-25	15	38	46
	-20	14	42	52
	-15	10	40	55
	-10	9	28	45
	-5	9	19	23
	0	8	20	24
3 %	-30	12	28	34
	-25	12	30	35
	-20	11	32	40
	-15	9	31	44
	-10	7	21	32
	-5	7	17	21
	0	7	16	18
4 %	-30	10	23	26
	-25	10	26	30
	-20	10	28	35
	-15	8	24	33
	-10	7	18	24
	-5	7	14	15
	0	7	14	15

Table 4.9.: Mean drop diameters with $\frac{\Delta P}{P}$ variation for C-9 at $\Delta P_{Pilot} =$ 25 psi, $T_{Fuel} = 120\ °F$, $T_{Airbox} = 250\ °F$

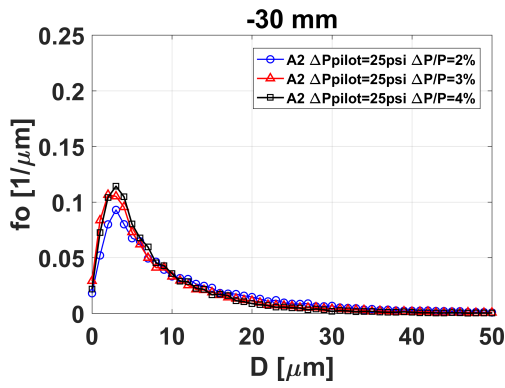| $\frac{\Delta P}{P}$	r [mm]	D_{10} [µm]	D_{32} [µm]	MMD[µm]
	-30	14	34	41
	-25	16	37	44
	-20	15	40	49
2 %	-15	12	39	52
	-10	9	31	49
	-5	9	22	28
	0	9	20	23
	-30	12	26	31
	-25	13	29	34
	-20	13	31	37
3 %	-15	10	30	42
	-10	9	23	32
	-5	8	17	19
	0	8	17	19
	-30	12	24	28
	-25	12	25	28
	-20	11	25	29
4 %	-15	9	25	34
	-10	8	19	25
	-5	8	16	18
	0	8	15	16

4.4.2   Probability Density Function

The impact of the increase in $\frac{\Delta P}{P}$ on the mean drop size and axial velocity is investigated through the number probability density functions. The comparisons of
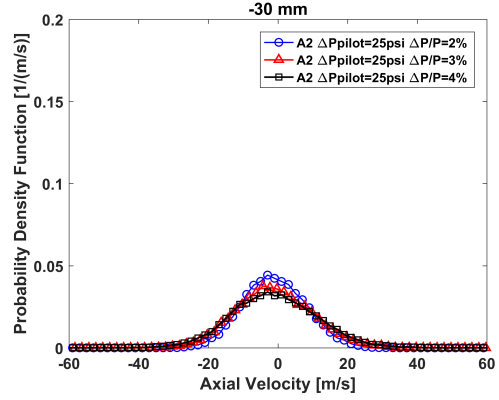
D_{32} and axial velocity number probability density functions are shown in Fig. 4.11 for A-2, C-1, and C-5. C-7, C-8, and C-9 are shown in Fig. 4.12.

An increase in pressure drop on the mean drop size shows an increase in the probability density of small diameters. The peak of the probability density function is observed to increase with the greater pressure drop while the probability density for the larger drops decreases. The same trends are shown in the mean drop size probability density functions for all six fuels, and the trends match well with the mean drop diameter trends.
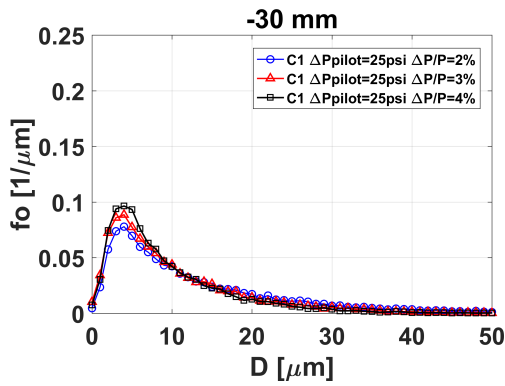
For the axial velocity, an increase in the pressure drop widens the probability density function profile. As a result, the peak of the probability density function is observed to be decreased. This follows well with the axial velocity trends.
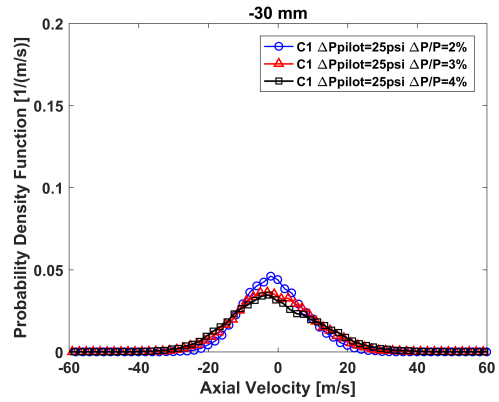
(a) Comparison of D_{32} number probaility density functions for A-2 with $\frac{\Delta P}{P}$ variation at r= -30 mm.
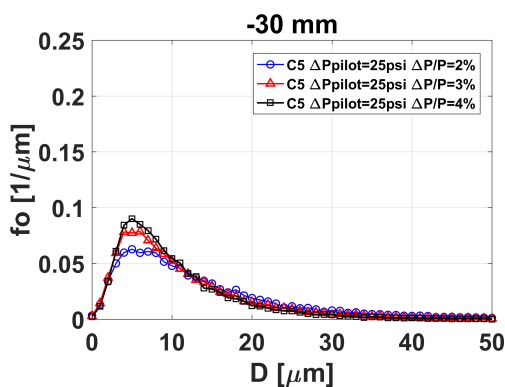
(b) Comparison of axial velocity number probaility density functions for A-2 with $\frac{\Delta P}{P}$ variation at r= -30 mm.

(c) Comparison of D_{32} number probaility density functions for C-1 with $\frac{\Delta P}{P}$ variation at r= -30 mm.

(d) Comparison of axial velocity number probaility density functions for C-1 with $\frac{\Delta P}{P}$ variation at r= -30 mm.

(e) Comparison of D_{32} number probaility density functions for C-5 with $\frac{\Delta P}{P}$ variation at r= -30 mm.

(f) Comparison of axial velocity number probaility density functions for C-5 with $\frac{\Delta P}{P}$ variation at r= -30 mm.

Fig. 4.11.: **Comparison of D_{32} and Axial velocity number PDFs with $\frac{\Delta P}{P}$ variation for A-2, C-1, and C-5 at $\Delta P_{Pilot} = 25$ psi, $T_{Fuel} = 120\ ^{\circ}F$, $T_{Airbox} = 250\ ^{\circ}F$**
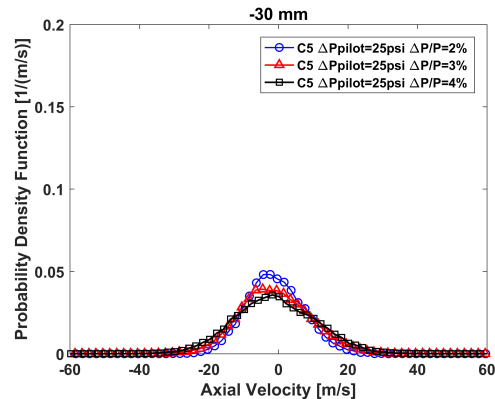
(a) Comparison of D_{32} number probaility density functions for C-7 with $\frac{\Delta P}{P}$ variation at r= -30 mm.

(b) Comparison of axial velocity number probaility density functions for C-7 with $\frac{\Delta P}{P}$ variation at r= -30 mm.

(c) Comparison of D_{32} number probaility density functions for C-8 with $\frac{\Delta P}{P}$ variation at r= -30 mm.

(d) Comparison of axial velocity number probaility density functions for C-8 with $\frac{\Delta P}{P}$ variation at r= -30 mm.
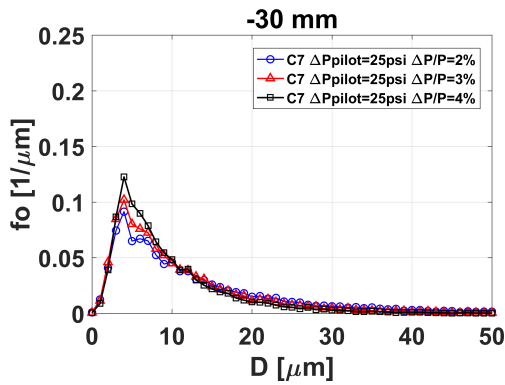
(e) Comparison of D_{32} number probaility density functions for C-9 with $\frac{\Delta P}{P}$ variation at r= -30 mm.
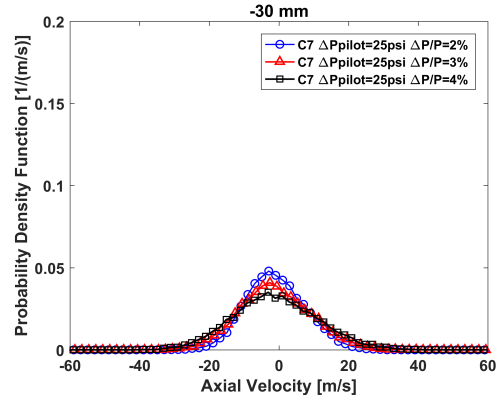
(f) Comparison of axial velocity number probaility density functions for C-9 with $\frac{\Delta P}{P}$ variation at r= -30 mm.
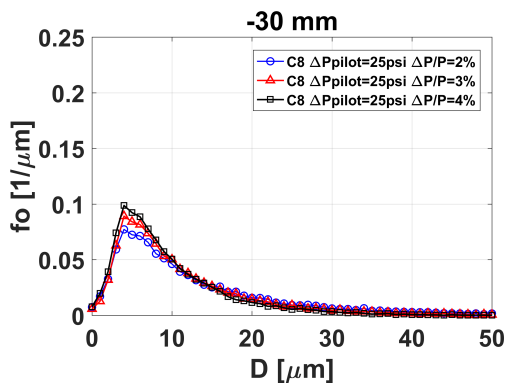
Fig. 4.12.: Comparison of D_{32} and Axial velocity number PDFs with $\frac{\Delta P}{P}$ variation for C-7, C-8, and C-9 at $\Delta P_{Pilot} = 25$ psi, $T_{Fuel} = 120\ °F$, $T_{Airbox} = 250\ °F$
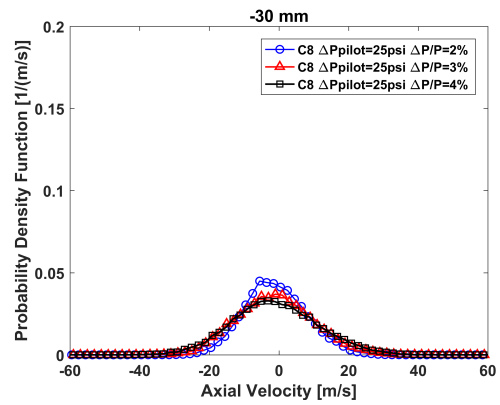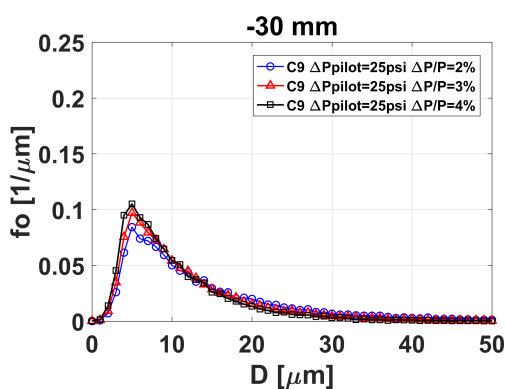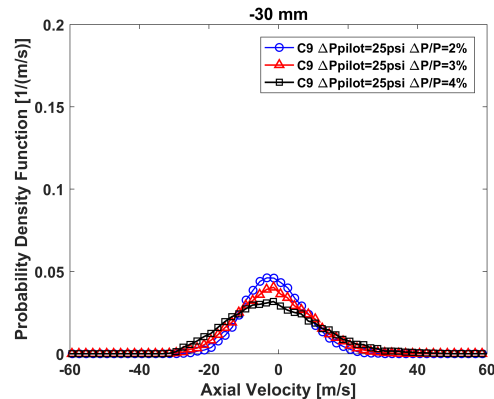
The effect of the pressure drop on the mean drop size and velocity are also investigated through the joint probability density functions as shown in Figure 4.13 and 4.14. For A-2, C-1, and C-5, the joint probability density functions at r= -30 mm are presented. The joint probability density functions for C-7, C-8, and C-9 are presented at r= -20 mm.

An increase in pressure drop decreases the mean drop size and increases the axial velocity. These trends are also shown in the joint probability density functions. The profile of the contour gets wider along y-axis and narrower along x-axis as the pressure drop increases. In other words, the probability density of larger drop diameters gets smaller while the velocity span gets wider in the negative direction as the drop velocity increases. The peak of the contour for each fuel is also shifted to the negative direction of y-axis as the pressure drop increases. This change appears prominently with the increase in pressure drop from 2% to 4%.
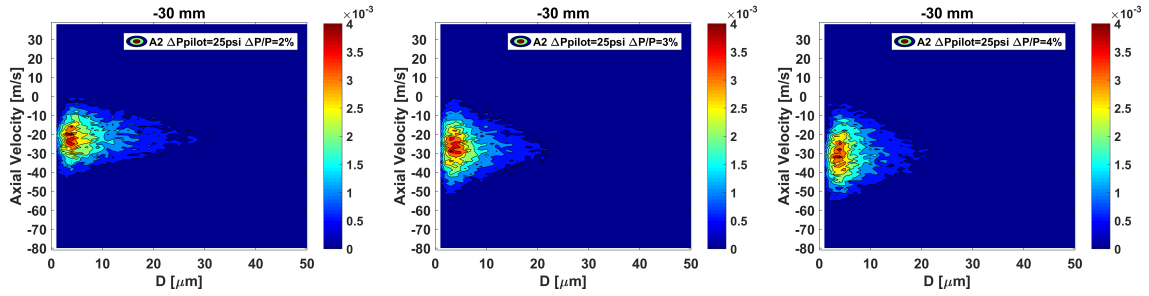
(a) D_{32} and axial velocity joint PDF for A-2 with $\frac{\Delta P}{P} = 2$ % at r= -30 mm.

(b) D_{32} and axial velocity joint PDF for A-2 with $\frac{\Delta P}{P} = 3$ % at r= -30 mm.

(c) D_{32} and axial velocity joint PDF for A-2 with $\frac{\Delta P}{P} = 4$ % at r= -30 mm.
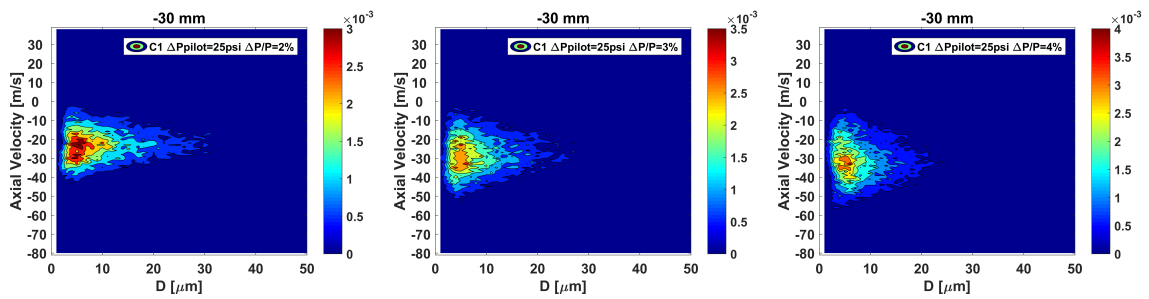
(d) D_{32} and axial velocity joint PDF for C-1 with $\frac{\Delta P}{P} = 2$ % at r= -30 mm.

(e) D_{32} and axial velocity joint PDF for C-1 with $\frac{\Delta P}{P} = 3$ % at r= -30 mm.

(f) D_{32} and axial velocity joint PDF for C-1 with $\frac{\Delta P}{P} = 4$ % at r= -30 mm.
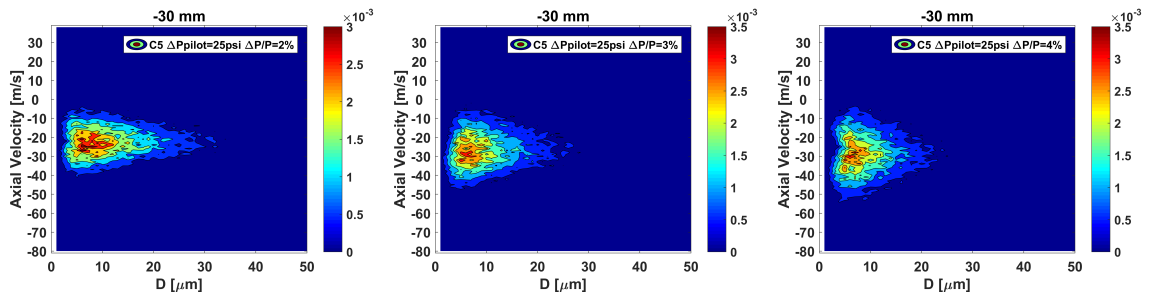
(g) D_{32} and axial velocity joint PDF for C-5 with $\frac{\Delta P}{P} = 2$ % at r= -30 mm.

(h) D_{32} and axial velocity joint PDF for C-5 with $\frac{\Delta P}{P} = 3$ % at r= -30 mm.

(i) D_{32} and axial velocity joint PDF for C-5 with $\frac{\Delta P}{P} = 4$ % at r= -30 mm.

Fig. 4.13.: Comparisons of joint PDF for A-2, C-1, and C-5 with $\frac{\Delta P}{P}$ variation at $\Delta P_{Pilot} = 25$ psi, $T_{Fuel} = 120\ ^{\circ}F$, $T_{Airbox} = 250\ ^{\circ}F$

(a) D_{32} and axial velocity joint PDF for C-7 with $\frac{\Delta P}{P} = 2$ % at r= -20 mm.

(b) D_{32} and axial velocity joint PDF for C-7 with $\frac{\Delta P}{P} = 3$ % at r= -20 mm.

(c) D_{32} and axial velocity joint PDF for C-7 with $\frac{\Delta P}{P} = 4$ % at r= -20 mm.

(d) D_{32} and axial velocity joint PDF for C-8 with $\frac{\Delta P}{P} = 2$ % at r= -20 mm.

(e) D_{32} and axial velocity joint PDF for C-8 with $\frac{\Delta P}{P} = 3$ % at r= -20 mm.

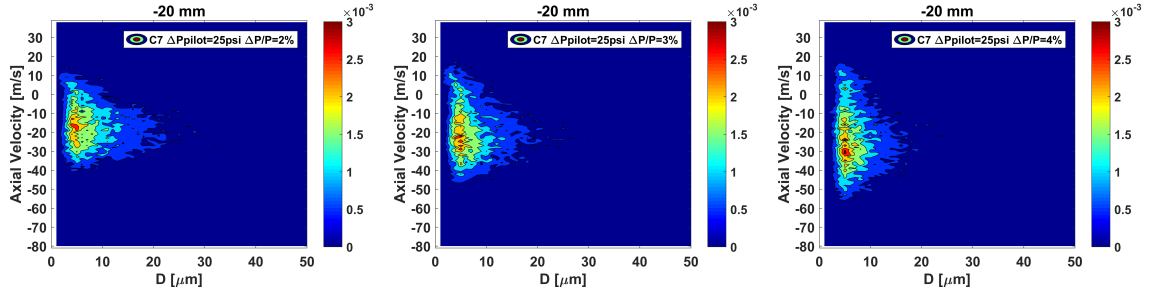(f) D_{32} and axial velocity joint PDF for C-8 with $\frac{\Delta P}{P} = 4$ % at r= -20 mm.

(g) D_{32} and axial velocity joint PDF for C-9 with $\frac{\Delta P}{P} = 2$ % at r= -20 mm.

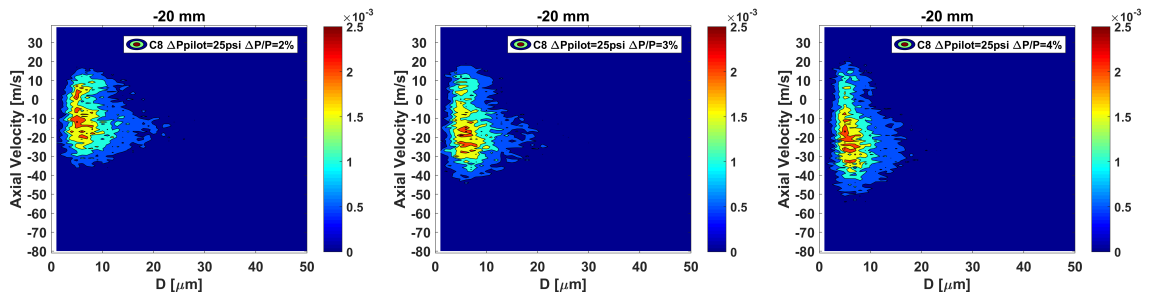(h) D_{32} and axial velocity joint PDF for C-9 with $\frac{\Delta P}{P} = 3$ % at r= -20 mm.

(i) D_{32} and axial velocity joint PDF for C-9 with $\frac{\Delta P}{P} = 4$ % at r= -20 mm.

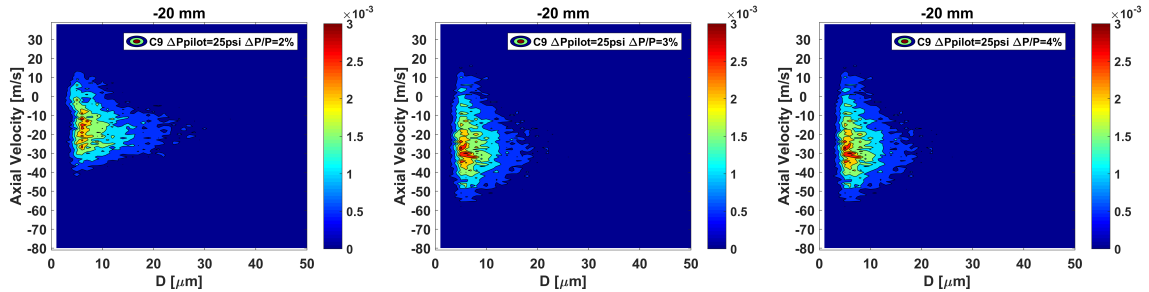**Fig. 4.14.: Comparisons of joint PDF for C-7, C-8, and C-9 with $\frac{\Delta P}{P}$ variation at $\Delta P_{Pilot} = 25$ psi, $T_{Fuel} = 120\ ^\circ F$, $T_{Airbox} = 250\ ^\circ F$**

4.4.3 Spray Cone Angle

The effect of the pressure drop across the siwrler on the full spray cone angles are investigated using a shadowgraph imaging with high speed camera. The pressure drop was varied with 2%, 4%, and 6% at $\Delta P_{Pilot} = 25$ psi. The results from Fig.4.8 show that the pressure drop variation was observed to have a minimal effect on the spray cone angles for each fuel. The changes in cone angles are within $\pm 1°$ for different pressure drops. These variations are within the margin of experimental uncertainties.

4.5 Influence of Fuel Types and Property on Spray Characteristics

4.5.1 Drop Size and Velocity

The effect of the fuel types on the mean drop size and axial velocity was investigated. The types of fuel compared in this section are A-2, C-1, C-5, C-7, C-8, and C-9. Each fuel type has a different chemical composition or ratio of compounds and has different physical properties such as surface tension, density, and viscosity. The physical properties estimated at LBO conditions are tabulated in Table 3.1 for each fuel type.

Figure 4.15 and 4.16 show the comparison of mean drop size and axial velocity at $\frac{\Delta P}{P} = 3$ % and $\Delta P_{Pilot} = 25$ psid for all test fuels. The plots for $\frac{\Delta P}{P} = 2$ and 4 % cases can be found in Appendix D. From the plots, it is observed that the C-7 fuel formed the largest drop sizes consistently at all radial locations. This trend is also shown in the cases where $\frac{\Delta P}{P} = 2$ and 4 %. For the axial velocity, the C-5 fuel droplets

are traveling faster than any other fuel droplets, especially within the radial location range of -20 mm to -5 mm. The axial velocities of all six fuel droplets increased with an increase in the pressure drop across the swirler.

From Table 3.1, the A-2 fuel has the highest viscosity value and C8 has the lowest. C-7 and C-8 fuels have the highest surface tension, and C-1 has the lowest surface tension. However, the difference in surface tension between C-7 and C-1 fuels is 0.004 N/m. C-8 fuel has the highest density and C1 and C9 are the lowest.

From these observations, the relationship between each fuel property and the mean drop size and axial velocity could not be found. An additional measurement is necessary with varying only surface tension while other properties are kept constant or vice versa in order to provide a clear explanation on the effect of each fuel property on drop size and axial velocity at LBO conditions.
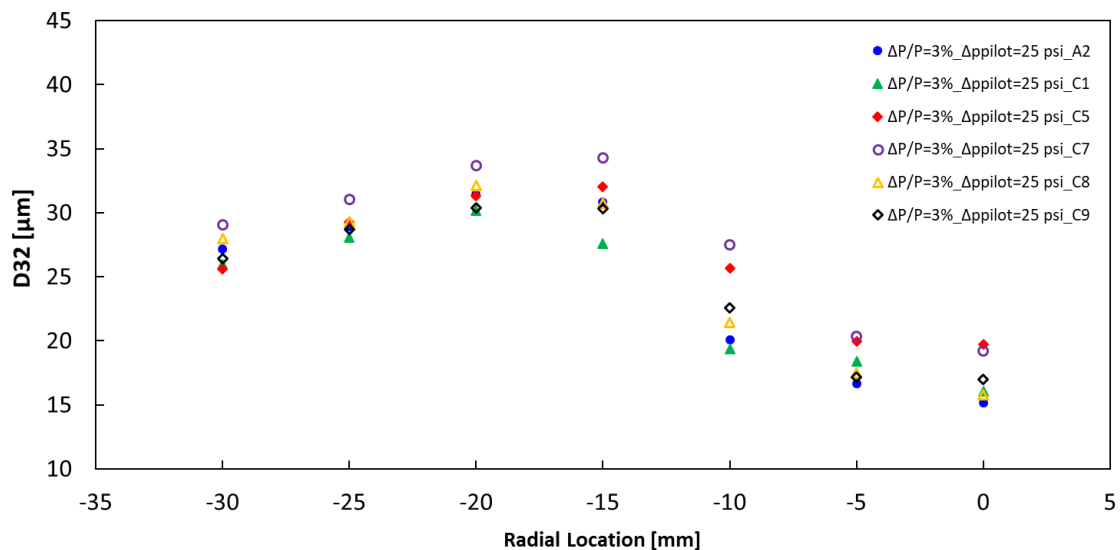
Fig. 4.15.: Comparison of Mean drop size for all six fuels at $\frac{\Delta P}{P} = 3$ %, $\Delta P_{Pilot} = 25$ **psi**, $T_{Fuel} = 120$ °F, $T_{Airbox} = 250$ °F
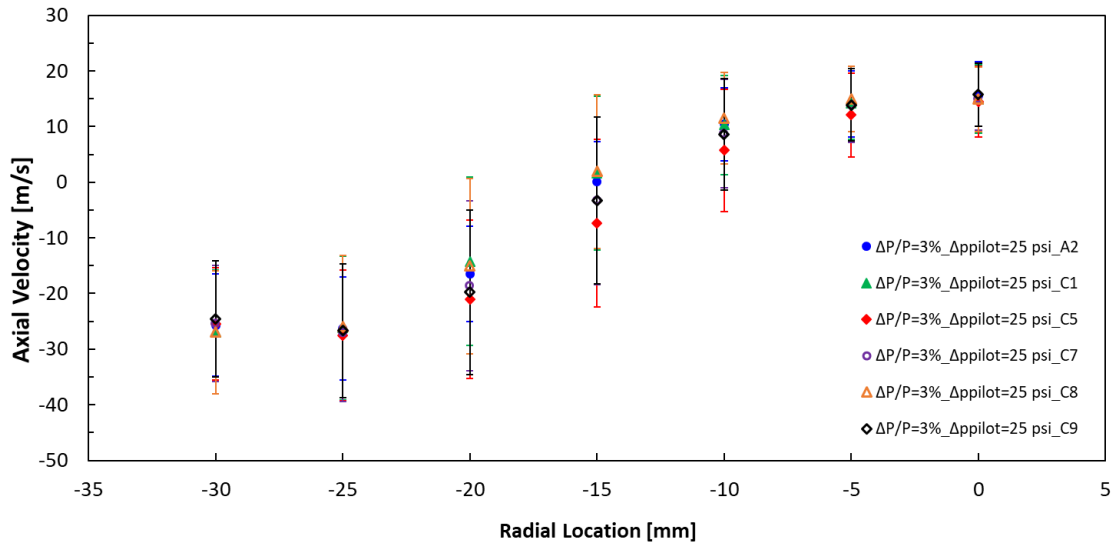
Fig. 4.16.: Comparison of Axial Velocity for all six fuels at $\frac{\Delta P}{P} = 3$ %, $\Delta P_{Pilot} = 25$ psi, $T_{Fuel} = 120$ °F, $T_{Airbox} = 250$ °F

4.5.2 Probability Density Function

The effect of fuel properties on the mean drop size and axial velocity is investigated with the joint probability density functions as shown in Fig. 4.17 and 4.18. Each fuel is compared at the same radial locations of -10 mm and -30 mm. At both radial locations, the shape of the contour profile maintained a similarity for each fuel. Little variations on the axial velocity and drop diameter can be shown as a slight different shape of the contour for each fuel. These trends follow the observations regarding mean drop size and axial velocity.
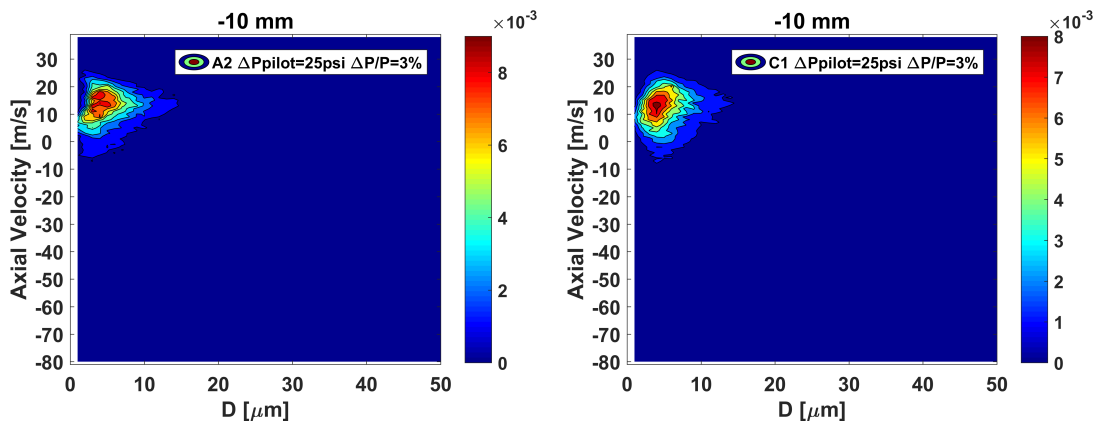
(a) D_{32} and axial velocity joint PDF for A-2 at r= -10 mm.

(b) D_{32} and axial velocity joint PDF for C-1 at r= -10 mm.
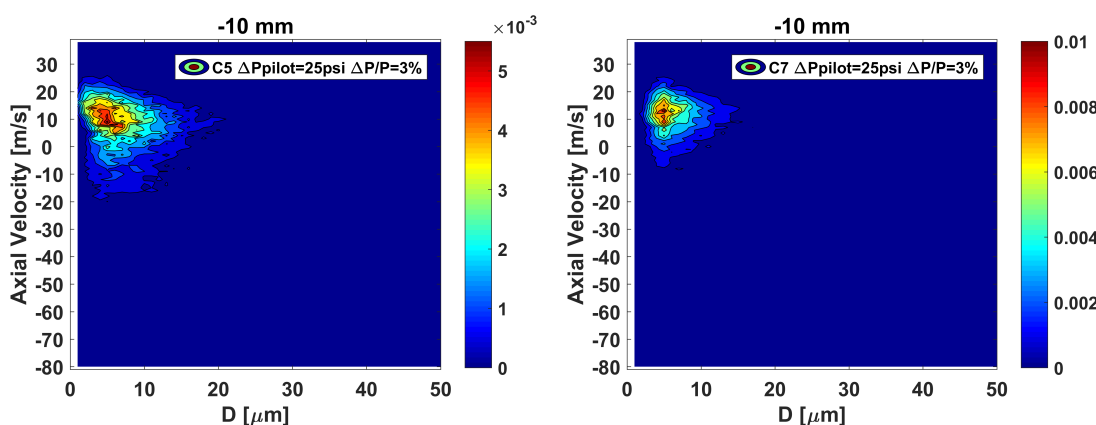
(c) D_{32} and axial velocity joint PDF for C-5 at r= -10 mm.

(d) D_{32} and axial velocity joint PDF for C-7 at r= -10 mm.
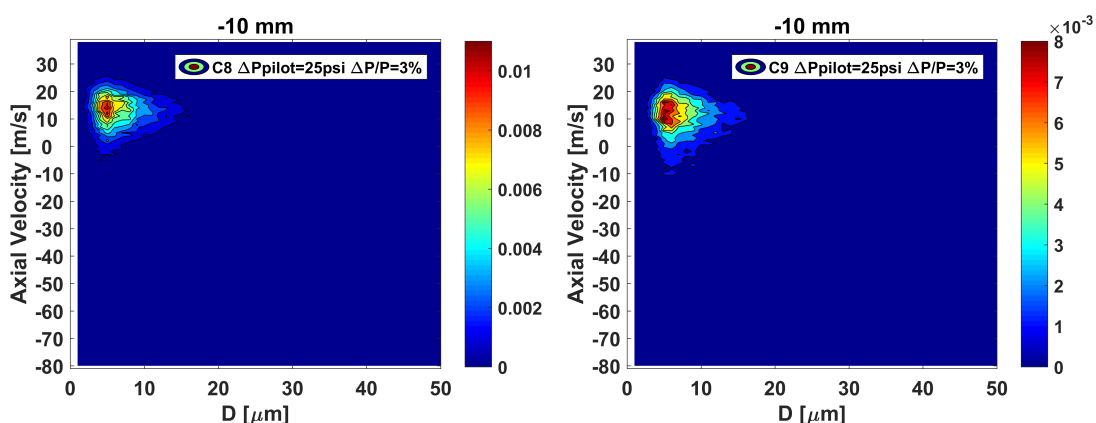
(e) D_{32} and axial velocity joint PDF for C-8 at r= -10 mm.

(f) D_{32} and axial velocity joint PDF for C-9 at r= -10 mm.

Fig. 4.17.: Comparisons of joint PDF for A-2, C-1, C-5, C-7, C-8, and C-9 at r= -10 mm with $\frac{\Delta P}{P} = 3$ %, $\Delta P_{Pilot} = 25$ psi, $T_{Fuel} = 120$ °F, $T_{Airbox} = 250$ °F at 1 inch measurement plane
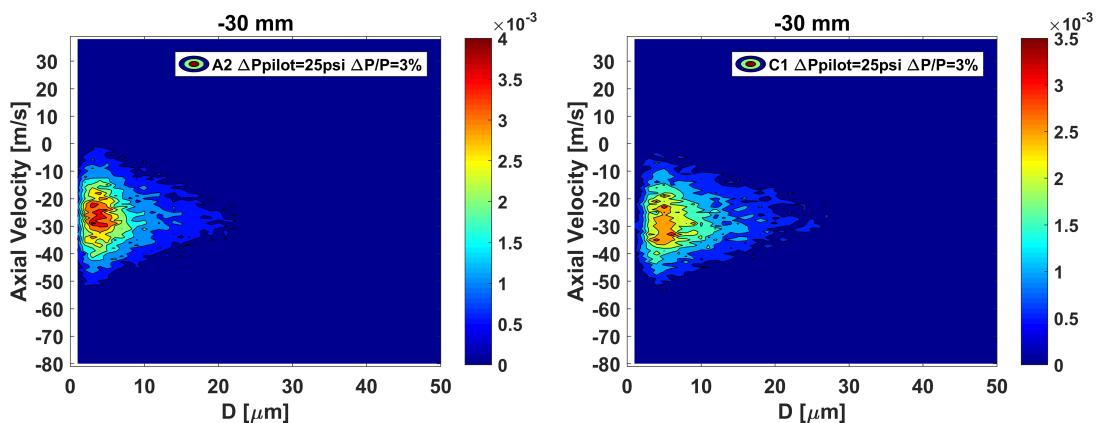
(a) D_{32} and axial velocity joint PDF for A-2 at r= -30 mm.

(b) D_{32} and axial velocity joint PDF for C-1 at r= -30 mm.
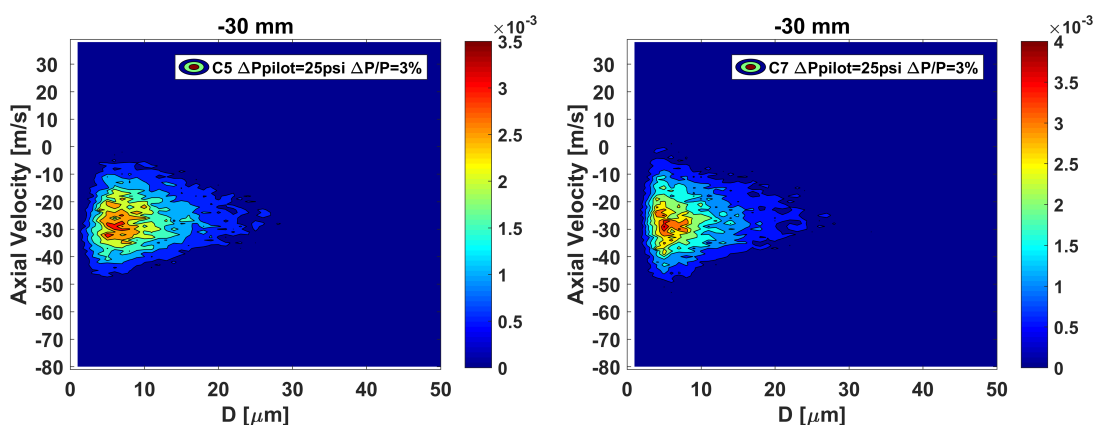
(c) D_{32} and axial velocity joint PDF for C-5 at r= -30 mm.

(d) D_{32} and axial velocity joint PDF for C-7 at r= -30 mm.
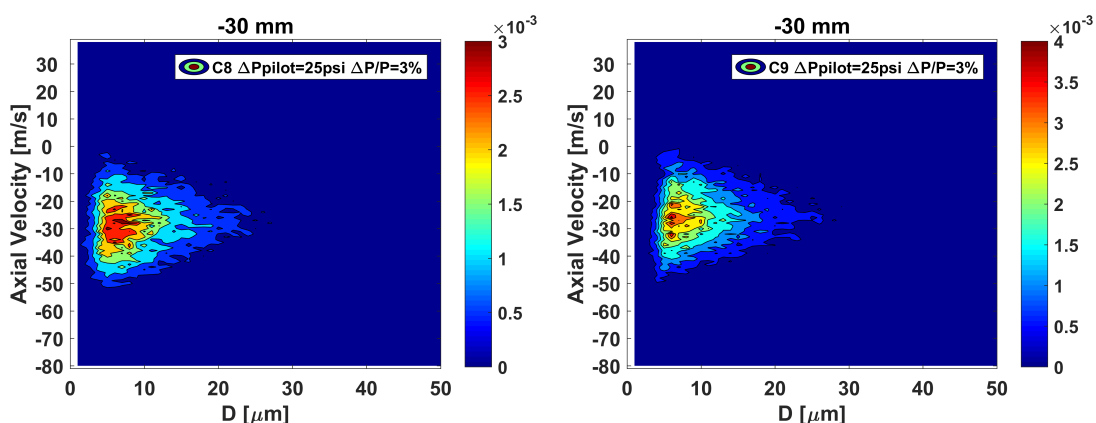
(e) D_{32} and axial velocity joint PDF for C-8 at r= -30 mm.

(f) D_{32} and axial velocity joint PDF for C-9 at r= -30 mm.

Fig. 4.18.: Comparisons of joint PDF for A-2, C-1, C-5, C-7, C-8, and C-9 at r= -30 mm with $\frac{\Delta P}{P} = 3$ %, $\Delta P_{Pilot} = 25$ psi, $T_{Fuel} = 120$ °F, $T_{Airbox} = 250$ °F at 1 inch measurement plane

4.5.3   Spray Cone Angle

The effect of fuel type on the full spray cone angles is investigated. The results from Fig.4.8 show that fuel type has a light effect on full cone angle with C-5 having higher angles compared to those for other two fuels. For first two cases in Fig.4.8, the uncertainties for C-1 and C-5 do not overlap each other. The differences in cone angles for those fuels are within 2°. Other three cases show that the variations in cone angles for each fuel are within the margin of experimental uncertainties.

5. SUMMARY AND CONCLUSION

5.1   Introduction

The abundant works on characterizing the spray with different types of the pressure-swirl and air-blast atomizers have been done with various fuel types for the combustion applications. However, the experimental studies on the spray characteristics of the hybrid air-blast pressure-swirl atomizer at actual aircraft combustion conditions are currently lacking, especially with the alternative aviation fuels.

In this work, a PDA system used to obtain the drop size and axial velocity of the spray from the hybrid air-blast pressure-swirl atomizer at lean blowout conditions. Five different alternative aviation fuels and one reference fuel were tested and studied for their spray characteristics at 1 inch (25.4mm) downstream from the swirler exit.

Three major operating parameters were varied in this study: the pressure drop across the swirler, fuel types, and fuel injection pressure. The effects of each parameter on the spray characteristics such as mean drop size, drop velocity, and cone angle were studied. The joint probability density function for the drop diameters and drop velocity were generated to investigate the inner-dependence of drop diameters and drop velocity. The Weber number and Ohnesorge number were used to determine the break-up regime for the drops at 1 inch (25.4 mm) measurement plane.

5.2   Summary Key Results

1. The effect of the fuel injection pressure on the mean drop size, velocity, and cone angle is observed to be very minimal for each type of fuel. At ambient condition, an increase in fuel injection pressure decreased the mean drop size. Further investigation is necessary to determine which factor caused the different result from LBO and ambient conditions.

2. The pressure drop across the swirler has a significant effect on the mean drop size and velocity, but not on the cone angle. An increase in pressure drop results the decrease in the mean drop size and increase in the axial velocity for all six fuels. The amount of increase in mean drop size with the increase in pressure drop is observed to be consistent for all six fuels. The changes in cone angles with the pressure drop are found to be minimal and within the margin of experimental uncertainties.

3. Different mean drop sizes and velocities are observed for six different fuels. The difference in mean drop size between C-7 (largest) and C-1 (smallest) are the largest with approximately 4.5 μm. The differences in other fuels are observed to be less than 4.5 μm and minimal. It is observed that there is no relationship between the fuel properties and the mean drop sizes and velocities. An additional measurement is needed to show the true effect of each fuel properties on the spray characteristics at LBO conditions.

The cone angles for A-2, C-1, and C-5 are compared. It is observed that the differences in cone angles for all three fuels are not significant and within the margin of experimental uncertainties.

6. FUTURE WORK

Based on the results from this study, the recommended future works include:

- Investigation of spray characteristics at high altitude relight and cold start conditions. The liquid nitrogen can be introduced to the airbox in order to decrease the airbox flow temperature. The ejector needs to be installed at the end of the pressure vessel to create a sub-atmospheric condition for the high altitude relight.

- More sophisticated investigation on the spray impingement on the inner surface of the current hybrid atomizer, because the methanol does not have the same physical properties as the jet fuel. Different type of fluid may have different atomization. If the pilot spray impinges on the inner surface, the different drop break-up mechanism can be expected.

- Detailed investigation of the spray characteristics near the swirler exit nozzle to determine the drop break-up regimes. Due to limitation of PDA on dense spray, alternative measurement technique may be necessary.

- Investigation of the spray characteristics at higher vessel pressure.

- Investigation of the characteristics of spray from main fuel injector.

- Investigation of spray characteristics with different type of injector at LBO conditions.

REFERENCES

REFERENCES

[1] Bachalo, W. D., and M. J. Houser. *Phase/Doppler Spray Analyzer For Simultaneous Measurements Of Drop Size And Velocity Distributions.* Optical Engineering, vol. 23, no.5, Jan 1984

[2] Bachalo, W. D. *Spray diagnostics for the twenty-first century.* Atomization Sprays 10 439-74, 2000

[3] Bohkart, J. A., et al. *Spray Measurements at Elevated Pressure and Temperatures using Phase Doppler Anemometry.* AIAA SciTech Forum, 55th AIAA Aerospace Sciences Meetting, Texas, Jan. 2017

[4] Buschhagen, T. et al. *Effect of Aviation Fuel Type and Fuel Injection Conditions on Non-reacting Spray Characteristics of a Hybrid Airblast Fuel Injector.* 54th AIAA Aerospace Sciences Meeting, 2016

[5] Custer, J.R. et al. *Influence of Design Concept and Liquid Properties on Fuel Injector Performance.* Journal of Propulsion and Power, vol. 4, no. 4, 1988, pp. 378384., doi:10.2514/3.23077.

[6] Colket, M. et al. *An Overview of the National Jet Fuels Combustion Program.* 54th AIAA Aerospace Sciences Meeting, AIAA SciTech Forum, (AIAA 2016-0177)

[7] Chen, S.K., Lefebvre, A. H., Rollbuhler J. *Factors Influencing the Effective Spray Cone Angle of Pressure-Swirl Atomizers.* Journal of Engineering for Gas Turbines and Power, American Society of Mechanical Engineers, 1 Jan. 1992

[8] Durdina, L., et al. *Investigation and Comparison of Spray Characteristics of Pressure-Swirl Atomizers for a Small-Sized Aircraft Turbine Engine.* International Journal of Heat and Mass Transfer, Pergamon, 8 Aug. 2014

[9] Dantec Dynamics *LDA and PDA Reference Manual.* Dantec Dynamics A/S, Denmark, 2011

[10] De Corso, S. M. and Kemeny, G. A. *Effect of Ambient and Fuel Pressure on Nozzle Spray Angle.* ASME Transactions, Vol. 79, No. 3, 1957, pp. 607-615

[11] Dantec Dynamics A/S *FiberFlow Installation and User's guide.* Dantec Dynamics, Denmark, 1995

[12] Durst, F. and ZARE, M. *Laser Doppler measurement in two-phase flows.* Proceedings of the LDA Symposium, pp.403-429. Copenhagen, Denmark, 1975

[13] Fansler, Todd D. *Spray Measurement Technology: a Review.* Measurement Science and Technology, IOP Publishing, 1 Jan. 2015

[14] Feddema, Rick. *Effect of Aviation Fuel Type and Fuel Injection Conditions on the Spray Characteristics of Pressure swirler and Hybrid Airblast Fuel Injectors.* ProQuest LLC, 2014, docs.lib.purdue.edu/open access theses/12/

[15] Guilldenbecher, D. R., et al. *Secondary Atomization.* Experiments in Fluids, vol. 46, no.3, 2009, pp. 371-402.,doi:10.1007/s00348-008-0593-2

[16] Hsiang LP, et al. *Drop deformation and breakup due to shock wave and steady disturbances.* Int J Multiphase Flow 21(4):545560

[17] Kannaiyan, K., et al. *Experimental investigation of spray characteristics of alternative aviation fuels.* Energy Conversion and Management 88 (2014) 10601069, 2014

[18] Lefebvre, A. H., and X. F. Wang. *Mean Drop Sizes from Pressure-Swirl Nozzles.* Journal of Propulsion and Power, 1 Feb. 1987

[19] Lefebvre, A. H. *Atomization and Sprays.* New York: Hemisphere Pub. Corp, 1989. Print.

[20] Markus Raffel, Christian E. Willert, Steven T. Wereley, Jrgen Kompenhans. *Particle Image Velocimetry: A Practical Guide 2nd Ed. 2007 Edition.* Springer, Berlin, 2007

[21] Mansour A. B., et al. *Hybrid atomizing fuel nozzle.* 15 Apr. 2003

[22] Meyer, S., et al. *Development of the Purdue University Integrated Gas Turbine Combustion Facility.* 41st AIAA/ASME/SAE/ASEE Joint Propulsion Conference and Exhibit, Arizona, July. 2005.

[23] Mugele, R. A., et al. *Droplet Size Distribution in Sprays.* Industrial and Engineering Chemistry, vol. 43, no. 6, June 1951, pp. 13171324

[24] Ortman, J. and Lefebvre, A. H. *Fuel Distributions from Pressure-Swirl Atomizers.* Journal of Propulsion and Power, 1 Feb. 1985

[25] Rizkalla, A. A., and A. H. Lefebvre *Influence of Liquid Properties on Airblast Atomizer Spray Characteristics.* Journal of Engineering for Power, American Society of Mechanical Engineers, 1 Apr. 1975

[26] Rachedi, R. R., et al. *A Study of Supercritical Jet Fuel Injection.* Volume 6: Energy Systems: Analysis, Thermodynamics and Sustainability — IMECE2007 — Proceedings — ASME DC, American Society of Mechanical Engineers, 1 Jan. 2007

[27] Vouros, A. P. et al. *Spray Characteristics of Alternative Aviation Fuel Blends.* Aerospace, MDPI, 2017

[28] Wang, X. F., and A. H. Lefebvre. *Influence of Fuel Temperature on Atomization Performance of Pressure-Swirl Atomizers.* Journal of Propulsion and Power, 1988

APPENDICES

A. REPEATABILITY
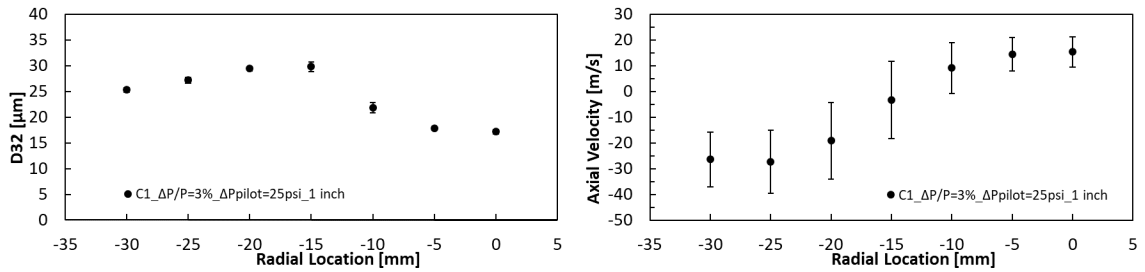
(a) Mean drop size for C-1 with uncertainty bars. (b) Axial velocity for C-1 with uncertainty bars.

Fig. A.1.: D_{32} **and Axial velocity for C-1 at** $\frac{\Delta P}{P} = 3$ %, $\Delta P_{Pilot} = 25$ **psi,** $T_{Fuel} = 120\ ^\circ F$, $T_{Airbox} = 250\ ^\circ F$
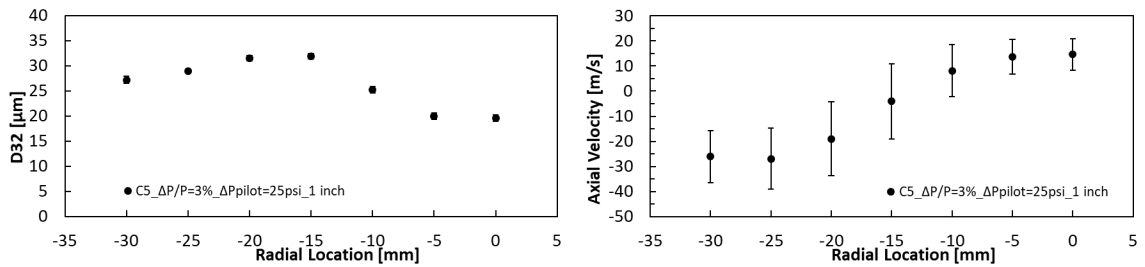
(a) Mean drop size for C-5 with uncertainty bars. (b) Axial velocity for C-5with uncertainty bars.

Fig. A.2.: D_{32} **and Axial velocity for C-5 at** $\frac{\Delta P}{P} = 3$ %, $\Delta P_{Pilot} = 25$ **psi,** $T_{Fuel} = 120\ ^\circ F$, $T_{Airbox} = 250\ ^\circ F$

B. PIPING AND INSTRUMENTATION DIAGRAM

Fig. B.1.: Piping and Instrumentation Diagram for Fuel Cart

Fig. B.2.: Piping and Instrumentation Diagram for VAPS rig in Rocket test cell

C. WEBER NUMBER AND OHNESORGE NUMBER

Table C.1.: Weber number and Ohnesorge number for A-2 with ΔP_{Pilot} variation and $\frac{\Delta P}{P}$ variation at %, $T_{Fuel} = 120\ ^\circ F$, $T_{Airbox} = 250\ ^\circ F$

ΔP_{Pilot}	$\frac{\Delta P}{P}$	r [mm]	-30	-25	-20	-15	-10	-5	0
	2 %	We	0.073	0.104	0.155	0.146	0.050	0.019	0.017
		Oh	0.109	0.108	0.113	0.119	0.126	0.123	0.126
25 psi	3 %	We	0.088	0.119	0.160	0.146	0.049	0.019	0.020
		Oh	0.123	0.128	0.131	0.130	0.139	0.132	0.127
	4 %	We	0.097	0.142	0.200	0.168	0.058	0.028	0.022
		Oh	0.121	0.123	0.131	0.144	0.136	0.135	0.132
50 psi	3 %	We	0.090	0.131	0.179	0.155	0.056	0.027	0.021
		Oh	0.117	0.116	0.123	0.132	0.130	0.130	0.132
75 psi	3 %	We	0.090	0.129	0.183	0.142	0.060	0.025	0.023
		Oh	0.115	0.109	0.114	0.120	0.112	0.134	0.135

Table C.2.: Weber number and Ohnesorge number for C-1 with ΔP_{Pilot} variation and $\frac{\Delta P}{P}$ variation at %, $T_{Fuel} = 120\ ^{\circ}F$, $T_{Airbox} = 250\ ^{\circ}F$

ΔP_{Pilot}	$\frac{\Delta P}{P}$	r [mm]	-30	-25	-20	-15	-10	-5	0
	2 %	We	0.093	0.126	0.206	0.151	0.048	0.024	0.020
		Oh	0.090	0.114	0.099	0.114	0.113	0.114	0.114
25 psi	3 %	We	0.118	0.159	0.204	0.169	0.062	0.030	0.025
		Oh	0.099	0.121	0.116	0.121	0.122	0.121	0.121
	4 %	We	0.140	0.204	0.278	0.198	0.073	0.040	0.030
		Oh	0.100	0.131	0.109	0.131	0.122	0.131	0.131
50 psi	3 %	We	0.107	0.164	0.241	0.188	0.063	0.033	0.032
		Oh	0.094	0.110	0.098	0.110	0.125	0.110	0.110
75 psi	3 %	We	0.117	0.183	0.235	0.248	0.068	0.040	0.036
		Oh	0.088	0.108	0.094	0.108	0.109	0.108	0.108

Table C.3.: Weber number and Ohnesorge number for C-5 with ΔP_{Pilot} variation and $\frac{\Delta P}{P}$ variation at %, $T_{Fuel} = 120\ ^{\circ}F$, $T_{Airbox} = 250\ ^{\circ}F$

ΔP_{Pilot}	$\frac{\Delta P}{P}$	r [mm]	-30	-25	-20	-15	-10	-5	0
	2 %	We	0.080	0.119	0.177	0.308	0.108	0.040	0.025
		Oh	0.040	0.039	0.040	0.043	0.047	0.053	0.055
25 psi	3 %	We	0.113	0.172	0.202	0.237	0.126	0.050	0.037
		Oh	0.043	0.042	0.043	0.046	0.051	0.051	0.051
	4 %	We	0.127	0.181	0.244	0.271	0.172	0.084	0.045
		Oh	0.043	0.045	0.046	0.046	0.047	0.048	0.052
75 psi	3 %	We	0.102		0.201		0.127		0.0320
		Oh	0.0412		0.0413		0.0466		0.0521

Table C.4.: Weber number and Ohnesorge number for C-7 with ΔP_{Pilot} variation and $\frac{\Delta P}{P}$ variation at %, $T_{Fuel} = 120\ °F$, $T_{Airbox} = 250\ °F$

ΔP_{Pilot}	$\frac{\Delta P}{P}$	r [mm]	-30	-25	-20	-15	-10	-5	0
	2 %	We	0.073	0.105	0.158	0.183	0.078	0.026	0.016
		Oh	0.021	0.020	0.021	0.022	0.023	0.024	0.024
25 psi	3 %	We	0.089	0.135	0.205	0.218	0.081	0.030	0.021
		Oh	0.022	0.021	0.022	0.023	0.024	0.024	0.024
	4 %	We	0.111	0.151	0.241	0.243	0.104	0.037	0.026
		Oh	0.022	0.022	0.022	0.023	0.024	0.024	0.024

Table C.5.: Weber number and Ohnesorge number for C-8 with ΔP_{Pilot} variation and $\frac{\Delta P}{P}$ variation at %, $T_{Fuel} = 120\ °F$, $T_{Airbox} = 250\ °F$

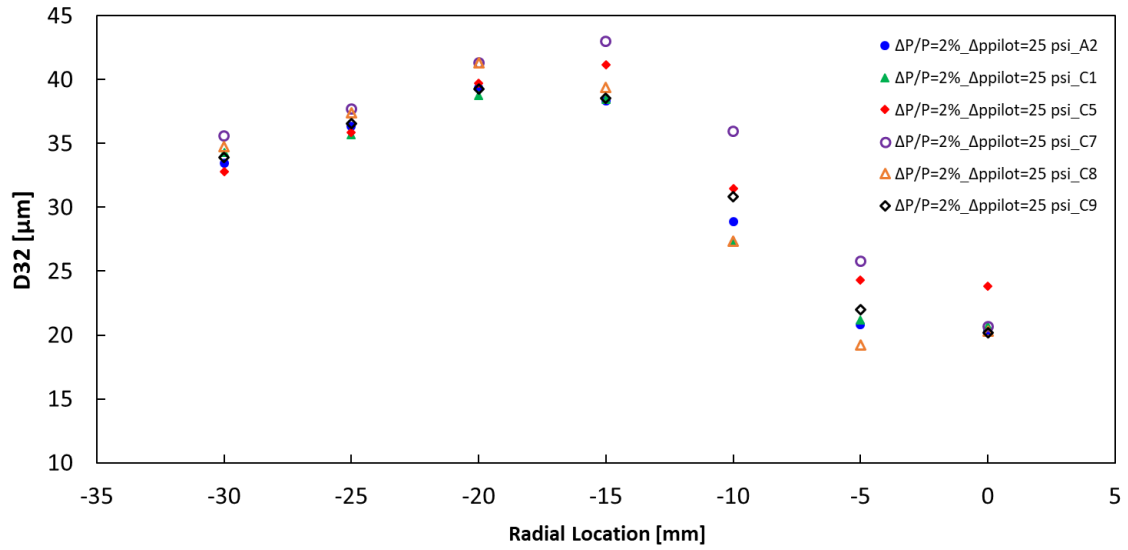| ΔP_{Pilot}	$\frac{\Delta P}{P}$	r [mm]	-30	-25	-20	-15	-10	-5	0
	2 %	We	0.079	0.113	0.178	0.150	0.041	0.018	0.017
		Oh	0.019	0.019	0.020	0.022	0.021	0.021	0.022
25 psi	3 %	We	0.110	0.146	0.214	0.176	0.052	0.023	0.021
		Oh	0.020	0.020	0.022	0.022	0.023	0.022	0.023
	4 %	We	0.119	0.177	0.268	0.214	0.061	0.031	0.027
		Oh	0.021	0.021	0.022	0.023	0.023	0.023	0.023

D. FUEL TYPES COMPARISON

Fig. D.1.: Comparison of Mean drop size for all six fuels at $\frac{\Delta P}{P} = 2$ %, $\Delta P_{Pilot} = 25$ psi, $T_{Fuel} = 120$ °F, $T_{Airbox} = 250$ °F
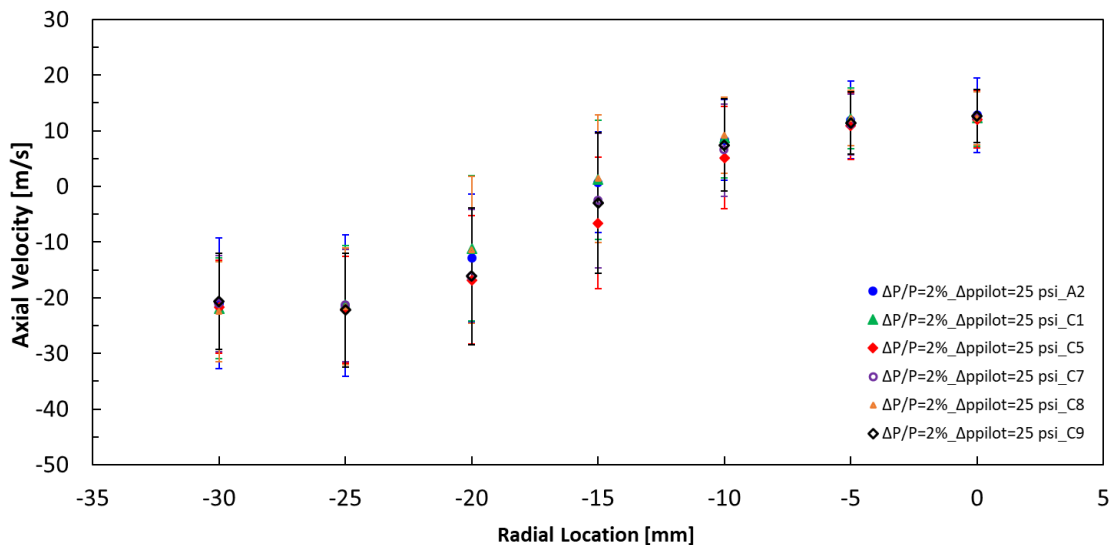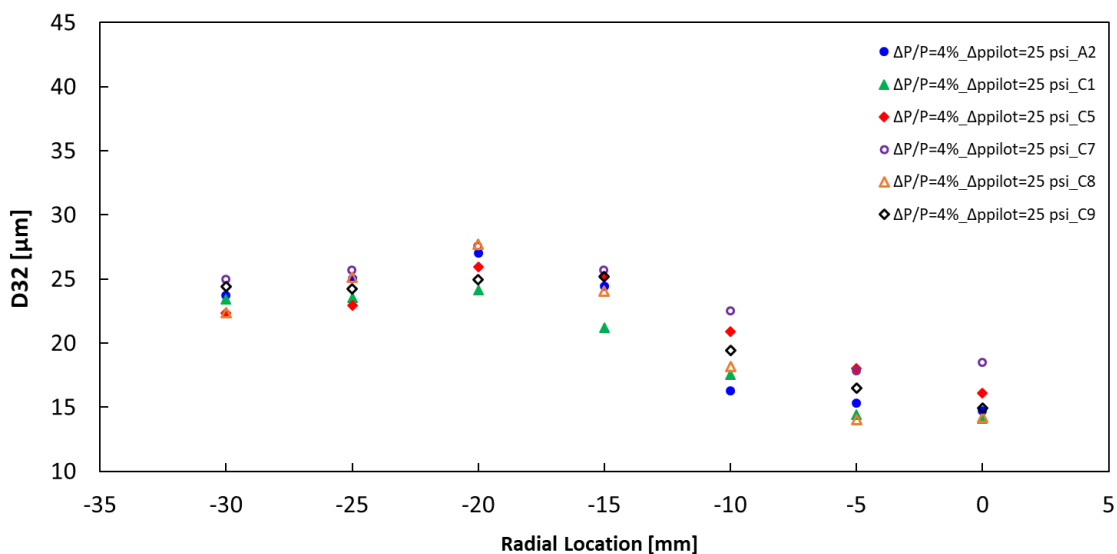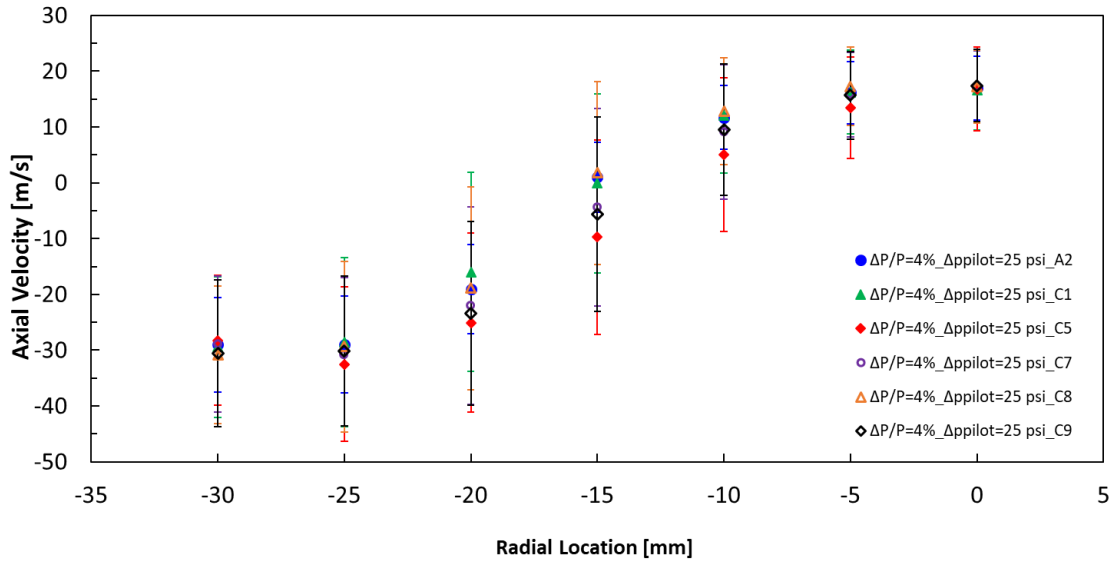
Fig. D.2.: Comparison of Axial Velocity for all six fuels at $\frac{\Delta P}{P} = 2$ %, $\Delta P_{Pilot} = 25$ psi, $T_{Fuel} = 120\ ^{\circ}F$, $T_{Airbox} = 250\ ^{\circ}F$

Fig. D.3.: Comparison of Mean drop size for all six fuels at $\frac{\Delta P}{P} = 4$ %, $\Delta P_{Pilot} = 25$ psi, $T_{Fuel} = 120\ ^{\circ}F$, $T_{Airbox} = 250\ ^{\circ}F$

Fig. D.4.: Comparison of Axial Velocity for all six fuels at $\frac{\Delta P}{P} = 4$ %, $\Delta P_{Pilot} = 25$ psi, $T_{Fuel} = 120$ $^{\circ}F$, $T_{Airbox} = 250$ $^{\circ}F$